INTEGRATED COMPUTATIONAL MATERIALS SCIENCE AND ENGINEERING FOR THE RESEARCH AND DEVELOPMENT OF GEN-IV METALLIC FUELS: APPLICATION TO URANIUM-NIOBIUM

A Dissertation

by

THIEN CHI DUONG

Submitted to the Office of Graduate and Professional Studies of
Texas A&M University
in partial fulfillment of the requirements for the degree of

DOCTOR OF PHILOSOPHY

Chair of Committee,	Raymundo Arróyave
Committee Members,	Tahir Çagin
	Miladin Radovic
	Sean McDeavitt
	Robert E. Hackenberg
	Patrice E.A. Turchi
Head of Department,	Andreas A. Polycarpou

December 2015

Major Subject: Mechanical Engineering

ABSTRACT

The concept of Integrated Computational Materials Science and Engineering (ICMSE) has emerged due to the need to accelerate the process of materials research and development at a fraction of the cost. In this work, we propose to apply ICMSE to the research and development of Gen-IV metallic fuels. As an illustration, the roles of thermodynamics and kinetics on the origin of uranium-niobium's discontinuous precipitation (DP) was investigated. For this, the used integrated computational framework included first-principles calculations, CALPHAD, and phase-field modeling.

Particularly, first-principles calculations were coupled with CALPHAD to consistently assess the thermodynamic properties of uranium-niobium. The assessment results were in good agreement with experiments. The consistent thermodynamic description was then used to estimate atomic mobility and diffusivity of bcc uranium-niobium. In turn, phase-field simulations were carried out to investigate the roles of thermodynamics and kinetics on the occurrence of DP via three possible hypotheses: the two local equilibria between α and γ, the kinetics of reaction front, and the ordering tendency of γ:

The two-local-equilibrium hypothesis was inferred from X-ray experiments. In its original form, the hypothesis assumed that α forms two common tangents with γ between which the first common tangent explains for the occurrence of DP while the second common tangent is responsible for discontinuous coarsening (DC), which is another interesting discontinuous reaction that follows after DP in the uranium-niobium system. In the current work, this hypothesis was re-examined using ICMSE's quantitative advantage. Study showed that this hypothesis is a possible explanation for

DP when further taking into account the thermodynamic effect of strain due to lattice/volume misfit as well as fast grain-boundary diffusion at the reaction front.

The kinetic hypothesis was proposed during our phase-field investigations of the kinetic effects on the occurrence of DP under the two-local-equilibrium hypothesis. It was found that when the kinetics of the reaction front is fast enough it can actively sustain the characteristic metastable phase of DP and ultimately leads to the stable growth of the reaction's lamellar microstructure. This however requires that the strain energy is needed in order to shift the first inflection point of γ's miscibility gap to a higher composition than that of the metastable phase so that γ_{1-2} falls within the metastable region of the gap.

The ordering hypothesis stems from the previous interesting finding which showed a pronounced tendency to short-range ordering in the equiatomic uranium-niobium alloy. This tendency, in principle, could lower the free energy of the system and allow an intermediate state during the decomposition of the γ phase which tends to legitimate the occurrence of the discontinuous reaction. Even though we can not directly verify the existence of such tendency in this work, we find through our first-principles calculations that this tendency is not likely to happen, at least for the investigated equiatomic bcc B2 and B32 uranium-niobium alloys.

The knowledge achieved in the current work contributes to a better understanding of the fundamental thermodynamics and kinetics that govern uranium-niobium and its discontinuous precipitation. Such fundamental understanding together with the integrated computational framework can serve as an infrastructure for future research and development of the fuel or for prognosis of its failure during nuclear operation, via which demonstrates the advantages of ICMSE in the research and development of nuclear fuels and Gen-IV Integrated Fast Reactor (IFR).

To mom, dad, big brother, and my love

ACKNOWLEDGEMENTS

First of all, I would like to express my gratefulness towards my advisor, Prof. Dr. Raymundo Arróyave. I owe him so much. He adopted me into the interesting field of materials science and engineering when I felt lost in my previous major after graduation. He taught me the fun and facts of computational materials science with his openness. He respected my freedom in research and gave me the opportunity to travel the world for learning. Thanks to him, I have learn so much and have come across so many interesting people and events in life. Thanks to him, I could make it this far.

I'm also thankful for having Anjana Talapatra, Anchalee Junkaew, Sean Gibbons, Shengyen Li, Navdeep Singh, Minsoo Park, and Saurabh Bajaj as my fellow colleagues. In Vietnam, elders teach that "*better learn from your friends than from your elders*." Such teaching I have never underestimated. My colleagues are special ones with whom I could discuss and from whom I have learned the meaning of science. With them have I also enjoyed a richer life throughout these years at Texas A&M University. As life brought us together for great moments, it has parted us for good and I believe that it will bring us together again for the better.

I would like to specially thank Robert E. Hackenberg (Bob) and his team at LANL for their valuable experimental data and insightful discussions. To me, Bob has been more than a collaborator but a demanding-yet-caring mentor. Tell you what, Bob? I have a feeling that you would be greater as a professor. I would also like to extend my heartfelt appreciation towards senior stalwarts Patrice E.A. Turchi and Alex Landa at LLNL. It is my true honor to be a part of their legacy. Patrice and Alex, my old men, I know you two do not like the task, which people in

my country humorously call knock-on-kid's-head task, for some reason I do have a strong impression that you are my teachers, especially you Patrice who firstly taught me about CALPHAD from an interesting view.

Lastly, my special appreciation towards Prof. Levente Vitos and Prof. Andrei Ruban for hosting and instructing me on the EMTO method during the time I was at KTH, Stockholm, and Prof. Ingo Steinbach and his team at ICAMS, Bochum for precious discussions and advices regarding phase-field methodology. This work could not be fulfilled without the financial support from NSF and LLNL through grants CMMI-0758298, 1027689, 0953984, 0900187 and DMR-0805293, the collaboration with LANL through Bob and his team. First-principles calculations were carried out in the Chemical Engineering Cluster and the Texas A& M Supercomputing Facility at Texas A&M University as well as in the Ranger Cluster at the Texas Advanced Computing Center at University of Texas, Austin.

NOMENCLATURE

ICMSE	Integrated Computational Materials Science and Engineering
DFT	Density-Functional Theory
CALPHAD	Calculation of Phase Diagram
PFM	Phase-Field Modeling
DP	Discontinuous Precipitation
DC	Discontinuous Coarsening
T	Temperature (K)
X	Composition ($at.\%$)
LLNL	Lawrence Livermore National Laboratory
LANL	Los Alamos National Laboratory
NSF	National Science Foundation
KTH	Kungliga Tekniska H¨ogskolan (The Royal Institute of Technology)
ICAMS	Interdisciplinary Centre for Advanced Materials Simulation

TABLE OF CONTENTS

Page

LIST OF FIGURES

FIGURE Page

FIGURE Page

FIGURE Page

FIGURE Page

LIST OF TABLES

TABLE Page

1. INTRODUCTION

1.1 Energy resources and human welfare

Ever since fire was first discovered, it has lit up the indispensable role of energy resources for human welfare. This role started as the modest means of firewood and straw for human survival during the early days such as heating up during winter and keeping wild animals away. Over eons, it gradually evolved to greater sophistication as humans realized that energy could exist under various forms and efficient sources could be harvested for better profits. Animals were then used for labor work, e.g. a horse to carry more goods, and wind power was later harnessed for higher productivity, e.g. a gristmill to produce more flour. Simply put, energy resources brought back prosperity when they were properly exploited. As humans reached a better understanding of this fact, they eventually found themselves on the same path seeking for the same mythical sources of welfare. Slowly but surely, new energy resources have been discovered along the timeline of human civilization.

These new energy resources first included the important fossil fuels: oil and charcoal. In their early days, oil was considered a nuisance as it contaminated drinking water, and charcoal merely made its humble presence felt in blacksmithing. It wasn't until the industrial revolution in the 17^{th} and 18^{th} centuries that fossil fuels significantly ramped up human living standards. These years saw the contiguous inventions of remarkable technologies such as steam engines, combustion engines, and electricity that established fossil fuels in their preeminent position of fulfilling human needs. Overnight prosperity was reflected in large-scale industrialization, expanding urbanization, higher food supplies, better healthcare, and universal education. To this end, fossil fuels significantly powered up human welfare, advanced erstwhile basic

needs to the modern plethora. The sudden affluence that relied so much on only a few energy sources, however, did not come without upsetting the balance.

Firstly, the exploitation of the fossil fuels led many countries to face a major political issue regarding their national energy security. As more and more of their infrastructure was based on fossil-fuel-based technologies, many nations became more and more reliant on these resources and hence vulnerable to their interrupted supply. At the same time, the natural reservoir of fossil fuels is limited, unequally distributed among the nations, and has been diminishing fast over the years, all of which affects the stable and secure deliveries of these energy resources. Consequently, the nations found it more and more difficult to maintain their economy leading to increased global competition. This more or less affected the general growth of human welfare.

Secondly, the combustion of fossil fuels has been releasing an enormous amount of greenhouse gases[1], e.g. carbon dioxide (CO_2), and other pollutants that have been aggravating the most serious global environmental changes, considerably impacting human welfare. In their fifth Synthesis Report in 2014, the United Nation Intergovernmental Panel on Climate Change (IPCC) highlighted that: "*recent climate changes have had widespread impacts on human and natural systems*," and "*continued emission of greenhouse gases will cause further warming and long-lasting changes in all components of the climate system, increasing the likelihood of severe, pervasive and irreversible impacts for people and ecosystems*." In addition, the World Health Organisation (WHO) published their study in 2011 showing that about 1.34 million people die prematurely each year due to PM10 pollutants, those less than 10 microns in air, which mostly originated in coal-fired power stations and motor vehicles. Other gases generated by the burning of fossil fuels have also been of concern due to

[1]According to the United Nation Intergovernmental Panel on Climate Change (IPCC), 57% of the global human-induced greenhouse gas emissions come from the burning of fossil fuels.

the threat they pose to human reserved cultures (due to acid rains) and the world's ecosystems (due to ozone depletion). At the end of the day, humans anticipate more the fact that their welfare is an inherent part of the Earth's.

For future stable development, it is crucial to reduce the negative impact of fossil fuels on human national economics and global environmental changes. This has been enabled by the reallocation of national resource consumptions into portfolios which compulsorily favor the by-degrees incoming shares from those of more sustainable and renewable green energies, discovered and/or elevated by new technologies from the 18^{th} century onwards. Those new resources, till date, include the hydroelectric, wind, solar, geothermal, biomass, and nuclear energies. Last of these is the 'peaceful-atom' resource which is most dependable in terms of sturdy supply, persistent operation, and high output, and hence shows great potential to guarantee the energy security of many nations as well as combat the global environmental changes.

1.2 Nuclear energy, integrated fast reactor, and metallic fuels

In their Energy Technology Perspective (ETP) published in 2010, the International Energy Agency (IEA) concluded that nuclear resource has played and will continue to play an important part in the portfolios of electricity generation and CO_2 reduction in the most cost-effective manner. Despite the Fukushima nuclear accident in 2011, the IEA has continued to emphasize the essential role of nuclear energy for stable future development in their ETP-2012 and ETP-2014 [8, 9], albeit in a more careful manner. Sharing the same perspectives, the U.S. Energy Information Administration (EIA) has also pointed out the importance of the nuclear component in their national energy portfolio. According to EIA, nuclear energy has contributed a considerable amount (723 million megawatt-hours) to the net national electricity produced in 2014 [10]. This accounts for approximately 19% of the U.S.

electricity portfolio relative to the 67% contribution from the fossil fuels (ratio of $1 : 3.5$). The relative contributions are based on electricity outputs of 100 nuclear power plants as opposed to $3,400$ coal, petroleum, and natural gas-fired power stations (ratio of $1 : 34$). In this scenario, the numbers effectively speak for themselves. Each megawatt-hour generated by the nuclear resource saves approximately 1.0 metric ton of CO_2 if the same amount of energy was produced by coal or 0.6 metric ton of CO_2 if it had been produced by natural gas, according to the U.S. Nuclear Energy Research and Development Roadmap in 2010 [11]. This "*offers the prospect of avoiding what could otherwise be an annual personal carbon footprint from electricity production of up to* 14 *metric tons of* CO_2," since "*the per capita electricity consumption in the United States is approximately* 14 *million megawatt-hours of electricity per year per person*" [11].

The nuclear resource has indeed shown its great potential for stable human welfare, but rather within a "*fire is a test of gold*"[2] context: After several nuclear incidents followed by the Three Mile Island accident (1979), public acceptance of the nuclear power generation dropped fast; major concerns rose up regarding the safety and reliability of nuclear operations. At the same time, governments started to worry about the potential threats arising from nuclear disposal, i.e. radioactive waste and proliferation risks. These have strongly affected the deployment of nuclear energy for constructive purposes. Given that "*nuclear energy is the only readily available large-scale alternative to fossil fuels for the production of continuous, reliable supply of electricity*" [12], overcoming social and political resistance is highly relevant to the stable development of a civil human society. This essentially requires the invention of advanced nuclear materials and technologies that take into account the key chal-

[2]Original as "*Ignis aurum probat, miseria fortes uiros*" in Seneca's Moral Essays, De Providentia (On Providence): cap. 5, line 9.

lenges: waste management, proliferation risk, safety and reliability. For this, critical actions have already been undertaken. Typically, the Generation IV International Forum (GIF), launched in 2001 and including 12 leading countries in nuclear energy, aimed to face the key challenges on a technical basis focusing on designing advanced nuclear reactors with enhanced safety, sustainability, proliferation resistance and improved economics [13]. Outcomes of GIF were six Gen IV reactor prototypes among which many favored the Integral Fast Reactor (IFR) concept over the conventional thermal reactors. This was due to the fact that IFR allows Pu-239 and other left-over minor actinides to be burnt more efficiently, i.e. close the fuel cycle, and therefore fundamentally solves the waste management and proliferation risk challenges. For solving the safety and reliability problem, IFR features the usage of metallic fuels.

Metallic fuels are alloys of nuclear fuels, mainly uranium and/or plutonium, with transition metals, such as zirconium, molybdenum, and/or niobium. The chemical interactions between the actinides and transition metals result in many interesting physical properties that inherently benefit IFR. This first includes the important inherent safety and reliability factors which the fuels introduce to IFR under normal-operation condition as well as operations under severe conditions. In particular, the excellent conductivities and compatibility of metallic fuels with IFR's coolant[3] make IFR's irradiation operations inherently safe with ambient residual-temperature condition since most of the generated heat is efficiently conducted out for beneficial work. This is especially remarkable when compared to commercial oxide fuels whose residual temperatures are usually high due to high-temperature operations and low conductivities ($\sim 2\ W/mK$ for oxide vs $\sim 20\ W/mK$ for metal). The metallic fuels are additionally attributed to have good thermal expansion coefficients which are also

[3]To maintain external fast neutrons at high energy, IFR makes use of liquid metal coolant instead of water moderator found in thermal reactors. Typical liquid metal coolants are sodium and lead.

compatible to those of claddings, again in contrast to those of oxide fuels. This at first sounds trivial but very importantly characterizes an inherent safety mechanism that allows IFR to auto-shutdown its power station under generic transient-without-scram severities such as loss-of-flow without scram (LOFWS), loss-of-heat-sink without scram (LOHSWS), or transient-overpower without scram (TOPWS). It is under such severities that metallic fuels clearly manifest their advantages over the oxides and other advanced nuclear fuels. To further demonstrate this inherent safety mechanism of metallic fuels, two landmark tests conducted in the Experiment Breeder Reactor II (EBR-II) on April 3, 1986 are listed [14, 15]:

- First, the LOFWS test was simulated under an extreme scenario in which EBR-II station was blacked-out and all safety systems had failed. Under this condition, the primary pump stopped circulating the reactor outlet coolant while the reactor was still at its full power. This rapidly raised the temperature of the outlet coolant (about 200^0C in 30 seconds), in turn heated up the fuel assembly hardware and caused it to expand. Interestingly enough, the expansion of the fuel assembly hardware enhanced neutron leakages, and hence slowed down the chain reaction and eventually shut down the reactor.

- Following the LOFWS test, the LOHSWS test was conducted on the same day. The primary pump was functioning normally to remove outlet heat from the core to the primary tank in this test. The intermediate pump was however shut down to disable the normal heat sink in the rest of the power plant. This eventually raised the temperature of the core inlet and caused it to expand when outlet heat could no longer be dumped out to the primary tank. This led to the same effect as in the LOFWS test: thermal expansion enhanced neutron leakage and hence reduced the reactor's power and eventually shut the reactor

down.

Other selective inherent safety and reliability characteristics can be further introduced to IFR with different solid solutions of metallic fuels. For instance, solid solution of zirconium in uranium is known to lower thermal neutron cross-section and suppress inter-diffusion between fuel and cladding. With addition of niobium, the brittle δ phase known to harm zirconium-uranium is concealed. The solid solution of molybdenum in uranium yields favorable microstructure allowing the metallic fuel to have a lower enrichment. Molybdenum-uranium also exhibits a higher melting temperature and thermal conductivity than that of zirconium-uranium. In addition, molybdenum is a stronger γ(bcc)-stabilizer that provides stable swelling behavior, and has a lower reaction potential with the ferrous cladding compared to zirconium. Apparently, metallic fuels introduce important inherent passive factors which allow the fast reactor to safely operate as well as shut down during some severe accidental situations.

Moreover, metallic fuels also facilitate the reprocessing of IFR for the so-called closed fuel cycle, that solves the waste management and proliferation risk as mentioned earlier. In IFR, the I(*ntegral*) mainly indicates the nuclear reprocessing which is integrated into the fast reactor to recycle spent fuels into new fuels. It is an important component of IFR in the sense that it not only enhances the efficiency of resource usage, leading to greater economy, but more importantly, through the recycling of left-over weapon-grade Pu-239 and other long-lived radioactive actinides for further fission, it addresses the political and social concerns regarding the proliferation risk and management of high-level waste. The current advanced technology for nuclear reprocessing is a pyrochemical processing based on electrorefining technique. In this technique, used fuel is attached to the anode of the electrorefiner and suspended in

the refiner's chemical bath. Electric current in turn dissolves the fuel and plates out uranium, plutonium, and other actinides on the electrorefiner's cathode. These extracted heavy elements are then cast into new fuel rods for a new fuel cycle. How do metallic fuels fit into this entire re-processing? First, due to their compatible natures, metallic fuels can be directly used in electrorefining without requiring any additional subprocesses such as the oxide reduction in the case of oxide fuels [16]. Firstly, this considerably simplifies the chemical process of nuclear re-processing, the re-processing's infrastructure, and the infrastructure's engineering design. Secondly, after the electrorefining, metallic fuels can be fabricated into new fuels relatively easily when compared to oxide fuels. Indeed, metallic fuels are very much compatible with most, if not all, of the conventional fabrication techniques including the injection casting that was actually used in the ERB-II. The easy fabrication of metallic fuels simplifies further the nuclear re-processing that allows for the closed fuel cycle, essentially easing the waste management and non-proliferation efforts.

Moreover, together with IFR, metallic fuels feature a burn-up rate as high as 20% and a higher breeding rate than that of oxide fuel ($1.3-1.5$ for metallic fuel vs 1.1 for oxide fuel). These advantages result in an increase in power output by $\sim 30\%$ relative to those of the oxide fuels. This brings about a higher economic value for the nuclear resource and at the same time strengthens national energy security. In addition, the higher efficiency also underscores the essential role of nuclear resources in combating global environmental changes. Indeed, given the 2014 electricity contribution from nuclear energy as reference [10], the increasing power output could replace 217 million megawatt-hours that would otherwise be produced by fossil fuels, hence saving an additional 217 million metric tons of CO_2 from being released to the environment each year. Undoubtedly, metallic fuels together with IFR elevate the role of the nuclear resource by not only addressing the listed social and political concerns but

also by better securing national energy supply and combating global environmental changes.

Perfecting IFR designs with focus on metallic fuels therefore promises great returns. Yet, it brings along many practical challenges. Among those challenges, the time and expense required for the research and development of metallic fuels are of concern. Conventionally, research and development of nuclear materials was carried out by mean of experimental trial and error. This discovery-based highly-empirical approach is generally time-consuming and cost-prohibitive, especially when design optimization of material properties are required to satisfy practical demands. Taking the uranium-zirconium and uranium-plutonium-zirconium alloys as examples, over 30 years of efforts (1964-1994) with tens of thousands of costly experimental fuel rods tested in EBR-II at Argonne National Laboratory to better understand the fuels' advantages and disadvantages has not yet resulted in a technology transfer of the fuels from test phase to massive applications. Recently, a new engineering discipline has emerged which has great potential to reduce the time needed for research and development of metallic fuels with a fraction of the cost, that of integrated computational materials science and engineering (ICMSE).

1.3 Integrated computational materials science and engineering

The concept of ICMSE is put forth upon the theoretical basis which integrates fundamental models and empirical relationships describing material information at different time and length scales across the processing-structure-property-performance paradigm into a holistic system. Such a system, with the aid of advanced computational science and technology, can be used to rapidly and efficiently assess the properties of materials on a routine basis and hence compensate for the experimental trial and error in reducing cost and time needed for the research and development

of materials. In its well developed and integrated form, ICMSE, from bottom up, offers a great mean to assess materials' multitude of sophistication for a better scientific insight (i.e. those of separate and often competing mechanisms that operate over a wide range of time and length scales to control the properties of materials). From top down, it represents a perfect liaison between materials science and engineering, that of an art to elevate simple raw materials into sophisticated refined forms that practically benefit human welfare.

Even in its current premature condition, ICMSE has already been demonstrating its remarkable advantages. To illustrate this, the virtual aluminum castings (VAC) methodology developed by Ford Motor Co. offers one great example [17]. VAC was initiated in an effort to reduce the cost and time needed to develop critical cast aluminum components such as cylinder head and engine block. It integrated computational tools that capture material information across the processing-structure-property-performance hierarchy to allow complete simulations of the entire casting processes of the components from initial mold preparation to final durability analysis [17]. Before VAC, the developments of the cast aluminum components were conducted via the conventional iterative testing-rework-retesting process. For this, traditional computer-aided engineering (CAE) approach for durability prediction provided a starting point. Due to the lack of information on the influence of manufacturing process on the components' properties, such a CAE prediction however could only be approximate. Consequently, the designed components were not optimal and often failed during new engine development, leading to costly redesign, retooling, and project delays. The implementation of VAC via ICMSE offered the advantage of assessing the manufacturing analysis prior to the durability prediction and hence provided the essential information for a more realistic durability prediction. In addition, it allowed Ford engineers to adjust both manufacturing and product design

variables in order to concurrently optimize both material properties and component configurations, leading to high-quality satisfactory products for end users. At the end, VAC was reported to benefit Ford Motor Co. with a 15 – 25 percent reduction in design time and component tests and a cumulative saving of about 120 million dollars, projecting to a remarkable combined return of investment (ROI) of well over 7:1 [18].

Another success of ICMSE is the integrated computational prognosis of stockpile pit lifetime conducted at Los Alamos National Laboratory (LANL) and Lawrence Livermore National Laboratory (LLNL). Stockpile pit is one of the most important components in the nuclear stockpile complex. Since it contains the radioactive plutonium element, it will eventually decay to failure and need to be refurbished. The question is, when will this happen? As the U.S. government was planning to construct a modern pit facility for the future refurbishment and manufacturing needs of this component, estimates of pit lifetimes was crucial for planning the size and schedule of this facility, and hence was of special interest. Consequently, the National Nuclear Security Administration (NNSA) had sponsored a program to provide predictions of primary-stage pit lifetimes owing to plutonium decay. This program had to face a technical and a political issue. First, the current technology available for predicting component lifetime is based on accelerated aging tests which are difficult and expensive, especially for the case of plutonium. Second, the performance tests of pits needed to verify the accelerated aging tests are prohibited by national policy as the result of U.S. voluntary compliance with international treaties. These two issues left integrated computational approach the only alternative. For this, scientists at LANL and LLNL had developed an ICMSE system combining the results of previous performance tests, theoretical investigations, and computer simulations of stockpile pits with varying ages and combinations of impurities. This integrated computa-

tional system, costing no more than an accelerated aging test, was able to provide accurate estimates of pit lifetimes and therefore allow any pit facility construction to be scheduled appropriately. This saved the U.S. government from the approximate expense of 1.5 billion dollars for constructing the new facility as the prediction indicated longer pit lifetimes than expected, projecting to an overall remarkable ROI of 10:1. More importantly, the success of ICMSE in this case manifested its unique capability in addressing special cases where the conventional experimental approach fails. Indeed, as pointed out by the US national material advisory board on ICME in 2008, the above results "*could not have been provided using conventional prototyping and component testing without violating national nuclear policies*" [18]. Truly, ICMSE can transform our ability to understand and design new materials.

Based on the above successful cases, the advantageous implementation of ICMSE for the developments of nuclear fuels and IFR could be foreseen as follows. On a small scale, an integrated virtual injection casting (VIC) system similar to VAC can be constructed to simulate the entire processing of metallic-fuel rods. This system, in particular, could include a computer-aided design (CAD) step to first prepare a virtual 3D mold. Commercial softwares such as ProCast and OptCast can then be used to simulate the casting and heat treatment processes (e.g. solution treatment and aging). During these thermal processes, computational thermodynamic tools such as Pandat, Thermo-Calc, and Dictra can be utilized to model a wide range of critical stable/metastable microstructures which would appear as the results of different heat treatment conditions. The effects of these microstructures on key mechanical and physical properties (e.g. fatigue, strength, and thermal growth) of fuel rods could later be investigated using in-house packages developed specially for analyzing the rods. Finally, the assessed mechanical and physical properties and their spatial distributions can be mapped into component and subsystem finite-element

analysis (FEA) of operating reactors to predict the rods' performance. On a larger scale, the structure-property-performance parts of VIC could be further integrated with the ICMSE, CAE, and FEA of other IFR components. Idealistically, this would allow the simulation of a whole fast reactor during its operation and the beauty of this is the *in situ* prognosis of future reactor failures. Proper plan for maintenance or permanent shutdown of the physical reactor could then be scheduled and tragedies such as the Three Mile Island and Fukushima could likely be avoided. To this end, effort in encouraging and accelerating the implementations of ICMSE for the research and development of nuclear fuels and IFR is highly needed.

1.4 Application to uranium-niobium

In order to support such an effort, we propose in the current work the application of ICMSE to the research and development of uranium-niobium. Over the years, uranium-niobium has been known to be a promising nuclear fuel for Gen-IV fast breeder reactors. The material exhibits a high melting point, good corrosion resistance, good conductivity and continuous bcc region at high temperatures. This, in principle would introduce stability during the thermal operation of the reactor given that the desired fuel exists in the form of pure-bcc single- or poly-crystallite. In reality, depending on its heat treatment conditions, various forms of metastable phases exist as different microstructures within the bcc matrix, among which, some lead to the fuel's enhancements while other to its degradation. In this section, we introduce two special phenomena, of which attributing lamellar structures are known to degrade the fuel's corrosion resistance and ductility: discontinuous precipitation (DP) and discontinuous coarsening (DC). Together, DP and DC comprise uranium-niobium's discontinuous[4] monotectoid decomposition ($\gamma_1 \xrightarrow{DP} \alpha + \gamma_{1-2} \xrightarrow{DC} \alpha + \gamma_2$,

[4]Note here that the word "discontinuous" in discontinuous monotectoid decomposition/reaction indicates the discontinuity of the decomposition/reaction process, as contrasted with continuous

see Fig. 1.1) whose origin fascinates us.

During the monotectoid decomposition of uranium-niobium, a quenched γ_1 (U-rich bcc) does not decompose continuously into the end equilibria of α (orth) and γ_2 (U-depleted bcc). Instead, it tends to transform into different intermediate states depending on its heat treatment condition. Aging at $\sim 300^0C$ and lower results in significant age-hardening accompanied by subtle microstructural changes (e.g., [20, 21, 22, 23]). Under these conditions, the system remains distant from thermodynamic equilibrium after even long-term ($\sim$ 5 years) aging and the specific transformation mechanisms remain unresolved. Therefore, this low-temperature aging regime will not be further examined here. The microstructural evolution upon aging at higher temperatures ($300 - 647^0C$) has been more definitively characterized. In particular, the system accesses a mixture of α phase plus a metastable phase of an intermediate Nb composition with the same bcc crystal structure as the stable γ_2 phase, referred as γ_{1-2} in this work ($\gamma_1 \rightarrow \alpha + \gamma_{1-2}$). This mixture has a lamellar structure and is associated with the so-called cellular or DP reaction [19]. After further prolonged annealing, the metastable γ_{1-2} transforms into the final mixture of α and γ_2 when stable γ_2 nucleates inside the system ($\alpha + \gamma_{1-2} \rightarrow \alpha + \gamma_2$). During this process, the lamellar structure coarsens, hence the process is designated as DC. The prototypical alloy exhibiting this sequence of phase transformations is U-13 $at.\%$ Nb, which coincidentally is the same as that in the monotectoid invariant reaction [24, 25, 26, 21]. The same phase transformations have been observed in both leaner and richer alloys [27, 28, 29, 30, 1, 31].

decomposition processes such as spinodal decomposition and order-disorder reactions. It should be differentiated from the specific mechanisms of DP and DC which indicate the abrupt change in composition between the precipitate and matrix γ phases at their interface (see Fig. 1.1 or [19] for details).

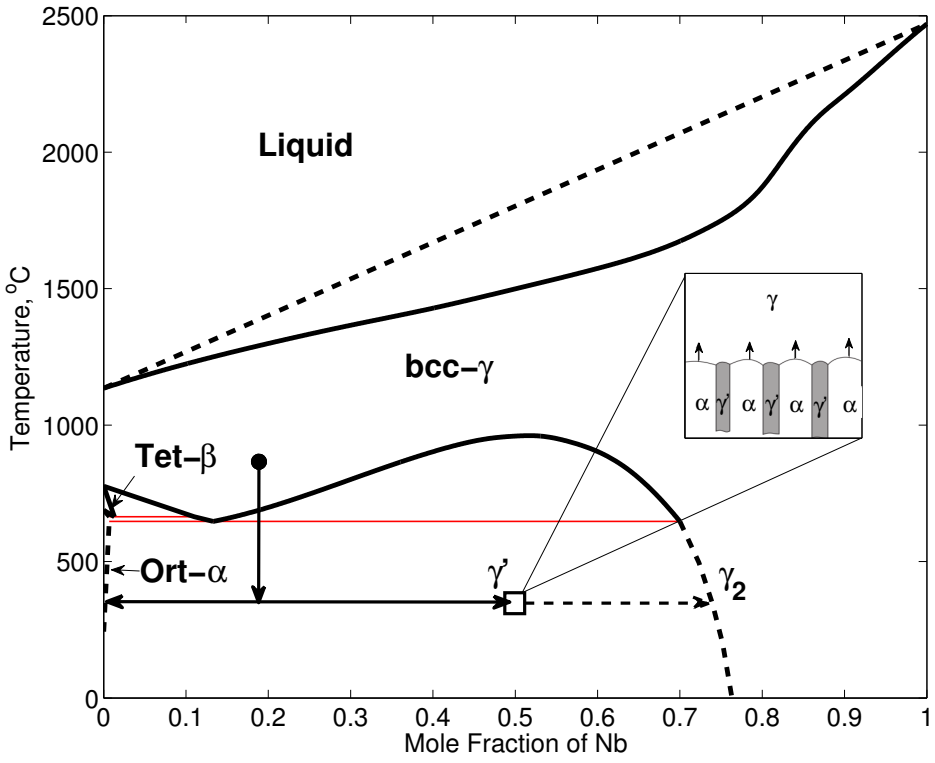

Figure 1.1: Schematic demonstration of discontinuous monotectoid decomposition in uranium-niobium system.

Djuric's hypothetical free energies - Reprinted from [1]

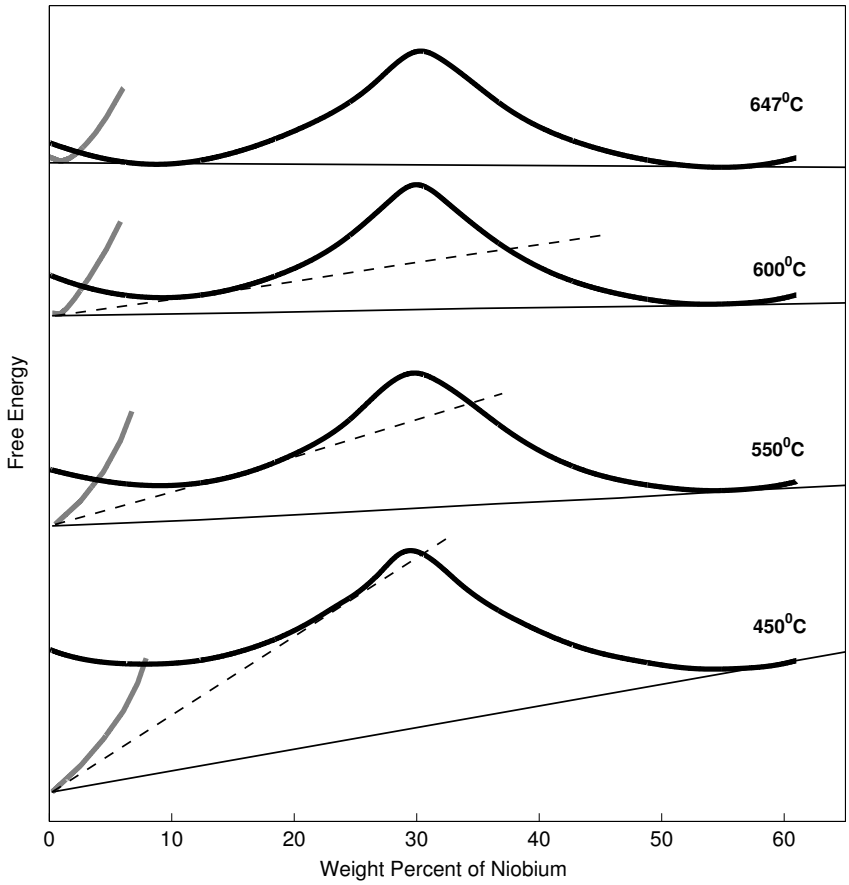

Figure 1.2: Hypothetical energy profiles proposed by Djuric *et al.* [1].

Although the observations of DP and DC in uranium-niobium system have been commonly reported by multiple research groups, the origin of their occurrences (or the separation of uranium-niobium's monotectoid decomposition into DP and DC subprocesses) has not been addressed in a satisfactory manner. To a certain extent, this is expected since the discontinuous reactions by themselves are among the most intricate solid state heterogeneous phase transformations [19], keeping aside

the additional sophistication from the actinide complex (i.e. f transition metals). Between these two reactions, the occurrence of DP in general is more complicated and is therefore often a topic of much interest and discussion. This is due to the fact that a successful occurrence of DP is essentially associated with the occurrence and sustainment of a metastable phase (e.g. γ_{1-2}) that coexists with a stable or near-stable phase (e.g. α) in form of lamellae. The existence of such a metastable phase always challenges the laws of equilibrium thermodynamics and hence posts interesting scientific questions. Relative to DP, DC, which usually follows after DP (or other cellular reactions), simply involves the compositional adjustment and redistribution of cellular aggregates, and hence appears to be readily assessable when the origin of DP is well understood. As such, the focus of the current work is on DP with minimal discussion occasionally extended to DC as this tends to support better the understanding of DP. Conventionally, DP is found to occur in systems that exhibit a certain lattice parameter and/or atomic size mismatch [32, 19]. These conditions are hence used to explain the occurrence of the reaction. Being practically convenient, such an explanation is however not applicable to all systems [32, 19]. Also, from scientific point of view, it is fairly empirical and does not essentially shed much light on the fundamental nature of the reaction and its associated systems. On this side, the current work aims to investigate the occurrences of DP and DC reaction in the uranium-niobium system from a more fundamental view of thermodynamics and kinetics. For this, we find that Djuric's hypothesis [1] on the discontinuous monotectoid reaction of the uranium-niobium system provides an interesting start point.

According to Djuric, α and γ should have their free-energy profiles formed with two LE, or common tangents: one at the intermediate composition, γ_{1-2}, and the other at the equilibrium composition, γ_2 (Fig. 1.1). Due to the former LE, γ would

decompose partially into α and metastable γ_{1-2}, if its initial composition γ_1 was less than γ_{1-2}. This explains the occurrence of DP. If by chance γ_2 nucleated inside the system, the stable phase would set up a lower energetic reference towards which the system would simultaneously evolve, i.e. the occurrence of DC. To demonstrate his explanation, Djuric hypothesized several energy profiles and LE common-tangent constructions, replicated in Fig. 1.2, without quantitatively describing them. In the present work, this hypothesis is examined in view of a hierarchical computational thermodynamic and kinetic methodology [33, 34, 35]. In particular, phase-field diffusion couples, designated as free-energy minimization processes, are carried out to investigate possible LE between α and γ during uranium-niobium's monotectoid decomposition of the initial γ_1. To account for the non-equilibrium transformation from the initial γ_1, the phase-field model with finite interface dissipation (in short, interface dissipation model), recently developed by Steinbach *et al.* [36, 37], is considered. The usage of this model necessitates CALPHAD assessments of both thermodynamic and kinetic databases of the uranium-niobium system.

Here, it is noted that the thermodynamic database of uranium-niobium system has already been assessed by Liu *et al.* [5], and its result was later used by Liu *et al.* [6] to estimate the kinetic diffusivities of γ. Although, the thermodynamic study [5], on which the kinetic work [6] is based, shows good phase equilibria under the liquidus line, consistent with previous evaluations and experiments [2, 38, 39, 40], extrapolation of γ-free energy to temperatures above 5000^0C results in an inverse miscibility gap, manifested in the metastable diagram of the bcc phase. As indicated by Bajaj *et al.* [41], even though this phenomenon is thermodynamically eligible as found in various polymers, it is likely an assessment artifact in simple metallic alloys. They have pointed out that CALPHAD's parameter optimization is an inverse problem that has many possible solutions among which some may contain unrea-

sonable "hidden" phase stabilities. According to Bajaj *et al.* , the use of *ab initio* energetic data can impose a restriction in CALPHAD optimization hence reducing the artifacts' probability. In the present work, we practice the self-consistent assessment strategy, coupling first-principles calculations with CALPHAD methodology, as suggested in [41]. In particular, first-principles calculations are carried out within the framework of Density Functional Theory (DFT) to estimate for the ground-state heats of formation of γ. The *ab initio* energies are then combined with experimental equilibria to re-assess the fundamental thermodynamics of uranium-niobium via CALPHAD. Assessment results are overall in reasonable agreement with the work of Liu *et al.* [5] without producing the inverse miscibility gap. Their reliability is further checked against our supplementary equilibria of the $\gamma_2/\alpha + \gamma_2$ phase boundary measured by sufficient long-term aging experiments (up to 5 years). The reliable thermodynamic data is then used to re-evaluate the kinetic diffusivities of γ described in terms of atomic mobilities [42] also within the framework of CALPHAD.

With the self-consistent thermodynamic and kinetic information available, phase-field diffusion-couple simulations are carried out to investigate possible LE between α and γ within the temperature range of interest. Interestingly, it is seen that the acquired CALPHAD free energies partially agree with Djuric's hypothesis at the investigated temperatures, i.e. on one hand they do show two common tangents at temperatures between 605^0C and 647^0C in consistent with Djuric's assumption while on the other hand they exhibit only one LE at the γ_2 composition in the temperature range from 400^0C to less than 605^0C. To explain for this partial agreement in favor of Djuric's hypothesis, we make use of the previous explanation for DP to argue that due to the volume and lattice mismatches between α and γ, there exists an additional strain energy to the CALPHAD free energies within the reaction-front region. While this energy is likely promoting a new thermodynamic state being

responsible for the peculiar discontinuity of the monotectoid decomposition, it may not be sufficiently captured by the CALPHAD extrapolation of the non-equilibrium part of the free energies at low temperatures. To account for the addition, we develop new free energies based on the original CALPHAD profiles and following Djuric's proposition. The resulting free energies are called strain-adjusted free energies, i.e. the combinations of bulk chemical and interfacial strain energies, which should only be valid when there exist lamellar interfaces between α and γ, therefore the strain field. The quantitative description of these proposed strain-adjusted free energies is given by a modified CALPHAD model. Phase-field diffusion-couple simulations are then carried out using the strain-adjusted free energies and the results show that the monotectoid decomposition rests at the intermediate state of α and γ_{1-2} and continues to decompose towards the final stable product of α and γ_2 when the stable γ_2 nucleates inside the system, in consistent with Djuric's hypothesis. This however is not sufficient enough to back up a solid conclusion that Djuric's hypothesis explains the occurrences of DP and DC. As previously mentioned, a successful occurrence of DP in general must be associated with the stable occurrence and sustainment of a metastable phase coexisting with a stable or near-stable phase in the form of a lamellar structure. While Djuric's hypothesis can best explain the coexistence of α and γ_{1-2}, it does not essentially guarantee a lamellar structure for these two phases. To further investigate this, 2-D phase-field simulations were carried out. It has been shown that when the fast grain boundary diffusion that is inherent to discontinuous reactions is considered, a reasonable growth of DP lamellar microstructures could be observed therefore leads us to conclude that Djuric's hypothesis is one possible explanation for the occurrence of the discontinuous reactions in the uranium-niobium system.

During the phase-field investigations, it is interestingly found that kinetics can

also act as a main mechanism to sustain the metastable γ_{1-2} and lead to the stable lamellar growth of DP. This mechanism tends to relax out the strict thermodynamic condition proposed by Djuric. However, minimal support from thermodynamics is still needed. Within the context of this work, such a support is the additional strain energy which tends to shift the inflection point to a value higher than that of the intermediate γ_{1-2} and hence allows this phase to lie out side of the thermodynamically unstable region of the γ's miscibility gap. Finally, another possibility to explain for the origin of the discontinuous reactions is discussed. This possibility stems from Strelova's finding which suggests a pronounced tendency to short-range ordering in the equiatomic uranium-niobium alloy [43]. This tendency could lower the free energy of the system and allow an intermediate state during the decomposition of the γ phase. Even though we can not verify the existence of such tendency, we find through our first-principles calculations that this tendency is not likely to happen, at least for the investigated bcc B2 and B32 equiatomic uranium-niobium alloys. Further theoretical and experimental investigations on the ordering tendency of equiatomic bcc uranium-niobium and its relationship to the discontinuous reaction are encouraged. The details of the integrated computational framework and its application to the investigation of the fundamental thermodynamics and kinetics of uranium-niobium and its discontinuous reactions are presented in the following sections.

2. INTEGRATED COMPUTATIONAL FRAMEWORK

2.1 Density functional theory

2.1.1 Overview

Density-functional theory (DFT) is one of the most popular and successful quantum mechanical approaches to matter. It is nowadays routinely applied to calculate many important properties of materials such as binding energy, band structure, phonon density, magnetic moment, elastic constants, etc., using only empirical-free input data, e.g. crystal structure and atomic position. For this, it has been recognized as an important methodological component of ICME. To have a general idea of what DFT is about, let us first recall some elementary knowledge from quantum mechanics.

In quantum mechanics, it is known well that all information about a given system which one could possibly have is contained in the system's wavefunction Ψ. In particular, an observable, O, of a system can be estimated from the system's wavefunction, Ψ, as follows:

$$O = \left\langle \Psi \left| \hat{O} \right| \Psi \right\rangle \tag{2.1}$$

where, $\hat{O}$ is a quantum operator corresponding to O; for instance, Hamiltonian, $\hat{H}$ and delta function, $\sum_{i=1}^{N} \delta(r - r_i)$, are the operators of the observable total energy and electron density, respectively:

$$E = \left\langle \Psi \left| \hat{H} \right| \Psi \right\rangle = N \int dr \cdots \int dr_N \Psi^*(\vec{r}, \vec{r}_2, \ldots, \vec{r}_N) \hat{H} \Psi(\vec{r}, \vec{r}_2, \ldots, \vec{r}_N) \tag{2.2}$$

$$n(\vec{r}) = \langle \Psi \, | \hat{r} | \, \Psi \rangle = N \int dr_2 \cdots \int dr_N \Psi^*(\vec{r}, \vec{r}_2, \ldots, \vec{r}_N) \Psi(\vec{r}, \vec{r}_2, \ldots, \vec{r}_N) \tag{2.3}$$

The wavefunction, Ψ, can be calculated from the many-electron time-independent Schrödingers equation which, within the Born - Oppenheimer approximation that treats the atomic nuclei as fixed particles, reduces to the following electronic wave equation:

$$\hat{H}\Psi = \left[\hat{T} + \hat{U} + \hat{V}_{ext}\right] \Psi = \left[\sum_i^N \left(-\frac{\hbar^2}{2m_i}\nabla_i^2\right) + \sum_{i<j}^N U(\vec{r}_i, \vec{r}_j) + \sum_i^N V_{ext}(\vec{r}_i)\right] \Psi = E\Psi \tag{2.4}$$

where, for the N-electron system, $\hat{H}$ is the Hamiltonian, E is the total energy, $\hat{T}$ denotes the kinetic energy, $\hat{U}$ denotes the electron-electron interaction energy, and $\hat{V}_{ext}$ denotes the potential energy from the external field due to positively charged nuclei. Note that (1) $\hat{T}$ and $\hat{U}$ are universal as they are the same for every N-particle system while $\hat{V}$ is system dependent, and (2) Eq. 2.4 cannot be separated into a system of simpler single-particle equations because of the interaction term $\hat{U}$.

To solve the many-electron time-independent Schrödingers equation for the wavefunction, there are many sophisticated methods; for example, in physics we have the diagrammatic perturbation theory based on Feynman diagrams and Green's functions, while in chemistry we often use the methods from the Hartree-Fock family which is based on the Slater determinants. However, these methods are attributed to the problematic huge computational effort which makes them practically impossible to be implemented efficiently for large and complex, therefore more realistic, systems (see for example [44] for a very nice "guesstimate").

It is here where DFT provides an appealing alternative or, according to its father, the Austrian American physicist Walter Kohn, "*a complementary perspective*" [44] which is more versatile than the previous models. In particular, DFT provides a way to systematically map the complicated many-body massive-interacting system onto a much simpler single-body non-interacting system. This is described in a series of famous papers establishing DFT by Kohn, his coworker, Pierre Hohenberg, and post-doctoral fellow, Lu Sham, in the years of 1964-1965 (the ones which brought Kohn the most prestigious Nobel prize later in 1999 to credit his significant contributions via DFT and which makes DFT so far the only ICME methodological component that has this great honor). In these papers, Kohn and co-workers seek to describe a system in term of its electron density, $n(\vec{r})$, instead of the electrons' atomic positions, $(\vec{r}_i,\, i = 1..N)$.

2.1.2 Electron density as the basis variable

Why electron density? To me and many others of the young generation of DFT practitioners, the most intuitive explanation is that it reduces $3 \times N$ atomic degrees of freedom (DOFs of N particles along 3 spatial directions, XYZ) to only 3 DOFs (n_x, n_y, and n_z), making whichever equation that it may result in more solvable than Eq. 2.4. This, however, was not Kohn's original interest but a crucial physical insight: "*Ever since my period at the Carnegie Institute of Technology (1950-1959) I had been interested in disordered metallic alloys, partly because of the excellent metallurgy department and partly because of the interesting experimental program of Emerson Pugh, in Physics, on substitutional Cu alloys with the adjacent elements in the periodic table, such as* Cu_xZn_{1-x}. *These alloys were viewed in two rather contradictory ways: As an average periodic crystal with nonintegral atomic number* $Z = xZ_1 + (1-x)Z_2$ *(*$Z_1 = 29$, $Z_2 = 30$*). This model nicely explained the linear*

dependence of the electronic specific heat on x. On the other hand the low temperature resistance is roughly proportional to $x(1-x)$, reflecting the degree of disorder among the two constituents. While isolated Cu and Zn atoms are, of course, neutral, in a Cu-Zn alloy there is transfer of charge between Cu and Zn unit cells on account of their chemical differences. The electrostatic interaction energy of these charges is an important part of the total energy. Thus in considering the energetics of this system there was a natural emphasis on the electron density distribution $n(r)$," said Kohn [44].

Now, it should be known that the idea of using electron distribution to describe matter was long proposed by Thomas and Fermi in their electronic-structure model. Even though the Thomas-Fermi model was not very successful for quantitative descriptions of electronic structures in matter, it suggested the interesting hypothesis that the ground-state density, $n_0(\vec{r})$, of any electronic system uniquely determines the electronic system, i.e. the wavefunction, Ψ, and hence everything! It was the correctness of this hypothesis that intrigued Kohn many years later.

2.1.3 The Hohenberg-Kohn theorems

In his sabbatical semester at Ecole Mormale Supérieure in 1964 Kohn joined forces with Hohenberg and derived the first foundation of DFT, the so-called *basic lemma of Hohenberg and Kohn* [45] in which Hohenberg and Kohn confirmed that the Thomas-Fermi hypothesis is correct. The proof of this lemma is straightforward as follows:

First, assuming that there were two external potential $V_{ext}(\vec{r})$ and $V'_{ext}(\vec{r})$ that differ by more than a constant and give the same $n(r)$ for their corresponding ground states, there would exist two different Hamiltonians $\hat{H}$ and $\hat{H}'$ with different normalized wave functions Ψ and Ψ' but identical ground-state densities. Now, taking

Ψ' as a trial wave function for $\hat{H}$ and applying the Rayleigh-Ritz minimal principle yields:

$$\begin{aligned} E_0 &< \langle \Psi' | \hat{H} | \Psi' \rangle \\ \Leftrightarrow E_0 &< \langle \Psi' | \hat{H}' | \Psi' \rangle + \langle \Psi' | \hat{H} - \hat{H}' | \Psi' \rangle \\ \Leftrightarrow E_0 &< E_0' + \int n(\vec{r})[V_{ext}(\vec{r}) - V_{ext}'(\vec{r})]d\vec{r} \end{aligned} \tag{2.5}$$

where E_0 and E_0' are the ground-state energies for $\hat{H}$ and $\hat{H}'$, respectively. Similarly, taking Ψ as a trial wave function for $\hat{H}'$ and applying the Rayleigh-Ritz minimal principle yields:

$$\begin{aligned} E_0' &< \langle \Psi' | \hat{H}' | \Psi' \rangle \\ \Leftrightarrow E_0' &< \langle \Psi' | \hat{H} | \Psi' \rangle + \langle \Psi' | \hat{H}' - \hat{H} | \Psi' \rangle \\ \Leftrightarrow E_0' &< E_0 + \int n(\vec{r})[V_{ext}'(\vec{r}) - V_{ext}(\vec{r})]d\vec{r} \end{aligned} \tag{2.6}$$

Now, adding Eq. 2.5 and Eq. 2.6 leads to the contradiction: $E_0 + E_0' < E_0' + E_0$. Therefore, by *reductivo ad absurdum*, we can conclude that there cannot be two different $V_{ext}(\vec{r})$ and $V_{ext}'(\vec{r})$ that give the same $n(\vec{r})$ for their ground state. In other words, $n(\vec{r})$ uniquely determines $V_{ext}(r)$; from above, we know as well that V_{ext} specifies H of the system (since T and U are universal); $n(\vec{r})$ must then specify Ψ and ultimately every observables of the system, i.e. $n_0(\vec{r}) \rightarrow V_{ext}(r) \rightarrow \Psi_0 \rightarrow$ *everything*!, and so confirm the Thomas-Fermi hypothesis.

Although the Hohenberg-Kohn basic lemma revealed the important truth, it was not self-containing. How could we find the exact ground-state electron density, i.e.

$n_0(\vec{r})$ an observable, without a pre-knowledge of the exact ground-state wavefunction, Ψ_0 (see Eq. 2.3)? What could possibly be the mappings from the electron density, $n_0(\vec{r})$, to the wavefunction, Ψ_0? The lemma did not provide any clues for these questions. In the second effort in 1964, Hohenberg and Kohn proposed an energy functional, i.e. the energy function of matter written in term of $n(\vec{r})$ instead of $\vec{r}$ (as in Eq. 2.4):

$$H = T(\vec{r}) + U(\vec{r}) + V_{ext}(\vec{r}) = T[n(\vec{r})] + U[n(\vec{r})] + V_{ext}[n(\vec{r})] \tag{2.7}$$

Hohenberg and Kohn then applied the variational principles on this energy functional, leading to the so-called *Hohenberg-Kohn density variational principles*:

$$T[n_a(\vec{r})] + U[n_a(\vec{r})] + \int v_{ext} n_a(\vec{r}) \geq T[n_0(\vec{r})] + U[n_0(\vec{r})] + \int v_{ext} n_0(\vec{r}) = E_0 \tag{2.8}$$

where, $V_{ext}[n(\vec{r})] = \int v_{ext} n(\vec{r})$, $n_a(\vec{r})$ is some arbitrary electron density, $n_0(\vec{r})$ is the exact ground-state electron density corresponding to V_{ext}, and E_0 is the exact ground-state energy. The significance of the Hohenberg-Kohn density variational principles was that it provided a guideline to estimate the ground-state electron density of matter: *only the true ground-state electron density of a system can minimize the energy functionals, $H[n(\vec{r})]$, of that system.* This was a very general guideline and did not actually answer the above questions since Hohenberg and Kohn were not able to explicitly define $T[n(\vec{r})]$ and $U[n(\vec{r})]$ in their energy functional; and as a matter of fact, no one actually could, even today, more than 50 years after the proposal of Hohenberg-Kohn's energy functional. However, the density variational principles together with the basic lemma of Hohenberg-Kohn established a rigorous foundation

upon which Kohn built his 'detour' theory, which did not essentially lead to the exact answers to the above questions but were close enough for many practical purposes and significant enough to win Kohn the Nobel prize.

2.1.4 The Kohn-Sham equations

In the winter of 1964, Kohn returned from France to San Diego, where he met his new postdoctoral associate, Sham. Together, they addressed the Hohenberg-Kohn unsolved key problem. In particular, they rewrote the energy functional, $H[n(\vec{r})]$, in a way that it separates all *unknown* many-body interaction energies from the rest and put them in the so-called *exchange-correlation energy*:

$$H = T[n(\vec{r})]+U[n(\vec{r})]+V_{ext}[n(\vec{r})] = T_0[n(\vec{r})]+J[n(\vec{r})]+E_{XC}[n(\vec{r})]+V_{ext}[n(\vec{r})] \quad (2.9)$$

where, $T_0[n(\vec{r})]$ is the *known* non-interacting kinetic energy which approximates $T[n(\vec{r})]$:

$$T_0[n(\vec{r})] = -\frac{1}{2}\sum_i 2\int \psi_i^* \bigtriangledown^2 \psi_i \quad (2.10)$$

J is the *known* classical Coulomb self potential energy which partially represents the electron-electron interaction, $U[n(\vec{r})]$:

$$J[n(\vec{r})] = \frac{1}{2}\int\int \frac{n(\vec{r}_1)n(\vec{r}_2)}{|\vec{r}_1-\vec{r}_2|}d\vec{r}_1 d\vec{r}_2 \quad (2.11)$$

and, $E_{XC} = T+U-T_0-J$ is the so-called exchange-correlation energy representing all *unknown* many-body interactions from both kinetic and potential energies that are not included in T_0 and J. As Axel D. Becke, an authority in DFT, commented [46]: "*the brilliance of this decomposition is that* T_0 *and* J *are given by exact expressions...*

and that the "unknown" functional, E_{XC}, is relatively small part of the total."

With the new form of the Hohenberg-Kohn's energy functional, Kohn-Sham then took the Hohenberg-Kohn density variational principles followed by the Euler-Lagrange equation, leading to:

$$\delta E_V[n(\vec{r})] = \int \delta n(\vec{r})\{v_{eff}(\vec{r}) + \frac{\delta}{\delta n(\vec{r})} T_0[n(\vec{r})] - \epsilon\} dr = 0 \tag{2.12}$$

where, ϵ is the Lagrange multiplier that corresponds to the constraint that the number of electron in the system is constant, $v_{KS}(r)$ is the Kohn-Sham's effective potential given by:

$$v_{KS}(r) = v_{ext}(r) + \int \frac{n(\vec{r}_2)}{|\vec{r}_1 - \vec{r}_2|} d\vec{r}_2 + \frac{\delta}{\delta n(\vec{r})} E_{XC}[n(\vec{r})] \tag{2.13}$$

Eq. 2.12 essentially leads to the interesting equation:

$$\left(-\frac{1}{2} \bigtriangledown^2 + v_{eff}(\vec{r}) - \epsilon_i\right) \psi_i = 0 \tag{2.14}$$

which is equivalent to the Schrödinger's equation of a single particle moving in an external potential, v_{eff}. Indeed, if we take N and V_{ext} in Eq. 2.4 equal to 1 (one particle) and v_{eff} respectively, U will disappear since there is no electron-electron interaction in a single-body system and the resulting equation will be Eq. 2.14. Eq. 2.14 is known as the *Kohn-Sham equation for an auxiliary single-particle non-interacting system* [47].

Now, assuming that the Kohn-Sham effective potential of a given N-particle system, v_{eff}, was known, the Kohn-Sham equation, Eq. 2.14, could be solved much more efficiently than the many-body Schrödinger's equation, Eq. 2.4, for the wavefunction ψ_i which yields the ground-state electron density of the system as follows:

$$n_0(r) = \sum_{j=1}^{N} |\psi_j(r)|^2 \tag{2.15}$$

The electron density, $n(\vec{r})$, in turn determined the Kohn-Sham effective potential v_{eff}, given that E_{XC} in Eq. 2.13 was known. This essentially establishes a self-consistent system of equations including Eq. 2.14, Eq. 2.15, and Eq. 2.13, which one can solve iteratively (see Fig. 2.1) with an initial guess of $n_0(\vec{r})$ and a given E_{XC} for the ground-state total energy of the system:

$$E_0 = \sum_j \epsilon_j + E_{XC}[n(\vec{r})] - \int \frac{\delta}{\delta n(\vec{r})} E_{XC}[n(\vec{r})] n(\vec{r}) dv - \frac{1}{2} \int \frac{n(\vec{r}_1) n(\vec{r}_2)}{|\vec{r}_1 - \vec{r}_2|} \tag{2.16}$$

and ultimately the contain-it-all wavefunction, ψ_i, which is spectacularly said to explain the whole universe! Is that so? It is true that the ground-state electron density, $n_0(\vec{r})$, and total energy, E_0, resulting from the Kohn-Sham auxiliary equation are identical to the exact values of the many-body Schrödinger's equation. This is because of the fact that the two eigenfunctions, Eq. 2.14 and Eq. 2.4, overall share the same total energy matrix, H, and eigenvalues, E. However, it is not essentially the case that the eigenvectors resulting from the two eigenfunctions are the same since, from linear algebra, it is well known that there are many different eigenvectors corresponding to the same eigenvalue, E, of the matrix, H. Intuitively, a single-particle non-interacting system whose electron density and energy are equivalent to a many-particle interacting system may not necessarily have its particle-waves (ψ_i) travel exactly the same way as those (Ψ) in the many-particle interacting system. Therefore, we can neither guarantee to '*have everything!*' nor '*explain the whole universe!*'. Nevertheless, to understand to a considerable extent the natures of many

things in the universe, just the knowledge of the exact ground-state electron density and, more importantly, the exact ground-state total energy of matter are crucial.

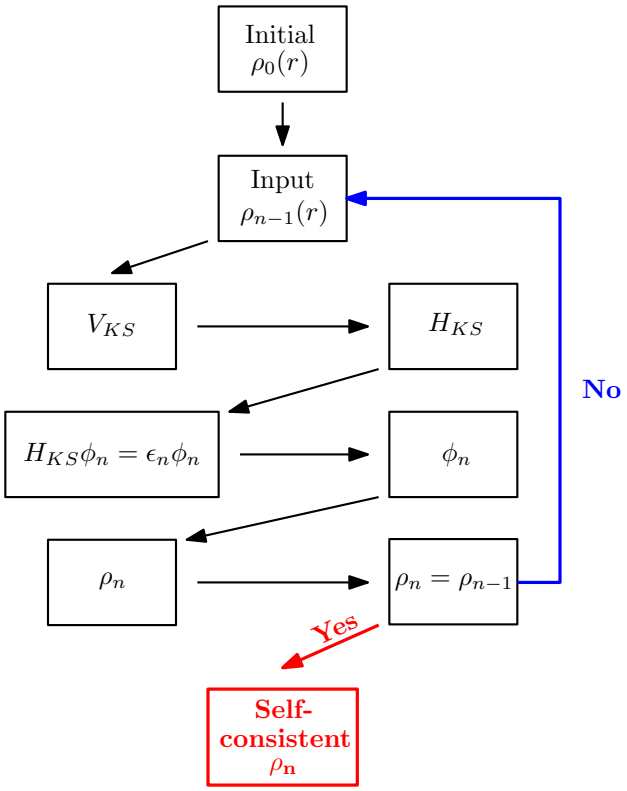

Figure 2.1: Schematic diagram to demonstrate the self-consistent iterative loop to solve Kohn-Sham equation. Here, it is usually started with an initial guess for $n(\vec{r})$, then the corresponding V_s is calculated and the Kohn-Sham equations is next solved for the ϕ_i. The resulting ϕ_i is then used to calculate a new density $n(\vec{r})$. This procedure is then repeated until convergence is reached.

2.1.5 The exchange-correlation approximation

From above, it is obvious that all the fruitfulness of the Kohn-Sham theory emerges from one key condition: the representability of E_{XC}. More than anyone else, Kohn knew that if he could not describe the exchange-correlation potential within

the Kohn-Sham equation, his new theory was not any better than the previous one with Hohenberg. He knew well too that while it is almost impossible to describe the exchange-correlation potential of a real N-particle interacting system, it is doable for the uniform electron gas (UEG). Then, why not use the exchange-correlation of UEG to *approximate* the exchange-correlation of a real N-particle system, knowing that the exchange-correlation potential after all is "*relatively small part of the total*" [46]? This essentially led Kohn and Sham to the so-called local density approximation (LDA) whose formula, including electron spin, reads:

$$E_{XC}^{LSDA}[n_\uparrow, n_\downarrow] = \int \epsilon_{XC}(n_\uparrow, n_\downarrow) n(\vec{r}) d^3r \tag{2.17}$$

To make LDA physically rigorous, Kohn-Sham relied on the normalization condition of the exchange-correlation "hole" [44]: Here, the hole measures the effects of exchange and correlation on the probability of finding an electron at r_2 when the probability of finding an electron at r_1 is $\rho(1)$, and its normalization condition indicates that hole is normalized at all coupling strengths and at all points to -1 electron. Since the normalization condition of the exchange-correlation hole is universal, the same constraint applies to the exact hole a of real system as it applies to the model hole of UEG that replaces it in the LDA. "*The success of the LDA is therefore no surprise at all*," said Becke [46].

With the proposal of LDA, the Hohenberg-Kohn-Sham theory on the electronic structure of matter, as well the memorable story about the birth of one important field in modern physics: DFT, was completed; the story that has been told over and over again until today and for many more years to come and the theory upon which many other important theories and models have been established. These include the projector augmented wave [48] coupled with the special quasi-random structure [49]

and the exact muffin-tin orbital [50, 51] (also remarked as the generalized Korringa-Kohn-Rosteker approach [52, 53]) coupled with the coherent potential approximation [54] which I would be using in the next major section to treat the electronic structures of the random bcc alloys of the uranium-niobium system.

2.2 CALPHAD modeling

2.2.1 Overview

The design of industrial processes requires reliable thermodynamic and kinetic information about the constituent phases, which commonly include gas, liquid, solid solutions, and intermetallic compounds in materials systems. CALPHAD, being originally the CALculation of PHAse Diagram and self-consistent coupling between phase diagram and thermochemistry data, seeks to describe this information on a routine basis. They use mathematical models that are neither empirical nor fundamental but rather encode both experimental and theoretical values in a language that is "*applicable to a much wider context than the original experiments or calculations*", according to the American thermodynamicist Larry Kaufman [55], the godfather of CALPHAD. The '*language*', as it has become evident, is widely used nowadays by many materials scientists and engineers as a powerful tool for materials research and development. In the report on the Integrated Computational Materials Engineering: A Transformational Discipline for Improved Competitiveness and National Security in 2008, the U.S. National Research Council has pointed out that "...*CALPHAD software is arguably the most important (and perhaps the only) generic tool available for ICME practitioners*..." [18] to remark the non-trivial role of CALPHAD in the emerging ICME discipline.

To reach the current stage of fruition, it took the method a considerably long period of time ($\sim$ 70 years) to develop from its embryo concept to the birth and

eventually to maturity and popularity. "*Such a lengthy incubation period between vision and fruition seems very long in retrospect, but is on par with similar developments in other areas of science and technology. It reflects the time taken for individuals to meet each other and agree to work together and also the time taken for the scientific and technological community to devote adequate funds to any new activity,*" said N. Saunders and P. Miodownik in their famous book "CALPHAD (Calculation of Phase Diagram): A Comprehensive Guide" published by Pergamon in 1998 [56]. A fair-and-square comment from the CALPHAD experts in regard to some 15 years of hatching the method before its birth. 15 long years and still this period excluded the time during which CALPHAD was in its early conceptual state, the very beginning that would bring us back to more than a hundred years ago. From here, let us drown a bit in the historical development of CALPHAD, the part which I personally find, in each and every scientific major, very much intriguing and inspiring and, in the following effort to introduce CALPHAD, a great foundational platform. Let us now turn to the first historical page of CALPHAD.

2.2.2 Thermodynamic backgrounds

It all started in 1875 when the famous American scientist Josiah Willard Gibbs published his article entitled "*On the Equilibria of Heterogeneous Substances*" [57]. In this article, Gibbs rigorously formulated the formal concept of chemical potential and rules that related the potentials to their conjugated extensive properties. This concept and rules henceforth became the thermodynamic foundation of phase equilibria, or more relevantly the very soul of CALPHAD.

While it is good to stay with Gibbs's original chemical-potential point of view with regard to his rules and concept, I find it relatively interesting to take a different view from the free-energy perspective. The following thermodynamic equations are

hence presented:

$$\left.\frac{\partial G_\alpha(x,T)}{\partial x_\alpha^{eq}}\right|_{T,p} = \mu_\alpha^{eq} = \mu_\beta^{eq} = \left.\frac{\partial G_\beta(x,T)}{\partial x_\beta^{eq}}\right|_{T,p} \tag{2.18}$$

$$\left.\frac{\partial G_{\alpha,\beta}}{\partial T}\right|_p = -S_{\alpha,\beta} \tag{2.19}$$

$$G_{\alpha,\beta} - T\left.\frac{\partial G_{\alpha,\beta}}{\partial T}\right|_p = H_{\alpha,\beta} \tag{2.20}$$

$$\left.\frac{\partial^2 G_{\alpha,\beta}}{\partial^2 T}\right|_p = -\frac{C_p^{\alpha,\beta}}{T} \tag{2.21}$$

where, $G_{\alpha,\beta}(x,T)$ are the Gibbs free energies of phase α and phase β, respectively; $x_{\alpha,\beta}^{eq}$ are the equilibrium compositions of phase α and phase β at temperature T, respectively; $\mu_{\alpha,\beta}^{eq}$ are the chemical potentials of phase α and phase β at equilibrium, respectively; $S_{\alpha,\beta}$ are the entropies of phase α and phase β respectively, $H_{\alpha,\beta}$ are the enthalpies of phase α and phase β, respectively; and, $C_p^{\alpha,\beta}$ are the heat capacities of phase α and phase β, respectively. Here, the first equation is the Gibb's equilibrium condition and represents Gibbs's concept. The last three equations are representatives of the thermodynamic relations between Gibbs free energy and extensive variables, hence Gibbs's rules.

Now, given that the functional form of Gibbs free energy was known explicitly, the significance of the above Gibbs-based thermodynamic equations to CALPHAD modeling would become obvious: They allow the estimations of equilibrium compositions at arbitrary temperature (Eq. 2.18), hence the ultimate construction of (temperature-composition) phase diagram. They allow, in conjunction, the investigations of various thermodynamic properties of materials (Eq. 2.19 – Eq. 2.21), and hence the self-consistent coupling between phase diagram and these thermochemistry data [58]. They thus give rise to CALPHAD (refer to overview for definition of

CALPHAD).

That said, how to describe these Gibbs-energy functions in the first place? A very interesting question that would essentially lead us to the modeling nature of CALPHAD. There are many different ways to answer this question, and the way that I would like to, is as follows: There are three conceptual approaches to describe the Gibbs-energy functions. The (troublesome) 'Good' approach is to fundamentally derive them from well-established theories in basic sciences, e.g. condensed matter physics and chemistry. The (charming) 'Bad' approach is to give up all complex physical backgrounds and empirically postulate their parameterized expressions, e.g. $G = (a_1+b_1T)x+(a_2+b_2T)x^2+(a_3+b_3T)x^3$, which fit well to available experimental and first-principles values. And, the (attractively menacing) CALPHAD is to be neither fundamental nor empirical... Guess what? History chooses CALPHAD.

2.2.3 Historical thermodynamic modeling

2.2.3.1 Regular solution model

Some thirty years after Gibbs's formulation saw the works of van Laar (a Dutch chemist) [59, 60], in which he sculpted out the original form of CALPHAD and put into it the soul from Gibbs. In particular, van Laar derived an algebraic expression to describe the Gibbs free energy of solution phases based on his teacher's equation, van der Waals's equation of state. Before showing van Laar's derivation, it should be noted that by his time it was fairly common to express the Gibbs free energy of an arbitrary solution ϕ, G^{ϕ}, in the following general form:

$$G^{\phi} = G^{0} + G^{ideal} + G^{xs} \tag{2.22}$$

Here, G^0 is the Gibbs free energy of constituents of ϕ, also commonly known as the Gibbs free energy of end-members. It is subjected to an important concept

of CALPHAD and, in van Laar's derivation, was actually formulated as a linear combination of constituents' Gibbs free energies, $G_i^0(T)$:

$$G^0 = \sum_i^N x_i G_i^0(T) \tag{2.23}$$

where, N is the number of constituents and $G_i^0(T)$ have explicit mathematical descriptions; however, its significance was only truly appreciable much later by Meijering in a different context. We, therefore, acknowledge the existence of G^0 for the moment and save its discussion for sometime later.

G^{ideal} is the so-called Gibbs free energy of ideal mixing. It is defined for solutions that resemble ideal gases. In such solutions, the interactions between the constituents of solutions are trivial and normally ignored. The enthalpy of mixing is hence zero, and the Gibbs free energy therefore depends only on the entropy of mixing:

$$G^{ideal} = H^{ideal} - TS^{ideal} = -TS^{ideal} \tag{2.24}$$

where, T is temperature, and the entropy of ideal mixing, S^{ideal}, is the configurational entropy which depends on the configurational degrees of freedom of constituents. Within statistical mechanics, this entropy has a solid fundamental backgrounds:

$$S^{ideal} = k\ln W_P = -Nk\sum x_i \ln x_i = -R\sum x_i \ln x_i \tag{2.25}$$

with k is the Boltzmann's constant and $W_P = \frac{N!}{\prod_i n_i!}$ is the number of configurations, $R = Nk$ is the gas constant, and x_i is the model fraction of component i. The profound functional form of G^{ideal} is hence:

$$G^{ideal} = RT\sum_i^N x_i \ln(x_i) \tag{2.26}$$

The last term in Eq. 2.22, G^{xs}, is the so-called excess Gibbs free energy of mixing. It represents the interactions of constituents beyond ideal solutions, hence is attributed to the non-trivial enthalpy of mixing. Due to its complicated nature, fundamental description of G^{xs} is very much limited and needs to be restated, and van Laar was amongst the first to show this. He started with his teacher's equation of state, which can be cast in terms of excess Gibbs free energy, as follows:

$$\begin{aligned} \frac{G^{xs,vdW}}{RT} &= \sum_i^N x_i \ln\left(\frac{V_i - b_i}{V - b}\right) + \frac{1}{RT}\left(\sum_i^N x_i \frac{a_i}{V_i} - \frac{a}{V}\right) \\ &= \sum_i^N x_i \ln\left(\frac{\Phi_i^{fv}}{x_i}\right) + \frac{V}{RT}\Phi_i\Phi_j(\delta_i - \delta_j)^2 \end{aligned} \tag{2.27}$$

where,

$$\Phi_i^{fv} = \frac{x_i(V_i - b_i)}{\sum_j^N x_j(V_j - b_j)} \tag{2.28}$$

$$\Phi_i = \frac{x_i V_i}{\sum_j^N x_j V_j} \tag{2.29}$$

$$\delta_i = \frac{\sqrt{a_i}}{V_i} \tag{2.30}$$

in which, a_i and b_i are van der Waals's parameters that represent the measure of attraction between articles and volume excluded by a mole of particles of each constituent, respectively, and V_i is the volume of the constituent (note that the same parameters without subscripts are for the system). With the assumptions that V_i can be approximated by b_i and the excess entropy of mixing and excess volume are zero, van Laar neglected the first term in the above equation and, after substituting Φ_i^{fv}, Φ_i, δ_i, and $V = \sum_j^N x_j b_j$, acquired his approximation for the excess Gibbs free energy, G^{xs}:

$$G^{xs,vL} = H^{xs,vL} = \frac{b_i x_i b_j x_j}{\sum_j^N x_j b_j} \left(\frac{\sqrt{a_i}}{b_i} - \frac{\sqrt{a_j}}{b_j} \right)^2 \tag{2.31}$$

where, $H^{xs,vL}$ is the excess enthalpy of mixing. van Laar realized that by using the physical parameters introduced by van de Waals, his energy function does not yield satisfactory results in comparison to experiment. He therefore reduced the above equation to:

$$G^{xs,vL} = \frac{A_{ij} x_i A_{ji} x_j}{\sum_i^N A_{ji} x_j} \tag{2.32}$$

and fit the empirical A_{ij} to experimental values, which essentially made his derived excess enthalpy of mixing a semi-empirical term.

By combining the excess, ideal, and constituent terms together, van Laar achieved his final Gibbs-energy function for solution phases:

$$G^{\phi} = \sum_i^N x_i G_i^0 + RT \sum_i^N x_i \ln(x_i) + \sum_i^N \sum_{j>i}^N \frac{A_{ij} x_i A_{ji} x_j}{\sum_i^N A_{ji} x_j} \tag{2.33}$$

in which the pair-interactions of constituents i and j were superimposed in the excess term according to van der Waals's mixing rule.

If we now define the interaction parameter Ω_{ij} to be:

$$\Omega_{ij} = \frac{A_{ij} A_{ji}}{V} \tag{2.34}$$

with $V = \sum_i^N A_{ji} x_j$, van Laar's Gibbs-energy function can be rewritten as follows:

$$G^{\phi} = \sum_i^N x_i G_i^0 + RT \sum_i^N x_i \ln(x_i) + \sum_i^N \sum_{j>i}^N \Omega_{ij} x_i x_j \tag{2.35}$$

This expression that features well the semi-empirical character of CALPHAD was

the very first CALPHAD formulation of the Gibbs-energy function G^{ϕ}. It was latter regarded by Hildebrand as the regular solution model due to its assumption of zero excess entropy of mixing.

van Laar applied this model to describe the free energies of solution phases in some hypothetical binary systems and then used Gibbs's rules to evaluate the phase diagrams of those systems. Even though van Laar did not have the essential inputs corresponding to real systems for his algebraic expression to elevate his evolutionary idea, he was very successful in demonstrating that phase diagrams of real systems could be obtained from thermodynamic data by equilibrium calculations, i.e. the concept of CALPHAD.

After van Laar, the CALPHAD concept stayed dormant for many following years due partly to the scarcity of thermochemistry data, the limitations of hand-calculations of phase diagrams to simple binary systems and the unavailability of the computer, and especially to the "*alternative more physical approach based on band-structure calculations*" which "*appeared likely to rationalise many hitherto puzzling features of phase diagrams [61],*" as pointed out by Saunders and Miodownik [56]. It was not until the 1950s when van Laar's work was finally taken further by Meijering, a Dutch metallurgist, with his calculations of miscibility gaps in ternary [62], quaternary systems [63], and more...

2.2.3.2 Lattice stability

In 1957, Meijering became the first to calculate a complete ternary phase diagram of a real system, i.e. the Ni-Cr-Cu system [64]. During his initial effort, Meijering faced an interesting problem. In particular, when he tried to describe the Gibbs free energy of the face-centered-cubic (fcc) Ni-Cr-Cu which, according to Eq. 2.35, reads:

$$
\begin{aligned}
G^{fcc} &= x_{Ni}G^{o}_{Ni}(x,T) + x_{Cr}G^{o}_{Cr}(x,T) + x_{Cu}G^{o}_{Cu}(x,T) \\
&\quad + RT(x_{Ni}\ln(x_{Ni}) + x_{Cr}\ln(x_{Cr}) + x_{Cu}\ln(x_{Cu})) \\
&\quad + \beta_{NiCr}x_{Ni}x_{Cr} + \beta_{NiCu}x_{Ni}x_{Cu} + \beta_{CrCu}x_{Cr}x_{Cu} \qquad (2.36)
\end{aligned}
$$

where, G^{o}_{Ni}, G^{o}_{Cr}, and G^{o}_{Cu} are respectively the Gibbs free energies of fcc Ni, Cr, and Cu, Meijering realized that he did not have any information on fcc Cr since this crystal structure was not directly accessible by experiments. A natural need to relate fcc Cr to something more available like bcc Cr in order to describe the Gibbs free energy of fcc Ni-Cr-Cu then arose. This need essentially led to the concept of lattice stability which can be defined as the difference in Gibbs formation energy between the two different crystal structures of the same material. The importance of this concept and the essence to accumulate lattice-stability values was later emphasized by Kaufman and since then has been gradually recognized and appreciated throughout the historical development of CALPHAD. In 1991, the Scientific Group Thermodata Europe (SGTE) published their remarkable collection of the lattice stabilities of pure elements. To encode these lattice-stability values, SGTE used the following polynomial:

$$
G^{0}(T) - H^{SER} = a + bT + cT\ln(T) + \sum_{2}^{n} d_n T^n \qquad (2.37)
$$

in which, the right left hand side of the equation is the lattice stability of a pure element with respect to its reference state, H^{SER}_{m}, defined at 298.15 K; a, b, c, d_n are coefficients; and, n represents a set of integers whose typical values are 2, 3, -1, 7, and -9. This polynomial has also been commonly used to describe the Gibbs free

energies of intermetallic compounds.

As shown by Saunders and Miodownik [56], the attempt of Meijering was particularly significant for the fact that it pioneered the introduction of the concept of lattice stabilities, which, as Meijering realized, are essential to make the calculations of phase diagrams possible. Later in 1981, Kaufman, who was recognized at that moment as the leader of the CALPHAD community, wrote an excellent article entitled: "J.L. Meijering's Contribution to the Calculation of Phase Diagram - A Personal Perspective" [65] to acknowledge Meijering for his non-trivial contributions to the CALPHAD approach. In this article, Kaufman wrote:

> "*During the 1950s the present author had the benefit of studying with Wagner, Chipman, and Cohen, reading the work of Zener, Kubaschewski, Darken and Meijering, and having student colleagues such as Hillert, Hilliard and Cahn with whom one could argue and disagree. Notwithstanding the fact that all of these individuals contributed substantially to the author's appreciation of the interaction between thermochemistry and phase diagrams, none had a greater impact than J.L. Meijering.*"

2.2.3.3 The birth of CALPHAD thermodynamic modeling

Now, it is noted that the early effort to promote the CALPHAD concept in the 1950s was not a singularity in Europe but was complemented by the developments in the USA. As has become unsurprising to us up until this moment, among the US pioneering CALPHAD workers was Kaufman. It was a year after he got his Sc.D. from the Massachusetts Institute of Tecnology (MIT) in 1955, that Kaufman published a paper co-authored with his advisor Morris Cohen to present their work on the calculation of Fe-Ni phase diagram [66]. In this paper, Kaufman and Cohen used the regular solution model to encode the experimental phase diagram information

at high temperatures and the martensitic transformation at low temperatures and found satisfactory results in comparison with experiments. Like Meijering's work, this paper of Kaufman was an important contribution to the early development of CALPHAD. To Kaufman, the paper historically marked the beginning of his career as one whose "*enthusiastic and inspiring leadership*", according to Kaufman's colleague Philip Spencer [67], had contributed "*in no small measure*" to the success of the CALPHAD method and more significantly the CALPHAD community.

Besides being the indubitable professional in computational thermodynamics, Kaufman had the passion and keenness that were key to the birth and growth of CALPHAD, which perhaps was best described by Saunders and Miodownik as [56]: "*the single-minded determination*" that combined the link of CALPHAD to practical problems associated with steels [66, 68], the vision of producing extensive database for the calculations of phase diagrams on a permutative basis, and the gathering of all major workers in the field world-wide. With these Kaufman had been persistent throughout his career life from the very beginning [66] to the very end [55]. The present historical review, not to be compared with the excellent reviews of predecessors [56, 69, 67], is dedicated to the memory of professor Larry Kaufman (1930 - 2013), whose legacy lives now and will for many years in the CALPHAD community.

After his significant contribution in 1956, Kaufman continued persistently to promote the CALPHAD concept to the scientific community of phase equilibria and phase diagrams (or perhaps more precisely to fight for the public acceptance of the innovative method). He had to face unavoidable opposite opinions, especially from the experimentalists who considered CALPHAD (initial) calculations too inaccurate and the band-structure theorists who were concerned about the differences in lattice stabilities between the CALPHAD method and the supposed-superior first-principles calculations. Not so surprisingly, there were times when Kaufman was discouraged;

he wrote, in a letter to Brewer [70] after the Battelle meeting convened in 1958 by the U.K. National Physical Laboratory (NPL):

> "*there have been the same tired old band theory discussions and little seems to have happened over the last thirty years; the attendees do not seem to be aware of the most important directions for attacking the problem.*"

Regardless of hurdles, Kaufman continued working hard with focus on steel alloys as he realized that these complex systems were where the band-structure calculations fell short and where the CALPHAD method would show its superiority. During these early years, Kaufman had also started constructing the thermodynamic database consisting of regular-model parameters for various binary and ternary alloy systems which he knew would come handy. These data were to be listed in his famous book devoted to CALPHAD many years later. In 1959 Kaufman published another important paper [71] in which he illustrated the importance of lattice stabilities in phase-diagram calculations.

In 1960 when Kaufman chaired an AIME meeting on Phase Equilibria, he first met Hume-Rothery, a famous English metallurgist and material scientists who spent most of his life on the accurate determination of experimental phase diagrams. Bilateral contact was then established between Kaufman and Hume-Rothery and lasted for 6 years until they met again in Geneva at the Battelle conference on Phase Stability of Metals and Alloys. There, Hume-Rothery invited Kaufman to write a review on the stability of metallic phases as seen from the CALPHAD viewpoint for Progress in Materials Science (PMS) which Hume-Rothery edited. This led to more correspondence by mail exchanges between Kaufman and Hume-Rothery during the next 30 months. During this time, the two discussed various aspects regarding phase equilibria in relation to the emerging CALPHAD that Kaufman had in mind, and

Hume-Rothery proved to be a fair but demanding editor. His view was that while he was "*not unsympathetic to any theory which promises reasonably accurate calculations of phase boundaries, and saves the immense amount of work which their experimental determination involves,*" [61] "*it would be difficult to persuade him that such calculations represented real progress and that the methodology should be included in the proposed review*" [56]; interestingly, he concluded "*however I would like to be convinced of the contrary!*" [61]. Kaufman took the time and opportunity working with Hume-Rothery to "*restate his position*" [56] and refine his views. Outcomes were three cores: the emphasis on the competition between all principal phases, the provision of realistic descriptions which could be applied to many systems, and the availability of a numerical inputs which could provide quantitative descriptions applicable over a wide range of temperature, composition and pressure. Through out these cores Kaufman sought to stress the important concept of lattice stabilities and the essence of thermodynamic databases. These all were very well reflected in his appointed review which was published in 1969 on the famous PMS journal [72]. And, to double their impacts the next year saw the publication of Kaufman's book, a promotion from his review, written with Bernstein. This was the very first textbook devoted to the CALPHAD method and its appeal was shown by its translations into different languages and as the source of inspiration for many researchers. With this book Kaufman established the very foundation upon which he gave birth to CALPHAD as both a method and shortly after a community, ending the long period of about 60 years of breeding its embryo concept.

2.2.3.4 Sub-regular solution model

Notably, in his book, to mark the new stage of CALPHAD development Kaufman proposed the usage of sub-regular solution model in which the composition-

dependence of interaction energies was taken into account. The consideration that was missed in the regular solution model and hence made it too simplistic and less applicable. In Kaufman's initiating effort, the excess Gibbs free energy was assumed to depend linearly on composition, as follows:

$$G_{mix}^{xs} = \sum_{i}^{N} \sum_{j \neq i}^{N} x_i x_j (\Omega_{ij}^{i} x_i + \Omega_{ij}^{j} x_j) \tag{2.38}$$

Later developments considered more complex composition dependencies which were generally expressed in term of a power series. The most common method is based on the Redlich-Kister equation which generalizes Kaufman's sub-regular solution model into:

$$G_{mix}^{xs} = \sum_{i}^{N} x_i G_i^0 + RT \sum_{i}^{N} x_i \ln(x_i) + \sum_{i}^{N} \sum_{j>i}^{N} x_i x_j \sum_{\nu} \Omega_{ij}^{\nu} (x_i - x_j)^{\nu} \tag{2.39}$$

where, ν usually does not exceed 3 and in case $\nu_{max} = 0$ the above equation reduces to that of the regular solution model. The interaction parameter Ω_{ij}^{ν} is temperature-dependent and usually expressed in term of the SGTE polynomial (see Eq. 2.37).

Sub-regular solution model is mainly used in metallic alloy systems to model substitutional phases such as liquid, bcc, and fcc. Since, these phases are native to alloy systems and these systems comprise an important class of materials, sub-regular solution model establishes itself as one of the most impactful models within CALPHAD modeling.

2.2.3.5 Sublattice model

Now, it is noted that during these years when Kaufman strove for the public acceptance of CALPHAD, other major workers in the field also delivered their sig-

nificant contributions. For instance, Kubaschewski and Chart wrote an important paper in which they summarized essential mathematical steps for constructing phase diagrams [73] in 1965. This paper then became the source of inspiration for the development of a commercial package at NPL, U.K for assessing thermodynamic properties of materials. Later, Kubaschewski moved to Germany and, with Ihsan Barin, started up a new group at RWTH, Aachen where he continued to contribute more to the formation of CALPHAD. In Sweden, Mats Hillert, a student colleague of Kaufman at MIT, built his own CALPHAD programme after being appointed to the Royal Institute of Technology, Stockholm (also known as KTH) in 1961. He was very successful in making CALPHAD a key feature of the Physical Metallurgy department at KTH as well as getting support from both governmental and industrial partners for its research activities. In the mid-1960s, through his programme Hillert established a collaboration with a group of experimentalists from Tohoku University at Sendai who on their return to Japan brought back the CALPHAD seed and planted it there.

In 1970, Hillert and Staffansson proposed the important two-sublattice version of the regular solution model [74], which took into account some ordering tendencies in alloy systems. Sublattice model features the partial occupancies of components at each atomic site within a crystal structure. It can be seen as a generalized form of the random substitutional model since it does allow a fully-random site occupancy of each component, which is the case of the random sublattice model. The partial site occupancy of each component is commonly indicated as site fraction, which for each component is given as follows:

$$y_i^s = \frac{n_i^s}{n^s} \tag{2.40}$$

where, n_i^s is the number of atoms of component i occupy sublattice s and N^s is the total number of sites on the sublattice s. In case vacancies get involved, e.g. interstitial phases, the above description for site fraction turns into:

$$y_i^s = \frac{n_i^s}{n_{Vac}^s + \sum_i n_i^s} \tag{2.41}$$

with n_{Vac}^s is the number of vacancies on sublattice s. From the site fraction, mole fractions can be directly calculated according to the following one-way relationship:

$$x_i = \frac{\sum_i N^s y_i^s}{\sum_s N^s (1 - y_{Va}^s)} \tag{2.42}$$

Here, the word 'one-way' was used to signify the fact that the inverse relationship, $y_i = f(x_i)$, is system dependent and not always straightforward to be derived. In many practical applications, such an inverse relationship is more necessary and has to be achieved numerically, i.e. free-energy minimization with constraints.

With y_i^s replacing x_i, Hillert and Staffansson had to redefine the constituent, ideal, and excess terms in Eq. 2.22. For the case of two-sublattice $(A, B)_1(C, D)_2$ crystal structures with A, B, C, and D components, the constituent term was given as follows:

$$G^0 = y_A y_C G_{AC}^0 + y_A y_D G_{AD}^0 + y_B y_C G_{BC}^0 + y_B y_D G_{BD}^0 \tag{2.43}$$

where, G_{AC}^0, G_{AD}^0, G_{BC}^0, and G_{BD}^0 are Gibbs free energies of end-members, i.e. AB, AC, BC, and BD crystal structures, respectively. This expression can be rewritten in a shorter format as follows:

$$G^0 = \sum_{I0} P_{I0}(Y)^0 G_{I0}^{\phi} \tag{2.44}$$

where, P_{I0} represents the corresponding product of site fractions when each sublattice is occupied by only one component. G^{ϕ}_{I0} is the Gibbs energy of the compound defined by I in phase ϕ. The ideal entropy of mixing in this case is given by:

$$G^{ideal} = RT \sum_{s} N^{s} \sum_{i} y_i^s \ln(y_i^s) \tag{2.45}$$

And, the excess energy of mixing, for the case of non-ideal mixing, is:

$$G^{xs} = y_A^1 y_B^1 y_C^2 L^0_{A,B:C} + y_A^1 y_B^1 y_D^2 L^0_{A,B:D} + y_C^1 y_D^1 y_A^2 L^0_{A:C,D} + y_C^1 y_D^1 y_B^2 L^0_{B:C,D} \tag{2.46}$$

where, $L^0_{A,B:C}$, $L^0_{A,B:D}$, $L^0_{A:C,D}$, and $L^0_{B:C,D}$ are composition-dependent, as follows:

$$L^0_{A,B:C} = y_A^1 y_B^1 y_C^2 \sum_{\nu} L^{\nu}_{A,B:C} (y_A^1 - y_B^1)^{\nu} \tag{2.47}$$

$$L^0_{A,B:D} = y_A^1 y_B^1 y_D^2 \sum_{\nu} L^{\nu}_{A,B:D} (y_A^1 - y_B^1)^{\nu} \tag{2.48}$$

$$L^0_{A:C,D} = y_C^1 y_D^1 y_A^2 \sum_{\nu} L^{\nu}_{A:C,D} (y_C^1 - y_D^1)^{\nu} \tag{2.49}$$

$$L^0_{B:C,D} = y_C^1 y_D^1 y_B^2 \sum_{\nu} L^{\nu}_{B:C,D} (y_C^1 - y_D^1)^{\nu} \tag{2.50}$$

Similar to the constituent term, the excess Gibbs energy of mixing can be written in a shorter format as follows:

$$G^{xs} = \sum_{Z>0} \sum_{IZ} P_{IZ}(Y) L^{\phi}_{IZ} \tag{2.51}$$

where, P_{IZ} is the site fraction product when only one sublattice contains Z components and the remaining sublattices are occupied by one component, and its cor-

responding L^{ϕ}_{IZ} denotes the interaction between the components. The total Gibbs energy of sublattice phases, thus, is given as:

$$G^{\phi} = \sum_{I0} P_{I0}(Y)^0 G^{\phi}_{I0} + RT \sum_{s} N^s \sum_{i} y^s_i \ln(y^s_i) + \sum_{Z>0} \sum_{IZ} P_{IZ}(Y) L^{\phi}_{IZ} \qquad (2.52)$$

This model was later generalized by Bo Sundman and John Ägren, students of Hillert, for any number of components and sublattices [75] and henceforth became a powerful model for treating systems with complex crystallography and for various ordering phenomena [76].

2.2.3.6 The growth of CALPHAD thermodynamic modeling

Now, it is noted that all of these efforts, although significant in their own way, did not much advance the formation of CALPHAD efficiently. The reason for this was that each major worker at that moment had their own way of representing and promoting computational thermodynamics which ended, from the macroscopic point of view, as small scattering efforts, if not duplicated, rather than one big unifying contribution. Gathering these major workers was therefore crucial for the advance of CALPHAD at that moment. Seeing through this, in 1973 Kaufman collaborated with Himo Ansara from the University of Grenoble, France to organize the very first CALPHAD meeting at ManLabs, where Kaufman was working, in Boston, USA. The aim of the meeting was to exchange ideas, discuss specific problems in computational thermodynamics, and, if possible, coordinate the activities between/among different major groups on the thermodynamic assessments of alloy phase diagrams. In the letter he sent out to potential participants, Kaufman clearly stated his viewpoint:

"*We are at present all using different computer methods to obtain tie-line so-*

lutions. We are also using slightly different formulations for the excess Gibbs energy of solution. In some cases the differences may be more semantic than real, but in any case, if we can all employ equivalent computer programmes, we could concentrate on the problem of defining system parameters in order to achieve universal interchangeability of results."

Positively, he suggested:

"*We believe that substantial progress can be made in a short period of time if we could arrange to work together for one week at one of our facilities to define problems, disband, carry out some individual activities and meet again for a week at a second facility to compare results and chart future activities.*"

Attending the first CALPHAD meeting that year were Himo Ansara and Claude Bernard from LTPCM, ENSEEG, Grenoble, France, Oswald Kubaschewski and Ihsan Barin from RWTH Aachen, Germany, Philip Spencer and Jack Counsell from NPL, Teddington, UK, Mats Hillert and Gernot Kirchner from KTH, Stockholm, Sweden, Harvey Nesor from ManLabs, John Cahn later at MIT, Dick Weiss from AMMRC Watertown, and Claude Lupis from Carnegie Mellon University in Pittsburgh. Topics being discussed during the meeting included thermodynamic assessments of pure elements, binary, and ternary systems, the analysis of interaction models, and the modeling of magnetic contributions. All these were best summarized in the historical review by Philip Spencer [67], who also attended the first CALPHAD meeting. And, just to show the seriousness and intensity of these discussions Spencer mentioned, in his review [67]:

"*... the meeting was both stimulating and exhausting, with all sessions taking place in a windowless room to promote concentrated discussion! Lunch bags*

provided the only slight distraction from the continuous scientific exchanges. As Ihsan Barin put it later – "it was a little like one might imagine a thieves' kitchen to be, but in this case with calculated phase diagrams being pushed around the table and three or four binaries being offered for one ternary."..."

At the end of the day, the first CALPHAD meeting was a big success. It successfully promoted the collaborations among major workers. It strongly established the foundation for the next CALPHAD meeting to be held in Grenoble in 1974 and many more to come in the following years. And, above all it historically marked the dawn of the CALPHAD community.

With the newborn CALPHAD to be nurtured, it would be difficult to maintain its activities and further expand its potentials without a dedicated source of long-term financial support. To deal with this, in 1975 Kaufman established CALPHAD Inc., a non-profit-making organization duly incorporated in Massachusetts. As one of the early fund-raising options, CALPHAD Inc. pursued the possibility of publishing a journal. It eventually came to an agreement with Pergamon Press and the CALPHAD journal was first issued in 1977. In the following years, under Kaufman's leadership, CALPHAD gradually established itself as a widely accepted tool for thermodynamic assessment in the field of materials science and engineering. This was shown in the changes in the opinions of experimentalists and theorists who previously suspected the CALPHAD method. As for the experimentalists, since the accuracy of CALPHAD assessments have been considerably improved with more and more reliable thermochemistry inputs available now than before, more and more experimentalists have turned to the method and literally used it to guide their experiments. As for the theorists, through conferences and workshops that were dedicated for the liaison between CALPHAD and band-structure calculations, workers from the two

fields have gradually found their common language, i.e. the self-consistent coupling between CALPHAD and first-principles calculations that has been highly encouraged in recent years due to its reliable and consistent outputs. Within the CALPHAD field, collaborations between workers have been greatly improved, especially with the encouragement and support from Kaufman and CALPHAD Inc. The CALPHAD method has become more popular. Research activities have been much more active. More and more works have been sent to the CALPHAD journal every year for consideration. A majority of them contributed to the compilation of thermodynamic data banks, e.g. the Scientific Group Thermodata Europe (SGTE) for lattice stabilities of pure elements [77]; many seek to propose new thermodynamic models, e.g. the aforementioned generalized sub-lattice model of Sundman and Ägren [75]; others investigated numerical aspects for dealing with thermodynamic data and models, e.g. efficient minimizations of Gibbs free energy or optimizations of model parameters. Not so surprisingly, during these years there was a rapid increase in the number of computer codes, both commercial and open-source, devoted to computational thermodynamics. To name a few, MTDATA [78] developed at NPL in England, FactSage [79] and SOLGASMIX [80] developed by Canadian workers, BINGSS by Lukas in Germany, and ThermoCalc by Hillert's group in Sweden. What's next?

2.2.4 Modern CALPHAD extensions

2.2.4.1 Kinetic modeling

The year 1992 saw the remarkable extension of CALPHAD modeling to the field of kinetic diffusions by Andersson and Ägren [42]. In their work, Andersson and Ägren start with a fundamental expression of atomic mobility:

$$M_k = \frac{1}{RT} \exp\left(\frac{\Phi_k}{RT}\right), \tag{2.53}$$

where, R is the gas constant and T is temperature; In the spirit of CALPHAD, they then expanded Φ_k in term of the Redlich-Kister polynomial:

$$\Phi_k = \sum_i x_i \Phi_k^i + \sum_i \sum_{j>i} x_i x_j \left[\sum_r {}^r\Phi_k^{i,j} (x_i - x_j)^r \right], \tag{2.54}$$

in which, Φ_k^i is the mobility of end-member; x is molar fraction; And, ${}^r\Phi_k^{i,j}$ is interaction parameter. As in the case of CALPHAD thermodynamic modeling, these parameters can be optimized in such a way that the resulting atomic mobility can in turn yield calculated diffusivities that are comparable with experimental data. This is realized according to the fundamental relationships between diffusion coefficients and atomic mobilities which were defined in Andersson and Ägren work. These relationships include first the so-called interdiffusivity [42]:

$$D_{ij}^n = \sum_{k=1}^{n} (\delta_{ik} - x_i) x_k M_k \left(\frac{\partial \mu_k}{\partial x_j} - \frac{\partial \mu_k}{\partial x_n} \right), \tag{2.55}$$

where δ_{ik} is the Kronecker delta ($\delta_{ik} = 1$ if $i = k$; otherwise $\delta_{ik} = 0$), and μ_k is the chemical potential of element k. The intrinsic diffusivity can also be written in term of atomic mobility as follows:

$${}^I D_{ij}^n = x_i M_i \left(\frac{\partial \mu_k}{\partial x_j} - \frac{\partial \mu_k}{\partial x_n} \right), \tag{2.56}$$

And the tracer diffusivity is expressed as:

$$D_i^* = RTM_i. \tag{2.57}$$

To show the applicability of their models, Andersson and Ägren developed a package called DICTRA in which they incorporated their assessed kinetic data with a sharp-interface model to investigate different dynamical processes such as diffusion

couples, coarsening, segregations, cooperative growths etc.

2.2.4.2 Other extensions

The extension of CALPHAD modeling to the field of kinetic diffusions showed how versatile the CALPHAD method, as being neither empirical nor fundamental, can be. And if it was not already evident, in some recent years, efforts have already been undertaken to further extend the method to the modelings of crystal lattice constants, interfacial energies, and elastic energies [81]. Taking Lu *et al.* [82] as an example, the molar volume is defined for nonmagnetic system, as the following:

$$V_m = V_0 \exp\left(\int_{T_0}^{T} 3\alpha dT\right) \tag{2.58}$$

where, V_0 is the molar volume at reference temperature T_0 (usually 298.15 K), and α is the linear expansion coefficient. In the spirit of CALPHAD, α is expressed as:

$$\alpha = \frac{1}{3}(a + bT + cT^2 + dT^{-2}) \tag{2.59}$$

where the constants a, b, c, and d are evaluated using available data from lattice-parameter expansion.

Clearly, the CALPHAD method has finally reached to its maturity and this without doubt is due to the persistent efforts and contributions from the early workers among whom Larry Kaufman showed his great enthusiastic and inspiring leadership. From here, what is more to tell will be left for the future generation of CALPHAD, who will have the right to turn to the newer pages of the CALPHAD history book that are being written by the current generation. What is left to refine is the inspiration sublimated from seeing how a new scientific approach has come to blossom and eventually fruition from its conceptual seed. And, as the prescient lecture of

professor Köster had previously echoed to Saunders and Miodownik [56], I also find it touches me:

> "*It is fascinating to trace the devious paths a research worker may have followed before he arrived at his final knowledge and discoveries. Sometimes it may be the gradual perfection of experimental apparatus or the systematic pursuit of an idea; on other occasions success may arise from the deliberate solution of a problem only he believes possible at all, or the recognition of the importance of some apparently insignificant factor; it may even be the appreciation of a phenomenon already known, but completely neglected; or again success may come simply by sudden inspiration, or as the outcome of a long, patient and plodding series of experiments... But one thing is common to all true research. Its results are won in the course of unceasing, stubborn wrestling with problems in the service of knowledge... For each deeper insight, each original discovery, arises not only from cool calculation but is also the outcome of creative force and imaginative perception.*"..."

2.3 Phase-field modeling

2.3.1 Overview

It has been well established and manifested within the field of materials science by its so-called *processing-structure-property-performance* paradigm that the properties and performance of a material are strongly dependent on its microstructure. This practically translates to the fundamental engineering problem that the design process of a material for some preferential properties and performance requires the manipulation of that material's microstructure, which in turn requires substantial understanding of the microstructure's evolutionary process, that for instance is solidification, solid-solid phase transformation, or grain growth. The phase-field method,

to this end, provides a practically efficient and reliable solution for the studies of arbitrarily complicated microstructural evolution in materials.

Then, what makes the fruition of phase-field modeling? To my understanding, the two seeds: (1) the phase-field concept and (2) its realization into a rigorous physical model. Before analyzing these seeds, let us first spend some time to briefly describe the history of phase-field modeling as one way to acknowledge the method as well as appreciate the earlier workers who had contributed non-trivially to its birth and growth:

The concept of phase-field modeling spreads its roots more than a century ago when van der Waals [83] proposed to model a liquid-gas interface by means of a density function that varies continuously across the interface. Many years after, van der Waals's idea started being adopted among the later generation of scientists beginning with Cahn and Hilliard [84] who proposed a thermodynamic formulation that accounts for the gradients in thermodynamic properties in heterogeneous systems, Ginzburg and Landau [85] who formulated a model for superconductivity using a complex valued order parameter and its gradients, and shortly after Hohenberg and Halperin [86] and Gunton et al. [87] in their stochastic theory of critical dynamics of phase transformations. Although significant in establishing what later became the fundamentals of the phase-field method, these early works however did not make the practical impact that was needed to give an official birth to the method as a new scientific field.

In the McWasp conference in 1993 on "the Modeling of Casting, Welding and Advanced Solidification Processes VII" in Palm Coast, Florida, Kobayashi stunned many scientists attending the conference at that moment with his remarkable video on the simulation of dendritic growth. The reason for Kobayashi's impact was as follow: the modeling of dendritic grow was previously considered a very difficult

task due to the complicated morphology of this microstructure; many conventional models, the so-called sharp-interface models, resulted in complex mathematical formulation which was computational expensive and did not essentially produce a morphology as realistic as the one of Kobayashi; Kobayashi's model [88], making use of the phase field $\phi(\vec{x}, t)$ to distinguish liquid ($\phi = 0$) from solid ($\phi = 1$), was however strikingly simple both in formulation and implementation. Its simulation result was simply gorgeous; its capability was impressive; it had marked the beginning of the phase-field method as an interesting new field.

Note that even though Kobayashi's model was remarkable, its derivation was somewhat ad hoc. This unavoidably led to a doubtful wave spreading among many scientists who were concerned about the authenticity of the method. Not surprisingly, there was a time when phase-field modeling was regarded as 'a toy' that was interestingly capable of simulating realistically complicated micro-morphologies. It was however soon more or less overcome by the later more rigorous formulations of phase-field models which were consistent with both thermodynamic principles and kinetic laws and at the same times brought to account more and more physical values. For instance, the formulations of Chen [89] and Wang [90], which originated from the microscopic theory of Khachaturyan, considered order parameter as a physical indicator of crystal symmetry and sought to minimize the total free energies of the system whose functional was described by the Ginzburg and Landau formula. Similar formulations were derived by Miyazaki [91, 92] and Onuki and Nishimori [93] to describe spinodal decomposition in materials with a composition-dependent molar volume, and by Finel and Le Bouar to describe the interaction of stress, strain and dislocations with precipitate growth and structural phase transitions [94, 95, 96]. A different type of formulation originated from the idea of Langer [97] which treated the phase-field variable as an index to differentiate one phase from the other. Al-

though this idea was somewhat pragmatic, the general formulation of the model could still be made thermodynamically and kinetically consistent and could be extended in a straightforward way to account for various physical values, a general advantage of phase-field modeling; especially since it allows coupling with the CALPHAD method which in turn allows the estimation of reliable thermodynamic driving forces for microstructural growth. Remarkable contributors of the Langer-type formulation included Kim and Kim [98], Karma and Plapp [99, 100, 101, 102, 103], and Steinbach et al. [104, 105].

Nowadays, the phase-field method is a very popular method for simulating dynamical processes at the mesoscale level. Its applications range from solidification [106], solid-state phase transformations [107], and grain growth [108], to dislocation dynamics [109, 94, 110], crack propagation [111, 112], electromigration [113], solid-state sintering [114, 115, 116] and vesicle membranes in biological applications [117, 118]. For this, it is recognized as an important methodological component of ICME for studying the evolution of microstructure, the key to materials science and engineering. Let us now look at the two aforementioned seeds of the phase-field method.

2.3.2 The phase-field concept

What is the fundamental concept of phase-field modeling? To be frank, the *diffuse character* of *phase-field variables* at the interface. This concept and its significance to the phase-field method can be well understood by addressing the following three constituent questions: (1) "What are the *phase-field variables*?", (2) "What is the *diffuse character* of the phase-field variables?", and (3) "Why is the diffuse character key to the phase-field modeling?". Let us now answer these questions one after another:

First, what are the phase-field variables? Within the context of the phase-field method, the evolution of a microstructure is described by the evolutions of the phase-field variables. These variables are state variables that are continuous functions of time and space. Together, they identify the state of a microstructural system, i.e. the microstructural morphology (and many more). Qualitatively, the phase-field variables can be related to the physical properties of materials such as crystal structure, orientation, or composition; they can also be artificial indices to simply differentiate bulk materials from each other. Quantitatively, the phase-field variables can be either conserved, e.g. compositions, or non-conserved, e.g. artificial indices.

What is then the diffuse character of the phase-field variables? As continuous functions in time and space, the phase-field variables have nearly constant values within a phase (or bulk) region while at the interface between two phases they vary gradually from their values in one phase to their values in the other phase across the interface with a finite thickness. The smooth transitions of the phase-field variables across the interface with respect to both space and time essentially characterizes the diffuse character of the phase-field variables at the interface, and hence the diffuse-interface character of the phase-field method for which, and in relative to the conventional sharp-interface description, the method is regarded as the diffuse-interface description. Fig. 2.2 demonstrates the interface within the diffuse-interface description in relative to that within the conventional sharp-interface description.

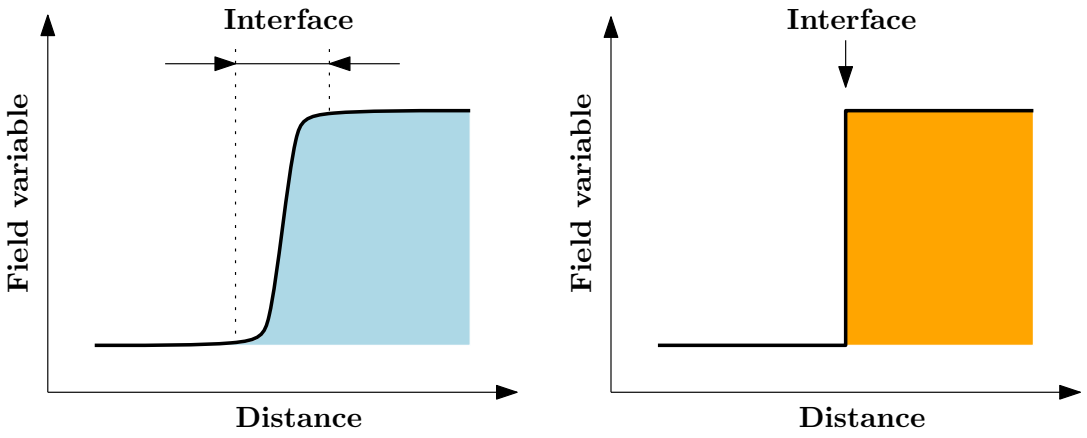

(a) Diffuse interface **(b) Sharp interface**

Figure 2.2: Diffusive interface vs sharp interface. Here, it is noted that in the diffuse-interface description properties evolve continuously between their equilibrium values in the neighboring phases while in the sharp-interface description properties are discontinuous at the interface.

Now, why is the diffuse character of the phase-field variables key to the phase-field method? The beauty of the diffuse-interface description is that the evolution of a microstructure, or in other words the position of the interfaces between grains as a function of time, is implicitly given by the evolution of the phase-field variables. Thanks to this, there is no need to explicitly track the position of the interfaces between phases during a microstructural evolution, and hence the simulations of complex morphological evolutions, typically observed in real alloy systems, can be made possible in an efficient and fairly physical manner without making a priori assumption on the shapes of the grains. Here, it is noted that the explicit tracking of the interface is attributed to the conventional sharp-interface description. Within this description, the position of the interfaces is explicitly tracked by means of mathematical equations which describe the physical mechanisms occurring at the interfaces (see for example [119, 120] or [121]). From the mathematical point of view, formulat-

ing these equations is extremely difficult especially for complex grain morphologies, which are commonly encountered in real alloy systems (and this is why Kobayashi made the stunning remark in 1993 with his 'different' model). Therefore, the sharp-interface description is mostly restricted to one-dimensional systems or simplified grain morphologies. On this side of the sharp-interface approach, the phase-field modeling really offers an appealing alternative with its diffusive-interface concept.

2.3.3 Formulation of the phase-field concept

From the above diffuse-interface concept, it was generally known that a phase-field model describes the evolution of a microstructure by means of the evolutions of the phase-field variables that are continuous functions in space and time. From the mathematical point of view, the statement: '*the evolutions of the phase-field variables that are continuous functions in space and time*' indicates a system of partial differential equations (each for one phase-field variable) that takes space and time as independent variables. These partial differential equations should contain the second-order gradient terms of the phase-field variables to take into account the diffuse character of the interface, i.e. the phase-field concept. More importantly, they have to be thermodynamically consistent so that the formulation of the phase-field model is rigorous. In other words, these partial differential equations have to minimize the total free energy of the system in order to evolve the phase-field variables. These considerations essentially lead to two important ingredients for the formulation of the phase-field concept: (1) an energy functional, i.e. energy as a function of the phase-field variables which in turn are functions of space and time, which contains the second-order gradients and (2) the variational principles applied on this energy functional, a common practice in the minimization of energy in physical modeling.

2.3.3.1 Thermodynamic energy functional

The energy functional that is commonly used among the scientists who practice phase-field modeling is the Cahn-Hilliard [84] energy functional. For a simple case of constant temperature and molar volume and no elastic, magnetic, or electric field, this energy functional reads:

$$F(x_B, \eta_k) = \int_V \left[f_0(x_B, \eta_k) + \frac{\epsilon}{2}(\vec{\bigtriangledown} x_B)^2 + \sum_k \frac{\kappa_k}{2}(\vec{\bigtriangledown} \eta_k)^2 \right] d\vec{r} \tag{2.60}$$

where, $f_0(x_B, \eta_k)$ denotes the classical free-energy density of a homogeneous system where all state variables, in this case the phase-field variables, are constant throughout the system. The required gradient terms are of course responsible for the diffuse character of the interfaces. The ϵ and κ coefficient are called gradient energy coefficients. They are related to the interfacial energy and thickness and always positive, so that gradients in the phase-field variables are energetically unfavorable and give rise to surface tension.

Here, it is noted that the phase-field variable η_k in Eq. 2.60 can either have physical meaning or be artificial. Depending on which one of these two one chooses to practice, it leads to a distinct description of the homogeneous free-energy density, f_0, hence the existence of two different types of phase-field models that have been developed independently by the two communities: the phase-field school of Khachaturyan and the phase-field school of Langer.

In the phase-field school of Khachaturyan, the phase-field variable is called order parameter, η, and is mostly used for representing the crystal symmetry of a microstructure. For this, the phase-field models within this school are usually applied to solid-state phase transformations (see [107] for an overview) that involve a symmetry reduction, for instance, the precipitation of an ordered intermetallic phase from

a disordered matrix [122, 123] or martensitic transformation [124, 125]. It is also applied to ferroelectric [126, 127] and magnetic domain evolution [128] and can account for the influence of elastic strain energy on the evolution of the microstructure.

Within this school, the homogeneous free-energy density, f_0, is described by the Landau polynomial which is a function of order parameters and composition and whose chosen order, which indicates the total minima of the polynomial, usually matches the number of crystal symmetries available in the system. For instance, in the case of the cubic to tetragonal phase transformation in which a cubic phase can transform to three different tetragonal (with longitude along x, y, and z orientations) and each tetragonal has two variants depending on which sublattice is occupied, the Landau free energy as a function of three order parameters must have six minima with equal depth (since the tetragonal phases have the same probability to form from the cubic parent phase). The form of the Landau polynomial for this type of transformation can be given by:

$$f_0(x_B, \eta) = \frac{1}{2}A(x_B)\sum_{k=1}^{3}\eta_i^2 - \frac{1}{4}B(x_B)\sum_{k=1}^{3}\eta_i^4 + \frac{1}{6}C(x_B)\left(\sum_{k=1}^{3}\eta_i^2\right)^3 \tag{2.61}$$

when A, B, and C are constant, the above polynomial reduces to the model of Wang and Khachaturyan [124]. Another example is the precipitation of an ordered intermetallic in a disordered matrix [129] in which the Landau polynomial reads:

$$f_0(x_B, \eta) = \frac{1}{2}A(x'_B - x_B)^2 + \frac{1}{2}B(x''_B - x_B)\eta^2 - \frac{1}{4}C\eta^4 + \frac{1}{6}D\eta^6 \tag{2.62}$$

where A, B, C, and D are positive phenomenological constants with a dimension of energy and x'_B and x''_B are constants with a dimension of composition.

Here, it is noted that even though the Landau polynomial offers the capability (its minina) to differentiate among the phases (with different crystal symmetries), the energetic value and eventually the thermodynamic driving force resulting from this polynomial are not essentially the values of the real alloy system. Indeed, for many times, the above polynomial coefficients, i.e. A, B, C, etc., are chosen so that the phase-field simulation can phenomenologically produce the microstructural morphology of interest. This could be seen as a limitation of this type of phase-field formulation.

In the phase-field school of Langer, a phenomenological phase-field variable, ϕ, is used purely to differentiate the reacting phases among each other. The model is mainly applied to solidification, e.g. the growth of dendrite, the micro-segregation of solute elements, and the coupled growth in eutectic solidification (see [106, 130] for an overview). Within this school, the homogeneous free-energy density, f_0, consists of an interpolation function, $h(x_B, \phi, T)$, and a double-well-type function, $g(\phi)$:

$$f_0(x_B, \phi, T) = h(x_B, \phi, T) + g(\phi) \tag{2.63}$$

The commonly-used double-well-type functions, $g(\phi)$, are the double-obstacle potential or the double-well potential. In case of the double-well potential, $g(\phi)$ is written as:

$$g(\phi) = w\phi^2(1-\phi)^2 \tag{2.64}$$

which has one minimum at 0 and another minimum at 1. Here, w represents the depth of the energy well; it can be either a constant [98] or linearly dependent on the molar fraction: $w = (1 - x_B)w_\alpha + x_B w_\beta$, where w_α and w_β denotes the energy depths in the α and β phases, respectively.

The interpolation function $h(x_B, \phi, T)$ combines the free energy expressions of the coexisting phases α and β, namely $f_\alpha(x_B, T)$ and $f_\beta(x_B, T)$, into one free energy expression using a weight function $p(\phi)$ as follows:

$$h(x_B, \phi, T) = (1 - p(\phi))f_\alpha(x_B, T) + p(\phi)f_\beta(x_B, T) \tag{2.65}$$

where, it is assumed that ϕ equals 0 in the α phase and 1 in the β phase.

Note here that the energy $f_\alpha(x_B, T)$ and $f_\beta(x_B, T)$ can stem from the CALPHAD method which is a widely-accepted approach for estimating the thermodynamic properties of multi-component alloys. Compared to the above Landau polynomial, the CALPHAD energy is intuitively more realistic, and therefore an advantage of the Langer-type formulation. Another advantage of the Langer-type formulation is that its extension to the case of multi-phase multi-component is considerably easier than in the Khachaturyan-type formulation.

2.3.3.2 Minimization of free energy

With the energy functional taken either from the Khachaturyan school or the Langer school, the evolution equations of the phase-field variables (state variables), which minimize the total free energy of the system, can be achieved by applying the variational principles on the energy functional. This is particularly done by taking the partial derivatives of the energy functional with respect to the phase-field variables (state variables). To demonstrate this, I will make use of Steinbach's recent model [36], which is known as the phase-field model with finite interface dissipation and belongs to the Langer's school. This is also the model that I will implement in the following major section to investigate the thermodynamic origin of the discontinuous monotectoid decomposition, including the discontinuous precipitation and discontinuous coarsening, as well as the microstructural evolution of the discontinu-

ous precipitation.

To account for non-equilibrium transformations which may exhibit a diffusion-potential jump across the interface, Steinbach *et al.* [36] recently developed a new phase-field model, called the phase-field model with finite interface dissipation, or in short the interface dissipation model. The novelty of this model relative to conventional phase-field models is that the rate at which the diffusion-potential jump across the interface dissipates can be controlled by a characteristic constant, called interface permeability for redistribution fluxes or inverse interface resistivity, which associates with a kinetic equation that links the two separate concentration fields in each phase at the interface together. Note that in a conventional model with equal diffusion potentials the rate at which the diffusion-potential jump across the interface dissipates is infinite in principle since the two concentration fields at the interface are linked by the equilibrium partitioning condition which, by its nature, enforces the instant convergence to the equilibrium values for each concentration field instead of allowing a gradual diffusion-based change as in a kinetic equation. The derivation of this model for the simple case of two-phase binary system starts with the definition of the Cahn-Hilliard energy functional:

$$F = \int_V \frac{4\sigma_{\alpha\beta}}{\eta}\left(-\frac{\eta^2}{\pi^2}\bigtriangledown\phi_\alpha\cdot\bigtriangledown\phi_\beta+\phi_\alpha\phi_\beta\right)+\phi_\alpha f_\alpha(c_\alpha)+\phi_\beta f_\beta(c_\beta)+\lambda[c-(\phi_\alpha c_\alpha+\phi_\beta c_\beta)] \tag{2.66}$$

where, c_α, c_β, ϕ_α, and ϕ_β are the phase-field variables, or state variables, whose evolution equations are to be defined in the following; here, c_α and c_β are the phase concentrations of the α and the β phases, respectively; ϕ_α and ϕ_β are the phase fractions of the α and the β phases respectively and are constrained to the following relationship: $\phi_\alpha + \phi_\beta = 1$. η is the interface width, $\sigma_{\alpha\beta}$ is the interfacial energy,

and the Lagrange multiplier, λ, is associated with the solute-conservation constraint: $c = \phi_\alpha c_\alpha + \phi_\beta c_\beta$. Note here that the energy coefficient κ in the original Cahn-Hilliard energy functional, Eq. 2.60, is zero; the interpolation function is $h = \phi_\alpha f_\alpha(c_\alpha) + \phi_\beta f_\beta(c_\beta)$, where the weight function $p = \phi_\beta$; and, the double-obstacle potential, $g = \phi_\alpha \phi_\beta$, is used instead of the double-well potential.

The evolutions of the phase concentrations, namely c_α and c_β, are derived from the variational principle by taking the partial derivatives of the energy functional, F, with respect to each phase concentration as follows:

$$\dot{c}_\alpha = -P_\alpha \frac{\delta}{\delta c_\alpha} F = -P_\alpha \left[\phi_\alpha \frac{\partial f_\alpha}{\partial c_\alpha} - \phi_\alpha \lambda \right] \tag{2.67}$$

$$\dot{c}_\beta = -P_\beta \frac{\delta}{\delta c_\beta} F = -P_\beta \left[\phi_\beta \frac{\partial f_\beta}{\partial c_\beta} - \phi_\beta \lambda \right] \tag{2.68}$$

with P_α and P_β are the kinetic coefficients indicating the rate of change of the phase concentrations and are defined according to the following relationship: $\phi_\alpha P_\alpha = \phi_\beta P_\beta = P$, where P is the interface permeability which, from the atomistic point of view, is expressed as:

$$P = \frac{8M}{a\eta}, \tag{2.69}$$

in which, M is atomic mobility; a is lattice parameter. For a detailed discussion on the physical meaning of P, the original work of Steinbach *et al.* [36] is recommended. Now, with $P_\alpha = \frac{P}{\phi_\alpha}$ and $P_\beta = \frac{P}{\phi_\beta}$, the above equations turn into:

$$\phi_\alpha \dot{c}_\alpha = -P \left[\phi_\alpha \frac{\partial f_\alpha}{\partial c_\alpha} - \phi_\alpha \lambda \right] \tag{2.70}$$

$$\phi_\beta \dot{c_\beta} = -P\left[\phi_\beta \frac{\partial f_\beta}{\partial c_\beta} - \phi_\beta \lambda\right] \tag{2.71}$$

Next, we substitute $(\dot{\phi_\alpha c_\alpha}) = \dot{\phi}_\alpha c_\alpha + \phi_\alpha \dot{c}_\alpha$ and $(\dot{\phi_\beta c_\beta}) = \dot{\phi}_\beta c_\beta + \phi_\beta \dot{c}_\beta$ into Eq. 2.70 and Eq. 2.71, respectively:

$$(\dot{\phi_\alpha c_\alpha}) = -P\left[\phi_\alpha \frac{\partial f_\alpha}{\partial c_\alpha} - \phi_\alpha \lambda\right] + \dot{\phi}_\alpha c_\alpha \tag{2.72}$$

$$(\dot{\phi_\beta c_\beta}) = -P\left[\phi_\beta \frac{\partial f_\beta}{\partial c_\beta} - \phi_\beta \lambda\right] + \dot{\phi}_\beta c_\beta \tag{2.73}$$

Summing up the above two equations, we obtain:

$$\begin{aligned} \dot{c} &= (\dot{\phi_\alpha c_\alpha}) + (\dot{\phi_\beta c_\beta}) \\ &= -P\left[\phi_\alpha \frac{\partial f_\alpha}{\partial c_\alpha} + \phi_\beta \frac{\partial f_\beta}{\partial c_\beta} - \lambda\right] + \dot{\phi}_\alpha c_\alpha + \dot{\phi}_\beta c_\beta \end{aligned} \tag{2.74}$$

We now divide the space into distinct reference volumes RV and make the assumption that internal processes inside a reference volume and exchange of atoms between adjacent reference volumes are independent and can be superimposed. In an isolated RV, since the overall concentration is independent of time, $\dot{c} = 0$. This leads to the solution of the above equation for the Lagrange multiplier λ as follows:

$$\lambda = \phi_\alpha \frac{\partial f_\alpha}{\partial c_\alpha} + \phi_\beta \frac{\partial f_\beta}{\partial c_\beta} - \frac{\dot{\phi}_\alpha c_\alpha + \dot{\phi}_\beta c_\beta}{P} \tag{2.75}$$

Substituting λ in Eq. 2.70 and Eq. 2.71, we obtain the evolution equations for each phase inside the reference volume:

$$\phi_\alpha \dot{c}_\alpha = P\phi_\alpha\phi_\beta \left(\frac{\partial f_\beta}{\partial c_\beta} - \frac{\partial f_\alpha}{\partial c_\alpha} \right) + \phi_\alpha \dot{\phi}_\alpha (c_\beta - c_\alpha) \tag{2.76}$$

$$\phi_\beta \dot{c}_\beta = P\phi_\alpha\phi_\beta \left(\frac{\partial f_\alpha}{\partial c_\alpha} - \frac{\partial f_\beta}{\partial c_\beta} \right) + \phi_\beta \dot{\phi}_\beta (c_\alpha - c_\beta) \tag{2.77}$$

The first part in Eq. 2.76 and Eq. 2.76 describes the flux of solute between the phases due to a difference in the diffusion potential and the second term represents the change of the phase concentrations due to an imposed phase change. Now, we superimpose the internal processes inside RV and external fluxes from adjacent RVs, leading to the final evolution equations for the state variables, c_α and c_β, as follows:

$$\phi_\alpha \dot{c}_\alpha = \vec{\nabla}(\phi_\alpha D_\alpha \vec{\nabla} c_\alpha) + P\phi_\alpha\phi_\beta \left(\frac{\partial f_\beta}{\partial c_\beta} - \frac{\partial f_\alpha}{\partial c_\alpha} \right) + \phi_\alpha \dot{\phi}_\alpha (c_\beta - c_\alpha) \tag{2.78}$$

$$\phi_\beta \dot{c}_\beta = \vec{\nabla}(\phi_\beta D_\beta \vec{\nabla} c_\beta) + P\phi_\alpha\phi_\beta \left(\frac{\partial f_\alpha}{\partial c_\alpha} - \frac{\partial f_\beta}{\partial c_\beta} \right) + \phi_\beta \dot{\phi}_\beta (c_\alpha - c_\beta) \tag{2.79}$$

where, D_α and D_β are the chemical diffusivities in the α and β phases, respectively.

The evolution equation of the phase fraction, ϕ_α, is derived by taking the partial derivatives of the Cahn-Hilliard energy functional with respect to this phase-field variable:

$$\begin{aligned} \dot{\phi}_\alpha &= -\frac{\pi^2}{8\eta}\mu_{\alpha\beta}\left\{ \frac{\partial F}{\partial \phi_\alpha} - \partial\phi_\beta \right\} \\ &= \mu_{\alpha\beta}\left\{ \sigma_{\alpha\beta}\left[\nabla^2 \phi_\alpha + \frac{\pi^2}{\eta^2}\left(\phi_\alpha - \frac{1}{2} \right) \right] - \frac{\pi^2}{8\eta} \triangle \tilde{g}_{\alpha\beta} \right\} \end{aligned} \tag{2.80}$$

(note that for the last equation we take into account the relationship: $\dot{\phi}_\alpha = -\dot{\phi}_{beta}$), where $\mu_{\alpha\beta}$ is the interfacial mobility, and $\triangle\tilde{g}_{\alpha\beta}$ is the generalized chemical driving force, which reads:

$$\triangle\tilde{g}_{\alpha\beta} = f_\alpha - f_\beta - \lambda(c_\alpha - c_\beta) \tag{2.81}$$

in which we make use of the fact that $c-(\phi_\alpha c_\alpha + \phi_\beta c_\beta)$ equals zero and that there is no contribution proportional to $\frac{\partial\lambda}{\partial\phi_\alpha}$ arises. With the Lagrange multiplier, λ, known from the above derivation, the last equation becomes:

$$\triangle\tilde{g}_{\alpha\beta} = f_\alpha - f_\beta - \left(\phi_\alpha\tilde{\mu}_\alpha + \phi_\beta\tilde{\mu}_\beta - \frac{\dot{\phi}_\alpha(c_\alpha - c_\beta)}{P}\right) \tag{2.82}$$

where, $\tilde{\mu}_\alpha$ and $\tilde{\mu}_\beta$ are the diffusion potentials of the α and β phases, respectively. Rearrangement of the terms proportional to $\dot{\phi}_\alpha$ leads the final evolution equation for the phase fraction, ϕ_α:

$$\dot{\phi_\alpha} = K\left\{\sigma_{\alpha\beta}\left[\bigtriangledown^2\phi_\alpha + \frac{\pi^2}{\eta^2}\left(\phi_\alpha - \frac{1}{2}\right)\right] - \frac{\pi^2}{8\eta}\triangle g_{\alpha\beta}^{phi}\right\}, \tag{2.83}$$

where, K is the kinetic coefficient that expresses the influence of finite diffusion and redistribution at the interface:

$$K = \frac{8P\eta\mu_{\alpha\beta}}{8P\eta + \mu_{\alpha\beta}\pi^2(c_\alpha - c_\beta)^2} \tag{2.84}$$

And, $\triangle g_{\alpha\beta}^{phi}$ is the chemical driving force:

$$\triangle g_{\alpha\beta}^{phi} = f_\alpha - f_\beta + (\phi_\alpha\tilde{\mu}_\alpha + \phi_\beta\tilde{\mu}_\beta)(c_\beta - c_\alpha). \tag{2.85}$$

In practical simulations, it is of advantage to introduce a weighting function which

couples the interface and thermodynamic contributions in the phase-field equation to concentrate the thermodynamic driving force in the center of the interface (see [36]). This leads to the following approximation:

$$\dot{\phi_\alpha} = K\left\{\sigma_{\alpha\beta}\left[\bigtriangledown^2\phi_\alpha + \frac{\pi^2}{\eta^2}\left(\phi_\alpha - \frac{1}{2}\right)\right] - \frac{\pi}{\eta}\sqrt{\phi_\alpha(1-\phi_\alpha)}\bigtriangleup g_{\alpha\beta}^{phi}\right\}, \tag{2.86}$$

Since ϕ_β can be calculated from ϕ_α using the relationship: $\phi_\beta = 1 - \phi_\alpha$ there is no need to derive the evolution equation for this state variable. The phase evolution Eq. 2.86 together with the concentration evolution Eq. 2.78 and Eq. 2.79 will be used in the next major section to investigate the non-equilibrium phase transformations and microstructural growth happening in the discontinuous monotectoid decomposition of the uranium-niobium system.

3. APPLICATION TO URANIUM-NIOBIUM*

In this major section, the integrated computational framework is carried out to investigate the fundamental thermodynamics and kinetics of uranium-niobium as well as their roles on the origin of the system's discontinuous reaction. This computational study is carried out for the purpose of reassuring the advantage of computational materials science in facilitating the design processes of materials in general and of nuclear materials in specific. It is demonstrated in our philosophy upon studying this material: Although experiments are important pronouncements of materials' natures, they are usually cost prohibitive. This is especially critical for nuclear-related materials, and as such experimental studies on the DP and DC reactions are scarce and understanding of their fundamentals is limited. This is where simulation and modeling come in handy. The developments of basic sciences and the tremendous growth of computational technology have been continuously powering computational aided materials design, allowing simulations to go hand-in-hand with experiments for a higher efficiency. From time to time, it has been proven that the inclusion of theoretical approaches can shed light on the interesting natures of materials. And, it is hoped that through theoretical assessing of the fundamental thermodynamics and kinetics of uranium-niobium system we may gain a better understanding, or perhaps insight, into the nature of its discontinuous reactions and to other existing metastable microstructures in other alloy systems. In the following section we present details on the hierarchical computational methodology and its results.

*Reprinted with permission from "Multiscale Modeling of Discontinuous Precipitation in U-Nb" by Thien Duong, Raymundo Arróyave, 2015. *Proceedings of the TMS Middle East - Mediterranean Materials Congress on Energy and Infrastructure Systems (MEMA 2015)*, pages 481–490, Copyright 2015 by John Wiley & Sons

3.1 First-principles calculations of γ's formation energies

In this section, first-principles calculations are carried out to estimate ground-state formation energies of the bcc phase, γ. In particular, different density-functional theories including Korringa-Kohn-Rostoker, exact muffin-tin orbital, and projector augmented wave methods are used. The resulting *ab initio* energetic data will be imposed as an first-principles constraint in later CALPHAD thermodynamic assessment to improve the consistency and reliability of the assessment.

3.1.1 Computational details

For first-principles investigations in the present work, we utilize two different Green's function approaches, namely Korringa-Kohn-Rostoker (KKR) multiple scattering formalism and exact muffin-tin orbital (EMTO) method. The self-consistent calculations are performed within the scalar-relativistic regime for a basis set of *spdf* valence orbitals. The core states are recalculated at every ionic step according to the soft-core approximation. Generalized gradient approximation (GGA) is adopted for the exchange-correlation functional [59]. The integration over the Brillouin zone is done using a $31 \times 31 \times 31$ grid of k-points determined according to the Monkhorst-Pack scheme [131]. Integration of Greens function is carried out over a complex energy contour with a 2.6 Ry diameter using a Gaussian integration technique with 40 points on a semi-circle enclosing the occupied states.

The substitutional disorder of the alloys is treated by using the coherent potential approximation (CPA) [54]. The applicability of CPA is checked in supercell calculations realized by the locally self-consistent Greens function (LSGF) method within the EMTO formalism [132, 133]. In particular, such calculations are used to determine the contributions from the screened Coulomb interactions to the one-electron potential V_i^{scr} of alloy components i, and the total energy E_{scr}, within the single-site

DFT formalism:

$$V_i^{scr} = -\alpha \frac{e^2 q_i}{S}; \text{ and, } E_{scr} = \frac{\beta}{2} \sum_i c_i q_i V_i^{scr}. \tag{3.1}$$

where, e is the electron charge; S is the Wigner-Seitz radius; q_i is average net charge of the atomic sphere; and, c_i is the concentration for the i^{th} alloy component. The screening constants α and β are found to be 0.725 and 1.088, respectively.

In addition to the Green's function approaches, we also use a different DFT approach for the self-consistent energetic calculations to strengthen our first-principles investigation. Namely, the full potential projector augmented wave (PAW) method [48, 134] as implemented in the Vienna *ab initio* simulation package (VASP) [135, 136, 137] is considered. Here, the disordered structures of U - 12.5 *at.*% Nb, U - 25 *at.*% Nb, U - 50 *at.*% Nb, U - 72.5 *at.*% Nb and U - 87.5 *at.*% Nb are modeled by the special quasirandom structure (SQS) technique [49] generated by Monte-Carlo algorithm using 64-atom supercells. A Monkhorst-Pack mesh of $7 \times 7 \times 7$ points (including Γ) and cut-off energy of 478 eV are considered for the integration over the Brillouin zone. It is believed that the used cell size, number of k-points and cut-off energy are reasonably chosen for good accuracy of self-consistent energetic calculations. Indeed, a verification calculation, carried out for the case of U - 50 *at.*% Nb using a 128-atom SQS supercell with a $9 \times 9 \times 9$ grid of k-points and a cut-off energy of 550 eV, demonstrates a small energetic difference (in the order of $\frac{1}{10}$ $meV/atom$) w.r.t to the previous calculation. For better results, the value of 10^{-7} eV is chosen for the convergence criterion. The GGA is again used to approximate for the exchange-correlation interactions.

3.1.2 Results and discussions

To verify our first-principles approaches, concentration-dependent lattice parameters of γ were calculated and compared with experimental data [2]. Results, shown in Fig. 3.1, indicates that the proposed Green's function techniques reasonably reproduce the structural characteristics of the materials (with maximum error less than 3% after taking into account the correction from thermal expansion using the linear coefficients of thermal expansion of $20 \times 10^{-6} K^{-1}$ and $7.88 \times 10^{-6} K^{-1}$ around $1000^0 C$ for pure γ uranium and niobium, respectively [138]. Note that for these sufficient results we only treat the uranium's 5f-electrons as normal particles. It has been shown in the recent work of Söderlind *et al.* [139] that uranium when alloyed with metals possesses weekly correlated electrons which can be adequately described within the context of DFT-GGA.

For reducing computational expense, PAW were only considered for the static calculations of ground-state formation energies with lattice constants interpolated from the EMTO's verified results. Within the framework of PAW and the Green's function approaches, isostructural formation energies are evaluated according to the following formula:

$$\Delta H^{\phi} = {}^0E^{\phi}_{U_{1-x}Nb_x} - (1-x){}^0E^{\phi}_{\gamma U} - x{}^0E^{\phi}_{\gamma Nb} \tag{3.2}$$

where, ${}^0E^{\phi}$ are the ground-state energies of phase ϕ and x is atomic fraction of Nb.

The calculated formation energies of γ are shown in Fig. 3.2. It can be seen from the figure that the first-principles results are generally in good agreement with each other. Discrepancy between PAW and the Green's function methods, which is of an acceptable order of $\sim 1.0\ kJ/mol$, is perhaps due to the differences between CPA and SQS approximations. Since the PAW calculations do not clearly suggest

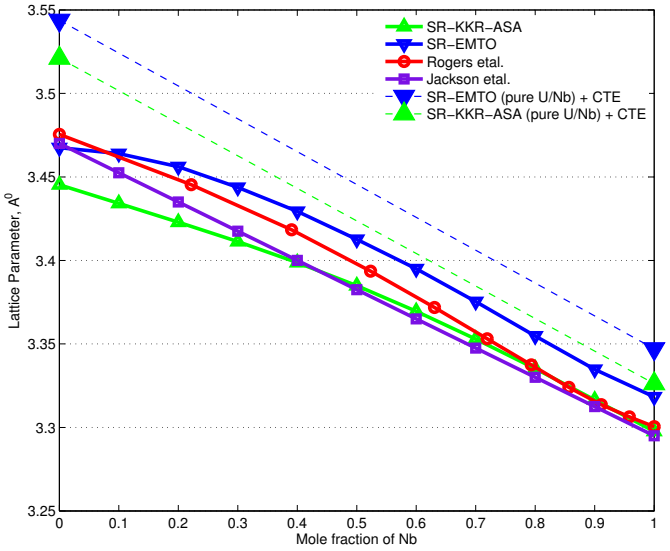

Figure 3.1: Calculated composition-dependent lattice parameters of γ-bcc at 0 K as compared to experimental data from Rogers *et al.* [2] and Jackson *et al.* [3]. Note that Rogers *et al.* measured lattice parameters of uranium-niobium alloys after they were quenched from 1100^0C [2].

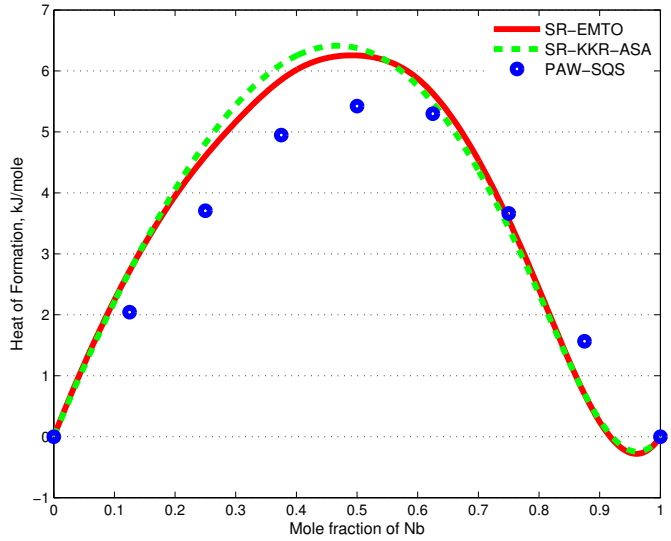

Figure 3.2: Calculated ground-state heats of formation of γ-bcc using SR-EMTO, SR-KKR-ASA and PAW-SQS.

an exothermic behavior within the Nb-rich region as inferred in the system's phase diagram [39], it is believed that CPA is better than SQS in this case, and the energetic data resulting from the Green's function calculations are more reliable.

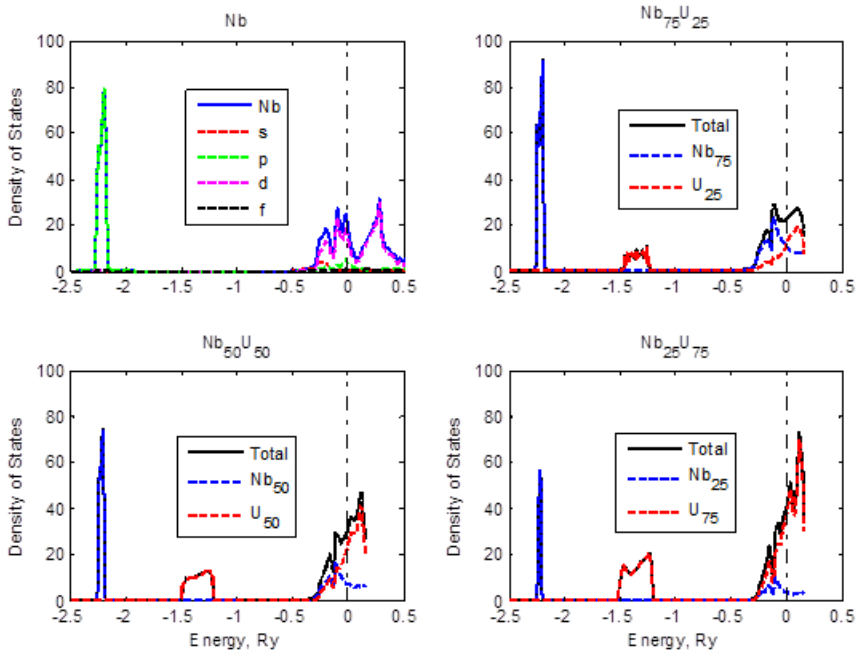

Figure 3.3: Calculated density of states of pure Nb, $U_{25}Nb_{75}$, $U_{50}Nb_{50}$, and $U_{75}Nb_{25}$.

To better understand the ground-state thermodynamic properties of the bcc uranium-niobium alloys, electronic densities of states were investigated at different compositions within the framework of Korringa-Kohn-Rostokers (KKR) multiple scattering formalism. The results are shown in Fig. 3.3. Here, the system is considered to be metallic taking into account the delocalized f-electrons and p-semi-core states as valence. Prior literature has shown that this treatment is reasonable for ab initio investigations of metallic fuels [41, 140, 141]. In the figure, it can be seen that uranium acts as the system's electron delocalizer as it promotes low-energy elec-

trons to higher energy states. This refines niobium's p-semi-core states to a narrower band and more importantly redefines niobium's electronic structure near the Fermi surface, which can be related to the system's solubility.

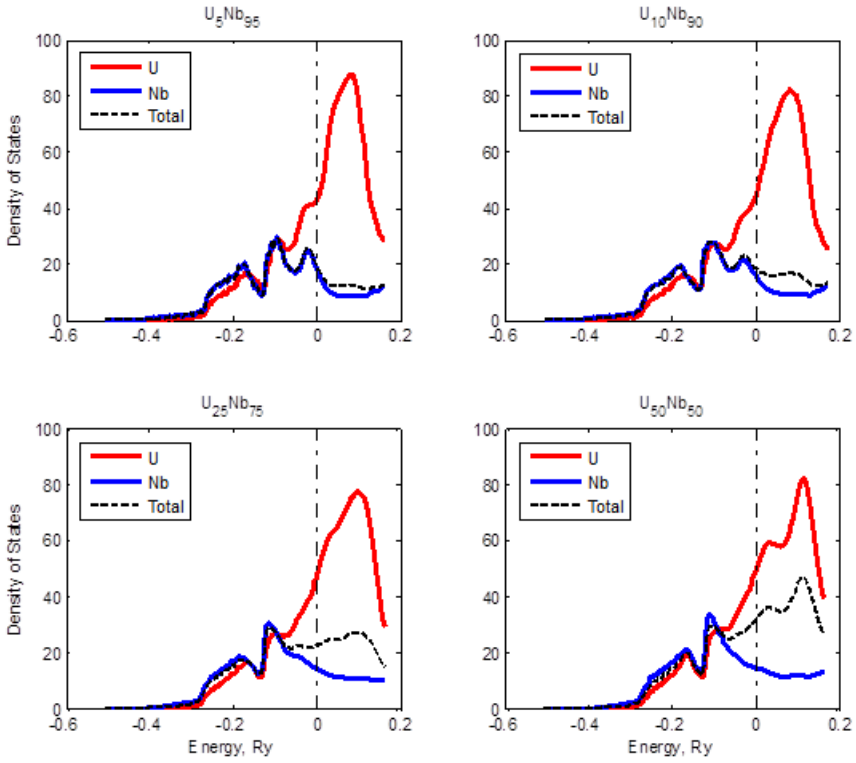

Figure 3.4: Calculated density of states of U_5Nb_{95}, $U_{10}Nb_{90}$, $U_{25}Nb_{75}$, and $U_{50}Nb_{50}$ near the Fermi surface.

A closer view of niobium's and uranium's (un-weighted) electronic densities of states around the Fermi surface can be found in Fig. 3.4. As can be seen from this figure, uranium's and niobium's high-energy electrons exhibit a hybridization which can be attributed to the metallic bond normally characterizing metallic alloys. From the electronic point of view, this bond could be responsible for the solubility

of uranium in niobium and vice versa as follows. For the bcc niobium-rich alloys, the hybridization occurs approximately on three peaks of niobium's d-orbital. When more uranium is alloyed, the third peak of hybridization is smeared away, which can perhaps be explained by a stronger repulsion between the denser (floating) uranium's f-electrons and niobium's d-electrons which tends to push some of the d-electrons inwards. This smearing leads to a weaker metallic bond between the two metals, resulting in a lower solubility for high-uranium alloys. One however may argue that the electrons which are pushed deeper into niobium's valence band can fortify the first two hybridization peaks, which are energetically stronger than the third; and hence, the bond will not necessarily be weakened. This is indeed the complicated reality. Apparently, there are two opposite trends competing to decide the solubility of the material and the factor deciding the winner is the amount of d-electrons being pushed back. In the case of uranium-niobium alloys, from Fig. 3.4 we observe relatively small changes of the first two peaks compared to the complete disappearance of the third one, occurring from 5%at alloyed uranium to 50%at alloyed uranium. Also, there is a possibility that the third peak of uranium's density of states is a more pronounced spike, but is screened off within the mean field coherent potential approximation; this spike, if it existed, would position the electron densities of uranium, within niobium-rich alloys, well at a "metastable" state, establishing the stability of these alloys. From the experimental viewpoint, Koike et al. [39] indeed suggested that the bcc uranium-niobium solid solutions exhibit exothermic (phase-mixing) phenomenon in compositions below 20%at-uranium and endothermic (phase-separating) behavior in higher %at-uranium compositions at low temperatures. This was also verified by the experiments of Vambersky et al. [4] which measured the excess enthalpy and entropy of mixing at 1100 K.

The solubility of uranium-niobium could be better understood relative to those

of uranium-molybdenum and uranium-zirconium. Fig. 3.5 compares the Fermi density of states of uranium-niobium with that of uranium-molybdenum and uranium-zirconium. Topologically, we see that the 90%at-uranium alloys are similar in their electron densities, noting that the partial density of state of uranium remains almost unchanged in all three alloys. The main difference is the magnitude of the first two hybridization peaks, which are largest in uranium-molybdenum. This is common sense since molybdenum has one electron than niobium and hence the portion of d-electrons being pushed inwards should be larger. In other words, the strengthening of metallic bond due to the hybridization of the first two peaks is stronger than the smearing of the third peak in uranium-molybdenum system, resulting in the system favoring solubility at the uranium-rich side. For the same reason, zirconium however has one electron less than niobium so its metallic fuel is even less stable than that of niobium at high uranium compositions. From Fig. 3.5, one can also study the relative stability/solubility of these alloys at low uranium concentrations. In particular, it can be seen that zirconium-10%at uranium is less stable than niobium-10%at uranium with two hybridization peaks as opposed to three. The smearing of hybridization peaks also occurs within the range of compositions although on the uranium atoms. Again, for the niobium-uranium system the smearing is relatively small compared to the strengthening coming from the additional third peak, insisting on high solubility of the system on this side of the composition. For molybdenum-uranium, the smearing however is strong resulting in the unstable molybdenum-rich actinide alloys.

Before moving on, it is noted that for other solid states in the uranium-niobium system, low symmetrical structures appear to be obstacles in the density-functional estimations of their formation energies, i.e., computational costs for self-consistent energetic calculations of those structures are impractically expensive. This is es-

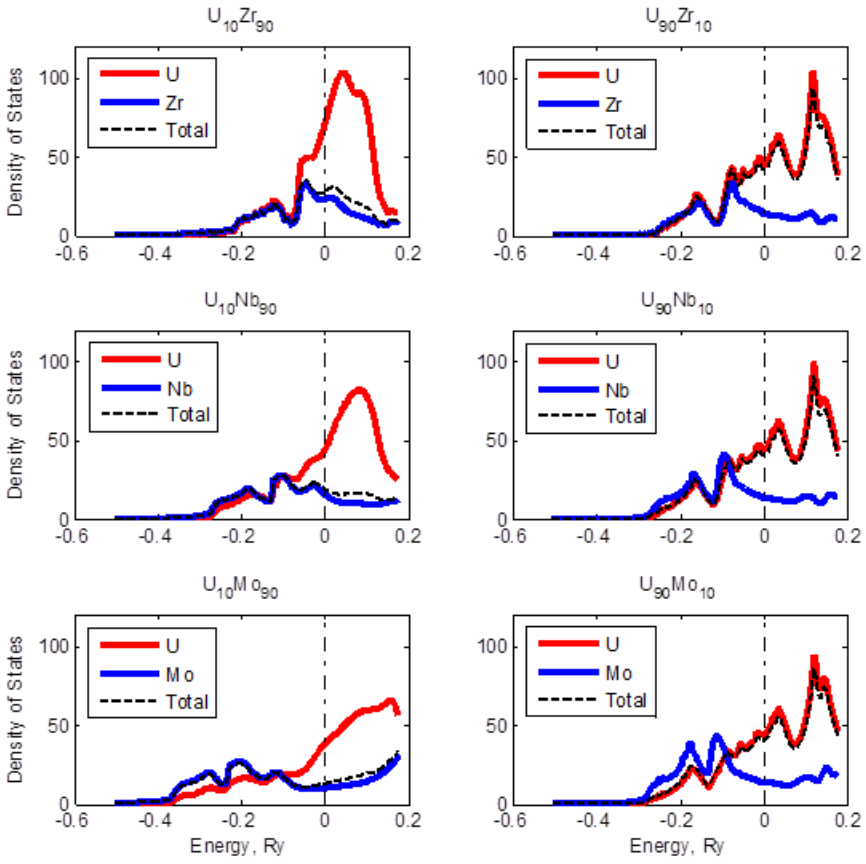

Figure 3.5: Calculated density of states of uranium-niobium relative to those of uranium-zirconium and uranium-molybdenum.

pecially true for the cases of Green's function approaches since both self-consistent loops for CPA and total energy get involved. Consequently, ground-state heats of formation were not evaluated for those phases. Nevertheless, the bcc's $0K$ formation energy is alone sufficient enough for imposing a solid quantum-originated constraint to the CALPHAD's optimization process, as evidenced in the following thermodynamic assessment.

3.2 CALPHAD modeling of uranimun-niobium's thermodynamics

Within this section, fundamental thermodynamics of uranium-niobium is first assessed using CALPHAD method, taking into account previous experimental data as well as the current first-principles constraints. The resulting thermodynamic representation is checked against our supplementary equilibria of the $\gamma_2/\alpha + \gamma_2$ phase boundary measured by long-term aging experiment. The proven thermodynamic representation is then used to assess atomic mobility and diffusivity of the body-center cubic phase, γ. Together, thermodynamic and kinetic data will essentially enable the phase-field LE investigations, carried out later in this work.

3.2.1 Experiments and parameter optimization

Studies of Nb-based metallic fuel mainly focus on its thermodynamic properties and many important works can be dated back to 50s and 60s. In particular, Sawyer [143] pioneered the studies of uranium-niobium phase stabilities in 1947 by sketching a nearly complete phase diagram of the material. In 1952, Saller etal [144] focused their study on a portion of uranium-niobium phase diagram and proposed a change regarding the solubility of Nb in U matrix. In particular, they recommended a eutectoid instead of peritectoid reaction for the $\beta - \gamma$ transformation. This idea was soon paced by Rogers *et al.* [2] whose work in 1958 is among the most comprehensive. Interestingly, in the same year (or close) another important study by Pfeil *et al.* [38]

showed agreement with Sawyer's work. The result was obtained by applying the lever rule to the volume fraction observed from metallography in comparison to the resistivity and dilatometry measurements of Rogers *et al.* Discrepancies increased in 1961 when Ivanov *et al.* [145] proposed the monotectoid reaction occurring around 13 *at.*% Nb. According to them, $\gamma - U$ should decompose into a mixture of $\gamma - Nb$ and β instead of $\gamma - Nb$ and α as proposed in previous works [2, 38, 146]. The opinion of Ivanov *et al.* was latter supported by Terekhov [147] and Massalski *et al.* [40] but disagreed by Elliott *et al.* [148] and Chiotti *et al.* [149]. In 1998, Koike *et al.* [39] analyzed previous works [1, 2, 4, 30, 38, 143, 145, 147, 150, 151, 152, 153, 154, 155] and came up with a phase diagram evaluated by considering the most reliable experimental data. Their evaluation has been adopted in the present work in conjunction with the *ab initio* energetic data calculated earlier [142].

As a common practice, details on the parameter optimization are presented as follows. Firstly, the random solution model [156] was considered for all uranium-niobium phases including γ (bcc), α (orthorhombic), β (tetragonal) and liquid. For the details of the model, one may refer to the methodology section. Here, the a_ν^ϕ and b_ν^ϕ parameters (see Eq. 2.37 and Eq. 2.39 for details) were optimized using Themo-Calc's PARROT module according to the following strategy. Initially, only the bcc phase was considered. The temperature independent parts of bcc (i.e. a_ν^γ) were fitted to the EMTO energetic data. It was found that a minimum value of 3 is required for n to reasonably reproduce the first-principles energies. a_ν^γ were then kept fixed during the optimization process of b_ν^γ to (1) reduce the total degrees of freedom of the PARROT's optimization process and (2) improve the consistency between CALPHAD methodology and *ab initio* calculations.

The optimization of temperature dependent b_ν^γ was carried out by firstly introducing driving force constraints for the phase at various temperatures and concen-

trations, according to Koike's *et al.* evaluated phase diagram. This thermodynamic constraint is defined as an affinity between reacting chemical species and has a negative value where its corresponding phase is stable. The introduction of bcc's driving force constraints forged out the double-well shapes of this phase's potentials at elevated temperatures. It is noted that both Nb- and U-ends of these double-well potentials were constrained in accordance with the SGTE database [77]. At this stage, the topology of γ- Gibbs free energy has been properly reflected by the interaction parameters but the domain in which the energy's values can range was fairly large. To restrict this domain, Vambersky's *et al.* [4] Gibbs formation energies, measured at 1048 K and 1173 K, were introduced.

Table 3.1: Optimized thermodynamic parameters for uranium-niobium system.

Phase	**Model**	**Parameters**
Liquid	$(Nb,U)_1$	${}^0L^{Liq}_{Nb,U} : 102268.08 - 76.90T$
Bcc	$(Nb,U)_1(Va)_3$	${}^0L^{bcc}_{Nb,U} : 28681.96 - 30.20T$
		${}^1L^{bcc}_{Nb,U} : -25306.13 + 2.74T$
		${}^2L^{bcc}_{Nb,U} : -37741.52 + 7.27T$
		${}^3L^{bcc}_{Nb,U} : -13979.73 - 3.74T$
Tet.	$(Nb,U)_1$	$G^{\beta U}_{Nb} = G^{bcc}_{Nb} + 21241.93$
Orth.	$(Nb,U)_1$	$G^{\alpha U}_{Nb} = G^{bcc}_{Nb} + 22505.03$

In the following step, the α, β and liquid phases – or to be precise, the interaction parameters of these phases – were brought into the optimization process, in addition to the existing bcc phase. The inclusion of these additional phases further tuned up

the curvature of γ-Gibbs free energy, as well as carved their own energetic profiles, in such a way that reasonable equilibria (or phase boundaries) were achieved between the pairs of $\gamma - \alpha$, $\gamma - \beta$ and $\gamma - liquid$, i.e. tie-line constraints being satisfied. Note that during this process, relative stabilities among the added phases must also be guaranteed. Finally, a_ν^γ was allowed to relax together with other parameters for a better agreement between the calculated and reference phase diagram [39]. The resulting optimized values were reported in Table 3.1.

3.2.2 Results and discussions

Fig. 3.6 and Fig. 3.7 show the phase diagram of uranium-niobium system calculated using these optimized parameters. Specifications of its invariant reactions are listed in Table 3.2. It can be seen from the figure that the liquidus and solidus lines agree reasonably with the experimental data [2], and as such they are compatible with those from other works [38, 40, 5]. Good agreements between calculations and experiments [38, 153, 155] are observed within the U-rich monotectoid region, in particular at the $\beta + \gamma$ boundaries and eutectoid reaction (refer to Table 3.2). Near the monotectoid invariance, the γ-U+Nb miscibility gap appears to be slightly broader than what was evaluated by Koike *et al.* [39] but still within the experimental bound [2]. Also, it does not suggest a sinusoidal-like curvature as estimated in Koike's *et al.* work. Investigations of free energies within this miscibility gap show small deviations with respect to the previous calculations of Liu *et al.* [5], that tend to reasonably agree with Vambersky's *et al.* experiments [4] taking into account the experimental errors (see Fig. 3.8). Back extrapolation of Gibbs free energies of the bcc phase to 0 K is compatible with the first-principles energetic data with maximum deviation of the order of $\sim 2.0\ Kj/mol$ (see Fig. 3.9). In the monotectoid reaction, it can be seen from Table 3.2 that the Nb-content of reactant (13.3 $at.\%$ Nb) agrees

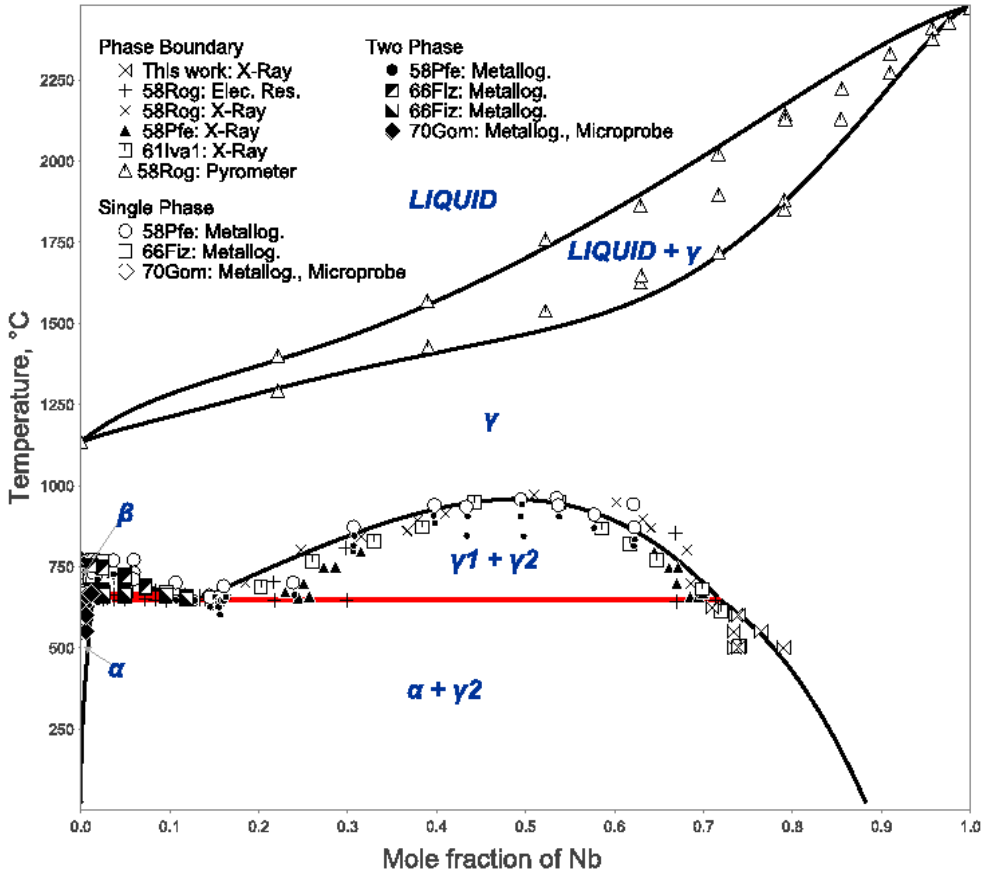

Figure 3.6: Calculated phase diagram of uranium-niobium system in comparison to experimental data.

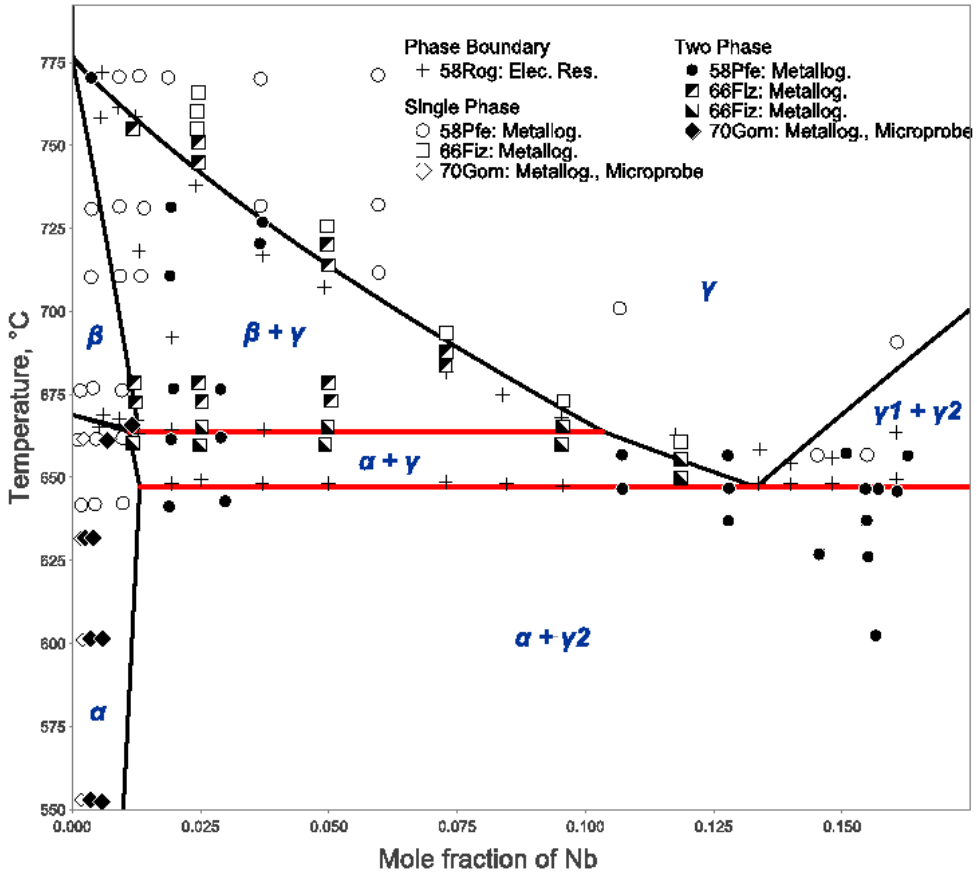

Figure 3.7: U-rich region of the calculated phase diagram of uranium-niobium system.

Table 3.2: Accessed invariant reactions in comparison with previous works

Type	**Reaction**	**Compositions (at% Nb)**			**T(C)**	**Reference**
Eutectoid	$\beta U \rightarrow \alpha U + \gamma U$	1.3	0.5 - 0.9	10.5 - 11.5	664	Koike *et al.* [39]
		1.3	1.09	10.1	664	Liu *et al.* [5]
		1.3	1.1	10.35	664	This work
Monotectoid	$\gamma U \rightarrow \alpha U + (Nb)$	13.3	0.5 - 0.9	68 - 72	647	Koike *et al.* [39]
		13.9	1.3	70	647	Liu *et al.* [5]
		13.3	1.3	71.7	647	This work
Critical	$(\gamma U, Nb) \rightarrow \gamma U + (Nb)$		52.3		930 - 970	Koike *et al.* [39]
			50.7		958	Liu *et al.* [5]
			48.6		957	This work

very well with that evaluated by Koike *et al.* [39], it lies well within the suggested range for the γ- product (71.66 *at.*% Nb vs 68-72 *at.*% Nb) but is relatively high for the α- product (1.3 *at.*% Nb vs 0.5-0.9 *at.*% Nb). Consequently, the α phase region below this reaction is likely to overstate the solubility of Nb in U-matrix [155] although it is computationally consistent with that calculated by Liu *et al.* [5].

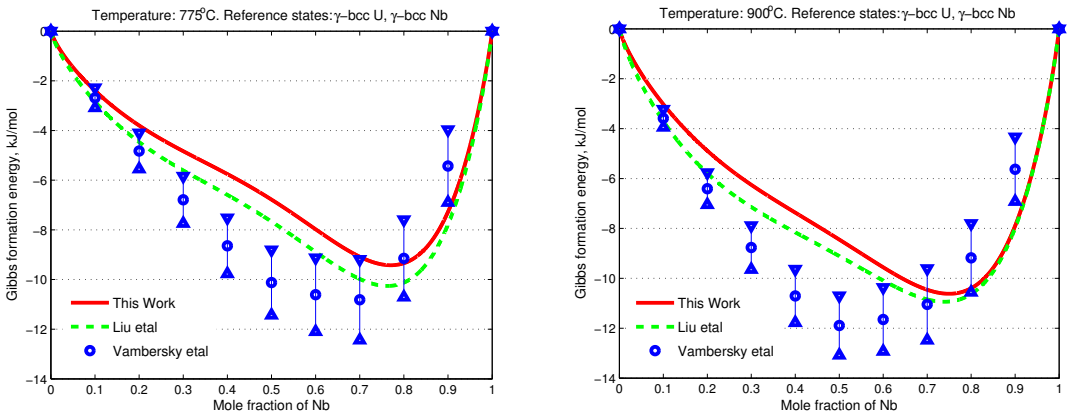

(a) (b)

Figure 3.8: CALPHAD-assessed Gibbs formation energy of bcc phase evaluated at 775^0C and 900^0C as compared to experiment [4] and previous calculation [5].

The most important difference between the present phase diagram and its predecessor [39] lies in the specification of $\gamma_2/\alpha+\gamma_2$ boundary. In particular, this boundary was predicted to be relatively steep in the previous work compared to its being gradual in the current study. This steep $\gamma_2/\alpha+\gamma_2$ boundary was sketched based on the curvature of the $\gamma-U+Nb$ miscibility boundary and two available x-ray diffraction (XRD) data-points from Ivanov *et al.* [145] at 500^0C and $\sim 600^0C$. Note that no explicit tempering durations were reported for these experiments; Instead it was implied as being short [145]. Considering the sluggishness of uranium-niobium within

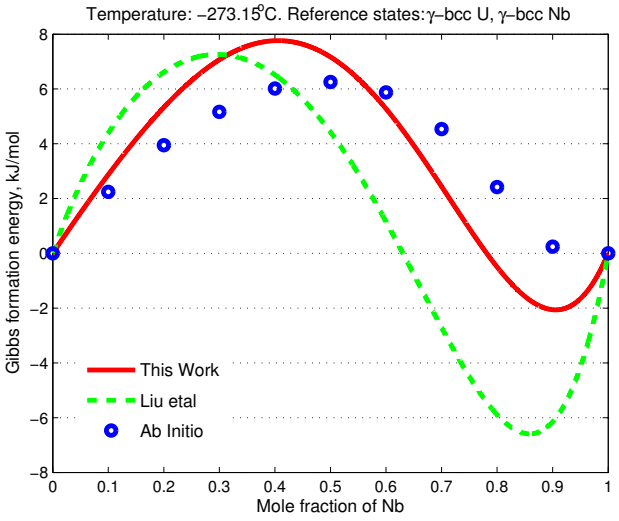

Figure 3.9: Comparison between the current 0 K CALPHAD-assessed Gibbs formation free energy with the current first-principles energetic calculations and previous work [5]. Good agreement between CALPHAD assessment and first-principles calculation manifests a better thermodynamic consistency of the CALPHAD assessment than that of [5], which appears to be more to the experimental side (see Fig. 3.8).

the $\alpha + \gamma$ region, these experimental data may not be so reliable. Indeed, Koike *et al.* has cautiously represented in their work a dashed-line $\gamma_2/\alpha + \gamma_2$ boundary to indicate that further investigations are needed. Fortunately, in this study we got reliable phase equilibria at the $\gamma_2/\alpha + \gamma_2$ boundary supplied by the experimentalists at LANL. For these data, X-ray experiments were carried out for considerably long annealing time. In particular, long-term heat treatment was conducted on specimens taken from two plates of nominal composition U-17.4 *at.*% Nb (chemical analysis showed 17.2 and 17.6 *at.*% Nb.) The alloys were vacuum induction melted from high purity depleted uranium and niobium stock, cast into graphite molds, hot rolled, and homogenized 6 hours at 1000^0C. Specimens were solution annealed 30 minutes at 850^0C under encapsulation and water quenched. They were re-encapsulated and then isothermally aged at over $300 - 625^0C$ for up to 5 years. The lattice parameters

(LPs) of the α and γ phases in the DC products were measured using XRD with ceria standards and full-pattern Rietveld analysis. Specimen preparation, XRD setup, and pattern analysis were the same as that reported earlier [22]. The microstructures were characterized by light-optical and scanning electron microscopy; all ages had 100% DC (or very close to this). For all ages, the α-U phase exhibited LPs close to their equilibrium value. The γ_2 LP values varied more vs. age, which was expected on the assumption that this variation was due to different niobium concentrations in the phase. They were converted into an equivalent Nb atom fraction x_{Nb} using the linear relationship for LP [25]:

$$LP(\gamma_2) = 3.475 - 0.175 \times x_{Nb}, \tag{3.3}$$

where the LP is in Angstroms. The experimental results, reported in Table 3.3, indicated that Nb content of γ_2 is likely to increase with increasing aging time, and the longest experiments are actually in very good agreements with the current assessed phase boundary (refer to Fig. 3.6 above). In other words, they justifies for the reliability of the current thermodynamic assessment. Here, it should be noted that these supplemental XRD data were only used for verification purpose, i.e., they were not included in the optimization process. This practice is known well in the field of Modeling as a method to check for the generalizations of parameterized functions, e.g., R-K polynomials within this context.

Table 3.3: $\gamma_2/\alpha+\gamma_2$ phase boundary data. Here, bulk alloy γ_1 is U - 17.4 $at.\%$ Nb. X-Ray measurements of γ_2 compositions after long-period aging were carried out at 500^0C, 550^0C and 600^0C. Experimental results indicate that γ_2 composition tends to increase with increasing annealing period.

T(C)	**Nominal time (Hours)**	γ_2 **composition** ($at.\%$ **Nb**)
500	5300	73.5
500	17532	73.9
500	43830	79.0
550	5300	73.4
550	17532	76.5
600	5300	73.6
600	10600	73.9
625	10600	71.0

Fig. 3.10 shows the calculated metastable phase diagram of γ in comparison with one predicted by Liu *et al.* [5]. It can be seen from the figure that the metastable phase diagram assessed in this study does not show an inverse miscibility gap for the cubic phase as it does in Liu's *et al.* work. As previously mentioned, this thermodynamic phenomenon is likely to be an assessment artifact in metallic binary systems. It has been demonstrated in [41] and the present work that the addition of first-principles energetic data to CALPHAD's optimization process has actually restrained this phenomenon and perhaps other "hidden" artifacts from existing within the solution space defined by the optimized interaction parameters.

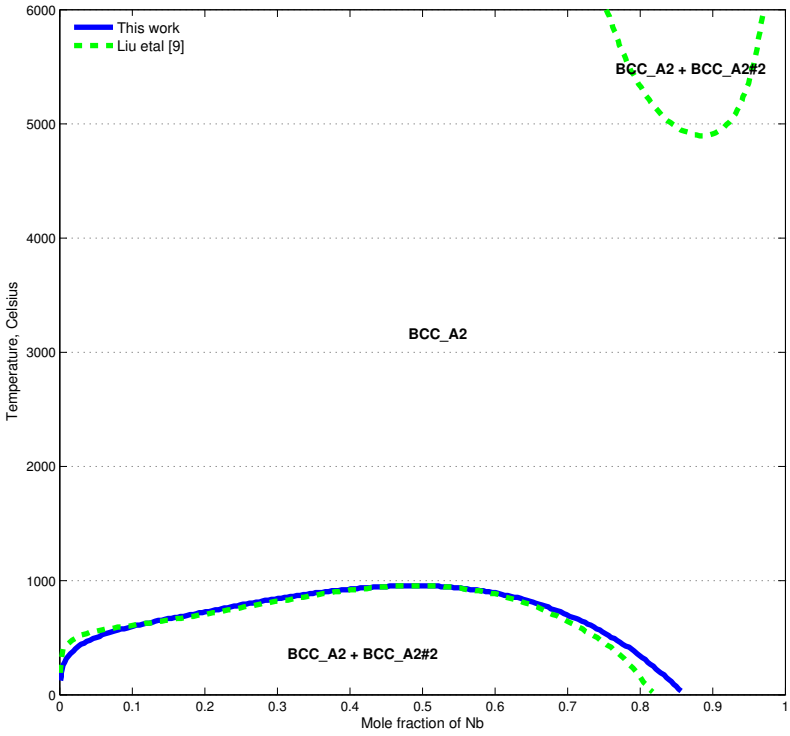

Figure 3.10: Calculated metastable phase diagram of the bcc phase.

3.3 CALPHAD modeling of γ's atomic mobility

Atomic mobilities and diffusion coefficients are of great importance in simulating and understanding the microstructure evolutions of materials. In the context of phase-field modeling, particularly the one implemented later in this work, they serve as sufficient kinetic information which together with essential thermodynamic data fulfill the prerequisites of the phase-field method. With the achievement of the self-consistent thermodynamic description above, it naturally leaves in this section the discussion of these kinetic quantities.

3.3.1 Experiments and parameter optimization

The DICTRA optimization process was carried out taking into account the above self-consistent thermodynamic description. To facilitate this process, the mobility parameters of end-members were adopted from Liu's *et al.* [6] work. It is noted here that the current diffusion assessment and Liu's *et al.* [6] share a common goal and approach but differ fundamentally in thermodynamic databases used. In Liu's *et al.* [6] work, the PARROT optimization of Liu *et al.* [5] was utilized. This fundamental difference however does not much affect the mobilities of end-members which are weakly dependent upon the alloy's thermodynamics. Consequently, the adoption of these quantities, practiced in the present work, is fully valid, especially when considering good agreement between calculations and experiments of tracer and impurity diffusivities acquired in [6]. In contrast, the interaction parameters, which characterize chemical exchanges and correlations within the alloy system, strongly depend on the system's chemical potentials and hence are expected to alter consistently with the change of thermodynamic database. Here, the interaction parameters were optimized using the experimental tracer diffusivities taken from Adda *et al.* [157] and Fedorov *et al.* [158] and the interdiffusivities measured by Fedorov *et al.* [7].

Table 3.4: Optimization kinetic parameters for the bcc phase of uranium-niobium system.

Phase	**Model**	**Mobility**	**Parameters**
Bcc	$(U, Nb)_1(Va)_3$	U	$\phi_U^{U:Va} : -112127.11 - 132.24 \times T$ [6] $\phi_U^{Nb:Va} : -387210.79 - 127.09 \times T$ [6] ${}^0\phi_U^{Nb,U:Va} : 81130.73$ ${}^1\phi_U^{Nb,U:Va} : 491786.57 - 357.62 \times T$
		Nb	$\phi_{Nb}^{Nb:Va} : -395598.95 - 82.03 \times T$ [6] $\phi_{Nb}^{U:Va} : -107072.73 - 181.63 \times T$ [6] ${}^0\phi_{Nb}^{Nb,U:Va} : -256479.19 + 135.86 \times T$ ${}^1\phi_{Nb}^{Nb,U:Va} : -205726.88$

3.3.2 Results and discussions

Optimization results are shown in Table 3.4. Fig. 3.11 compares the present calculated interdiffusion coefficients at 1273 K with ones from experiment [7] and previous calculations [6]. It can be seen from the figure that the present calculated interdiffusivity at 1000^0C is compatible with the previous calculation [6] as well as experiment [7]. This justifies the current CALPHAD assessment of atomic mobility and diffusivity. Here, it is noted that the diffusion assessment is limited to only bcc uranium-niobium. This is due to the lack of kinetic data for the other phases, particularly the one of interest: α. In the following section where the atomic mobility and interdiffusivity of α are needed, it is assumed that the kinetics of this phase is generally faster than that of the bcc phase. This assumption is based on the fact that the atomic packing factor of α is smaller than that of γ, i.e. more free space for atomic transport.

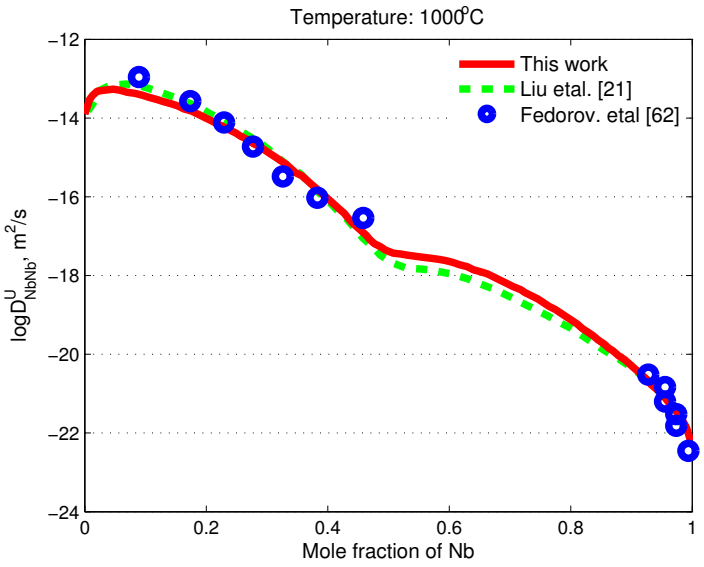

Figure 3.11: Calculated interdiffusivity of uranium-niobium system at 1000^0C as compared to previous calculation [6] and experiment [7].

3.4 Phase-field investigation of Djuric's hypothesis on the occurrence of discontinuous precipitation

With proven and reliable thermodynamic and kinetic representations achieved in the previous sections, phase-field simulations are carried out in the current section to examine Djuric's hypothesis on the origin of uranium-niobium's discontinuous precipitation and coarsening [1]. In particular, interface dissipation model [36] is implemented in place of a Gibbs free-energy minimizer, or LE finder, to find out whether, within the temperatures of interest, α would form with γ (with initial composition γ_1) two LE: one at the observed intermediate γ_{1-2} composition and the other at the stable γ_2 composition as Djuric assumed. The favor of the phase-field model over a conventional free-energy minimizer, such as one used in the Thermo-Calc package, is due to the fact that the phase-field model is not only an energy minimizer but also, in its full course, a scientific tool of choice to study out-of-

equilibrium microstructure evolutions and phase transitions. In this regard, it offers the advantages of:

- being able to take into the energy-minimization function the account of phase (or microstructure) evolutions in addition to physical changes such as chemical composition, temperature, grain orientation, etc.

- demonstrating with insights how the γ_{1-2} LE [1], if existed, functions to interrupt the monotectoid decomposition in the uranium-niobium system and temporally traps it at the metastable state.

- preparing an integrated CALPHAD - phase-field framework for future investigations of microstructure evolutions and phase transitions in the uranium-niobium system such as the lamellar growth in DP and DC reactions or the spinodal decomposition of γ.

The phase-field studies show that the proven-reliable CALPHAD free energies on one hand disagree with Djuric's hypothesis at temperatures between 400^0C and 605^0C, but on the other hand are consistent with the thermodynamic assumption at higher temperatures between 605^0C and 630^0C. In favor of Djuric's hypothesis, we revisit the assessed CALPHAD free energies between temperatures ranging from 400^0C to 605^0C and find that it is still possible to accommodate the hypothesis within the lower temperature range by taking into account an additional strain energy due to volume/lattice mismatch between α and γ. It is argued that while at high temperature the strain energy is small and could be reasonably captured by CALPHAD, its higher value is likely to be underestimated at lower temperature. To quantify this additional strain energy, new energetic profiles are constructed basing on the CALPHAD free energies and Djuric's hypothesis. Within the context of this work, these

energies are called strained-adjusted free energies. The new energies are then used to investigate whether or not stable lamellar growth of the discontinuous reactions may be reasonably achieved.

3.4.1 On the possibility of two local equilibria

To examine Djuric's hypothesis on the origin of uranium-niobium's discontinuous monotectoid decomposition, the interface dissipation model was implemented in place of a free-energy minimizer to investigate the CALPHAD free energies of α and γ for their possible LE (states of minimal energy). The idea is to utilize the proven and reliable CALPHAD description as a quantitative reference to examine Djuric's phenomenological hypothesis. The fundamental significance of this reference lies in the fact that it allows the thermodynamic hypothesis to be checked against the original thermodynamics of uranium-niobium. To better demonstrate this, we adapted the simple set theory as shown in Fig. 3.12. Within this figure, (set) A, B, and C indicate the by-nature thermodynamics of uranium-niobium, the ordinary thermodynamics of uranium-niobium approximated by CALPHAD, and Djuric's phenomenological hypothesis, respectively. Here, the exact boundary of A is unknown hence it is represented by a dashed line; B is however known explicitly and believed to belong to A since the CALPHAD assessment is in good agreement with experiments (note that B is believed to represent the core of A - the ordinary thermodynamics defining the uranium-niobium's equilibrium phase diagram); therefore it is proposed to be an available thermodynamic reference to examine C. According to the set theory, C has three possible positions relative to B:

- C_1 belongs to B, i.e. Djuric's two-LE hypothesis is an inherent feature of the CALPHAD ordinary thermodynamics. Since B also belongs to A, this makes C_1 is the subset of A. In other words, unless there exists a stronger mechanism

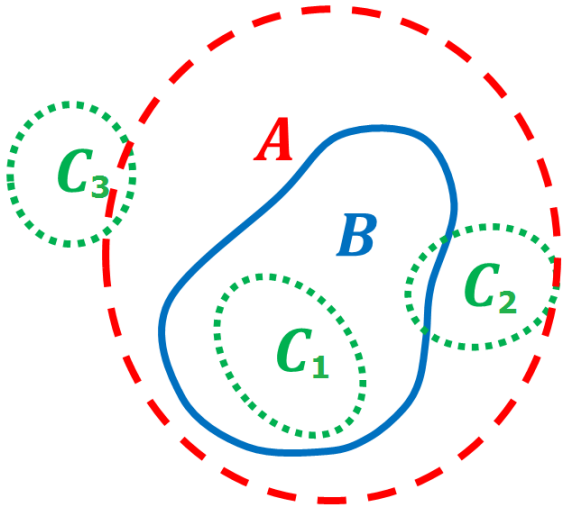

Figure 3.12: Set theory to demonstrate the usage of CALPHAD thermodynamic reference in examining Djuric's hypothesis. Here, A represents the thermodynamics of uranium-niobium by nature; B represents the ordinary thermodynamics of uranium-niobium approximated by CALPHAD; C represents the two-LE phenomenon hypothesized by Djuric [1].

to stabilize the metastable γ_{1-2} phase, it is highly possible that the thermodynamic hypothesis explains the discontinuous monotectoid decomposition.

- C_2 intersects B, i.e. the two-LE hypothesis is only partially accounted for by the CALPHAD description. Although this is not as conclusive as in the first case, it still makes C_2 one possible subset of A. In other words, the thermodynamic hypothesis may still be valid. In this case, further investigations are needed to see if C_2 could possibly belong to A.

- C_3 is far away from B, i.e. the CALPHAD description does not feature two LE at all. This makes C_3 less likely to be a subset of A. As a consequence, the possibility of Djuric's hypothesis being valid, is low. Here, it would also require further investigations as in the second case to verify whether C_3 really does not have any thermodynamic correlations with A.

To find possible LE between the CALPHAD energies of α and γ using the proposed phase-field model, it is found that the diffusion-couple-type simulation is ideal for its simplicity, i.e. 1-D, yet sufficient, i.e. LE is sufficiently indicated when the Kirkendall interface stops moving, its driving force vanishes, and the compositions of two reacting phases are homogeneous. The schematic demonstration of the phase-field diffusion couple is shown in Fig. 3.13. For computational details, the couple of interest is 1 μm long and initially consists of 0.1 μm of α and 0.9 μm of γ. It has a total of 500 grid points with the step of 2 nm and interfacial width of 10 nm. The initial compositions of α and γ are 1 $at.\%$ Nb and 13 $at.\%$ Nb respectively. To estimate thermodynamic driving force (in form of energy density $[J/cm^2]$), the assessed CALPHAD energetic data are used, see Fig. 3.14; for simplicity, the used molar volumes for this estimation are assumed to be constant and take the average value of those from the initial orth and bcc phases. The interfacial energies are taken as the

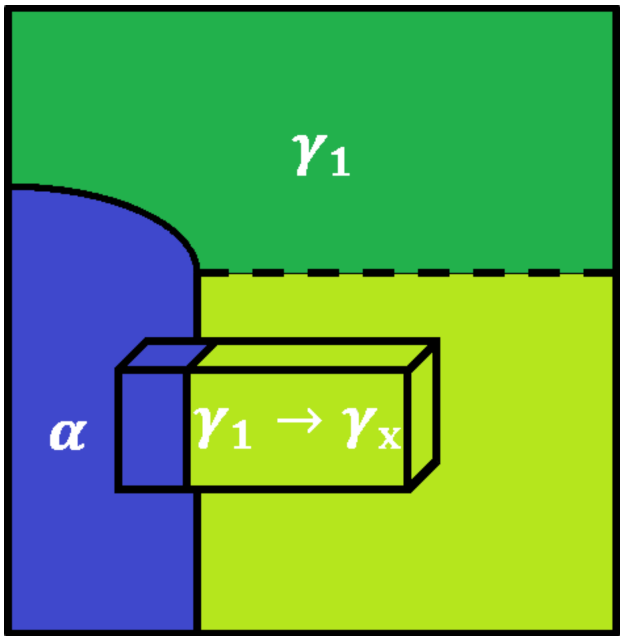

Figure 3.13: Schematic representations of diffusion-couple simulations to investigate the LE between α and γ. Here, the convergence product of α and γ_x depicts a LE between α and γ. The dash line indicates the boundary between the two same crystallographic bcc phases, to differentiate with boundaries separating different crystallographic structures.

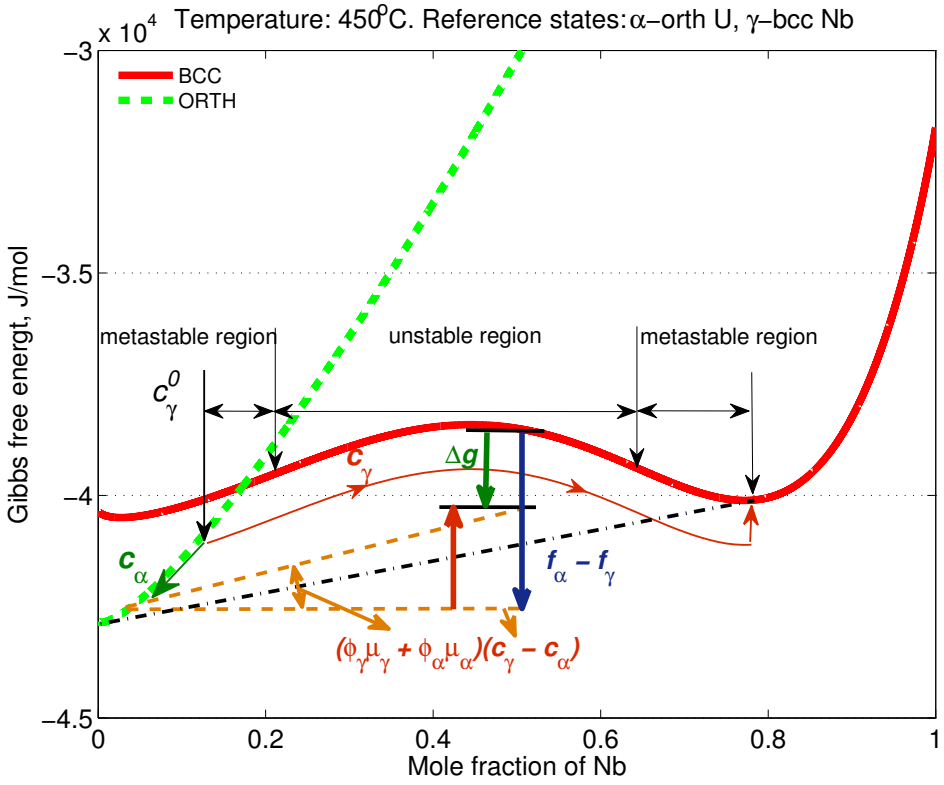

Figure 3.14: CALPHAD free energies used for the phase-field investigations of possible LE between α and γ. The red and green arrows along the free energetic profiles schematically describe the evolutions of the compositions of α and γ at the interface of the diffusion couples, namely c_α and c_γ, that would occur within the phase-field simulations. Here, the values of c_α and c_γ at which the phase-field simulations would converge indicate the LE compositions of α and γ, respectively. The driving force $\triangle g_{\alpha\beta}^{phi}$ of the phase-field model is also demonstrated by the green top-down arrow which is the subtraction of the energy needed for compositional changes or diffusions, i.e. the red bottom-up arrow, from the total energy available, i.e. the top-down blue arrow.

averages of those evaluated in [31]. The interfacial mobilities are chosen according to our empirical formula: $\mu = 10^7 \frac{D_i M_i}{D_i + M_i}$, where $i = \alpha$ or γ; M is the value of atomic mobility and D is the value of interdiffusivity. Here, the atomic mobility and interdiffusivity of γ are taken from the current assessed DICTRA database; basing on the atomic packing factors of orth and bcc, it was assumed that the atomic mobility and diffusivity of α are three times faster than those of γ; since these kinetic coefficients do not affect the thermodynamic LE between the two reacting phases, their precise values are of only peripheral interest within the scope of this work. Nevertheless, it is noted that kinetic factors can play an important role in determining the lamellar microstructure of DP, as demonstrated later in this work; therefore a comprehensive knowledge of these physical quantities is beneficial for future developments and applications of the nuclear material. A summary of all models and physical parameters used in this work can be found in Table 3.5. For solving the model's evolution equations, finite-difference method was utilized. The numerical stability of this linear solver was supported by dynamic time step. To further improve the efficiency of our simulations, the arithmetic average of driving force ($\triangle g_{\alpha\beta}^{phi}$) for phase-field evolution is taken over the interface, as suggested by Steinbach *et al.* [36].

Simulation results of the phase-field diffusion couples at 450^0C and 550^0C are shown in Fig. 3.15. Here, the 3-D plots represent the evolution of the diffusion-couple interface (i.e. the $\alpha|\gamma$ interface) with respect to distance (x-axis), time (y-axis) and composition (z-axis). The solid (green) lines with arrows in the 3-D plots indicate the evolutionary path (and directions) of the composition of γ at the interface during the phase transformation. The insets feature the average chemical driving force, $\triangle g_{\alpha\beta}^{phi}$ (see Eq. 2.85), at the diffusion-couple interface plotted as a function of γ's interfacial composition and the position of the interface. The color within the insets shows the order of magnitude of the chemical driving force (note that non-zero driving force

Table 3.5: Numerical and material parameters for the diffusion-couple simulations.

Parameters	Symbols	Values
Grid spacing	Δx	2.0 nm
Molar Volume	V_M	12.27 cm^3/mol [a]
Interface energy of DP	$\sigma_{\alpha\gamma}$	0.125×10^{-4} J/cm^2 [b]
Interface energy of DC	$\sigma_{\alpha\gamma}$	0.25×10^{-4} J/cm^2 [b]
Permeability	$P_{\alpha\gamma}$	$\frac{8M_\gamma}{a\eta}$
Lattice Parameter	a	3.5 $\mathring{A}$ [c]
Interface width	η	10.0 nm
Atomic mobility of α	M_α	$3 \times M_\gamma$
Atomic mobility of γ	M_γ	Database (this work)
Diffusivity of α	D_α	$3 \times D_\gamma$
Diffusivity of γ	D_γ	Database (this work)
Interface mobility	$\mu_{\alpha\gamma}$	$\frac{\varsigma D_\gamma M_\gamma}{D_\gamma + M_\gamma}$ cm^4/Js [d]

[a] *Approximate average of α-U and γ-U-50 at. % Nb molar volumes (taken from the EMTO data)*

[b] *Approximate averages of $\sigma_{\alpha\gamma}^{DP}$ and $\sigma_{\alpha\gamma}^{DC}$ reported in [31]*

[c] *Effective lattice parameter of choice, corresponding to V_M*

[d] *Proposed empirical formula where $\varsigma = 10^7$*

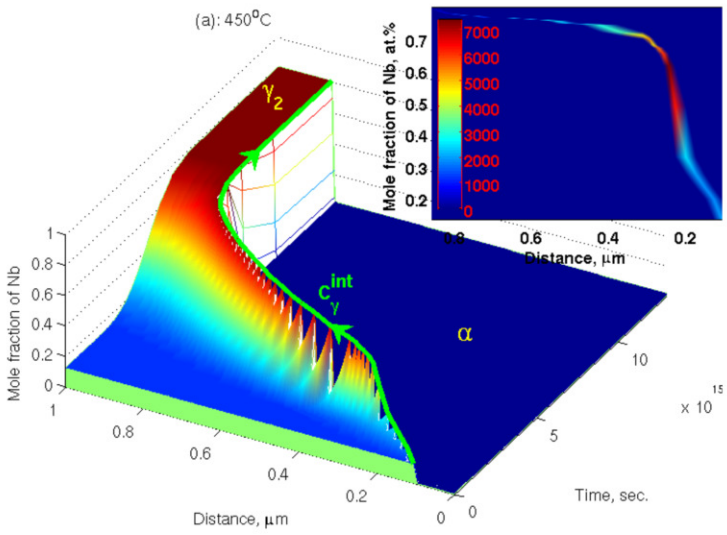

(a)

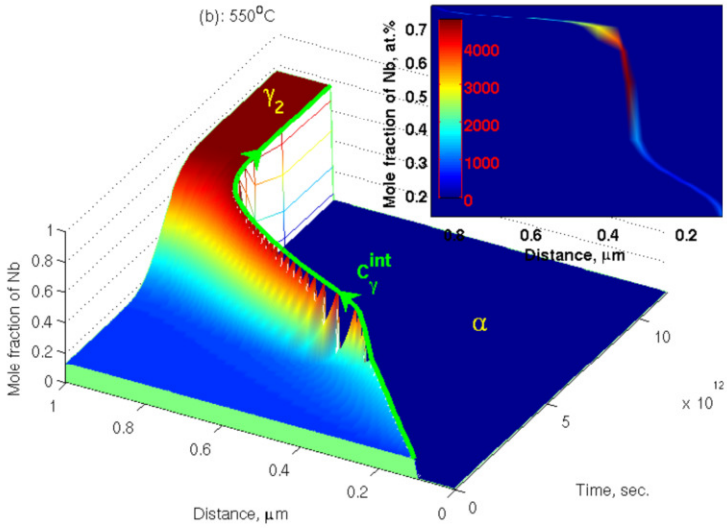

(b)

Figure 3.15: Phase-field investigations of possible LE between α and γ at 450^0C and 550^0C. Here, the α-growing / γ-shrinking processes of diffusion couples occur from right to left of the figures; the insets are the projections of the 3-D evolutionary paths of c_γ^{int} on the 'Mole fraction of Nb at.%' - 'Distance' plane and their colors indicate the magnitudes of the average chemical driving forces, $\triangle g_{\alpha\beta}^{phi}$, at the interface along these paths.

is only located around the projection of the evolutionary path of c_{γ}^{int} on the 'Mole fraction of Nb, at. %' and 'Distance,μm' axes and that since the initial setups of the diffusion-couple simulations are out-of-equilibrium all average chemical driving forces at the beginnings of the simulations are positive non-trivial values).

It can be seen from Fig. 3.15 that after the evolution time is larger than 1.0×10^{14} s for 450^0C or 2.0×10^{11} s for 550^0C the Kirkendall interface stops moving; the interface's chemical driving force, $\triangle g_{\alpha\beta}^{phi}$, vanishes (see insets); and, the compositions in both α and γ reach their homogeneous values across the phase regions. These all indicate that the interface dissipation model has found, for each temperature, one LE, at which the γ composition is identical to that of the stable γ_2 (79 at.% Nb for 450^0C and 76 at.% Nb for 550^0C) estimated by the free-energy minimizer of the Thermo-Calc package in the previous section (see Fig. 3.6 above). Some notes are:

- The sluggish evolution times (of orders 10^{14} $[s]$ for 450^0C and 10^{11} $[s]$ for 550^0C) result from the estimated CALPHAD's slow bulk diffusivity (in orders of 10^{-23} $[cm^2/s]$ for 450^0C and 10^{-21} $[cm^2/s]$ for 550^0C, consistent with the experimental values from Peterson and Ogilvie [159, 160]). In reality, the reaction happens much faster due to the so-called fast boundary-diffusion condition at the reaction front of DP [19], which will be addressed in a different phase-field study.

- The sudden increase in $\triangle g_{\alpha\beta}^{phi}$ from 40 to 60 at.% Nb for both simulation cases (red areas in insets) corresponds to the period within which the composition of γ at the $\alpha|\gamma$ interface, c_{γ}^{int}, evolves through the center of the unstable region of the bcc miscibility gap (see Fig. 3.14 for the schematic demonstration of c_{γ}^{int} evolution through the energetic profile at 450^0C). The significant driving force within this region urges c_{γ}^{int} to quickly leave the unstable region for the follow-

ing low-energy area of the γ_2 LE, essentially creating two noticeable necking points: one around 30 at.% Nb (vicinity of the first inflection point) and the other around 60 at.% Nb (vicinity of the second inflection point), along the evolutionary path of c_{γ}^{int} for both simulation cases.

Further phase-field investigations of $\alpha - \gamma$ LE for both 450^0C and 550^0C with initial composition of γ higher than γ_2 all showed a convergence back to the same equilibrium state at γ_2. This essentially indicates that within the CALPHAD energy landscape at 450^0C and 550^0C the orthorhombic phase, α, only form with the bcc phase, γ, one LE which corresponds to the stable $\alpha + \gamma_2$ products of the monotectoid decomposition; no LE can be found at the intermediate composition of γ_{1-2} as hypothesized by Djuric. As a matter of fact, it is found that single LE, i.e. $\alpha + \gamma_2$, is a common phenomenon throughout the temperature interval between 400^0C and 600^0C (actually up to 605^0C), within which Djuric's experiments were carried out. Given that the CALPHAD quantitative energies should capture a more precise thermodynamics than those phenomenologically hypothesized by Djuric (refer to Fig. 1.2 in page 17 for a reminder), would this defy Djuric's hypothesis?

Interestingly, it is found that, within the higher temperature range of the discontinuous monotectoid decomposition from 605^0C to 647^0C, the CALPHAD free energies of α and γ do form two LE with each other and the first LE does hinder the monotectoid decomposition at its intermediate state, very much consistent with Djuric's hypothesis. To illustrate this, simulation results of the phase-field diffusion couple at 605^0C are shown in Fig. 3.16. As evidenced by this figure, the interface dissipation model finds two LEs: one at an intermediate γ_{1-2} composition of 24.49 at.% Nb, as shown in Fig. 3.16 (a), and the other at the stable γ_2 composition of 73.95 at.% Nb, as shown in Fig. 3.16 (b). Note especially in Fig. 3.16 (b) that there is

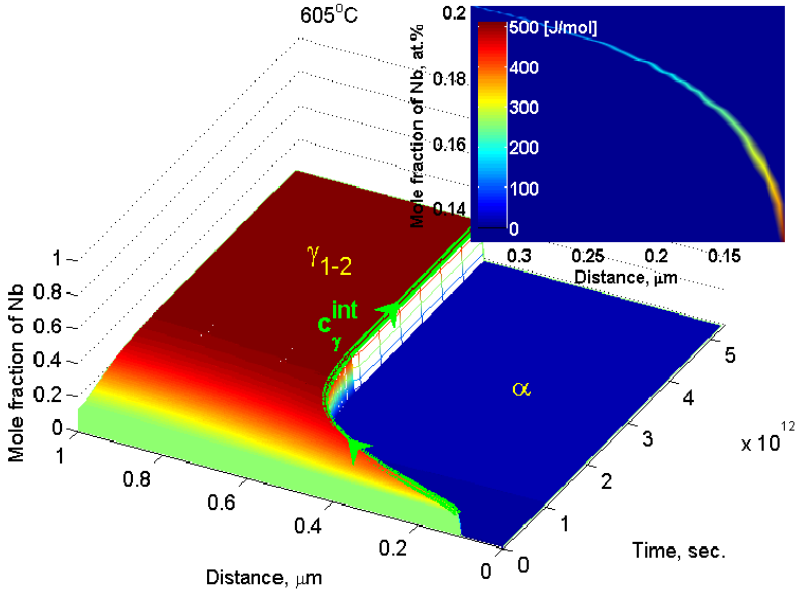

(a)

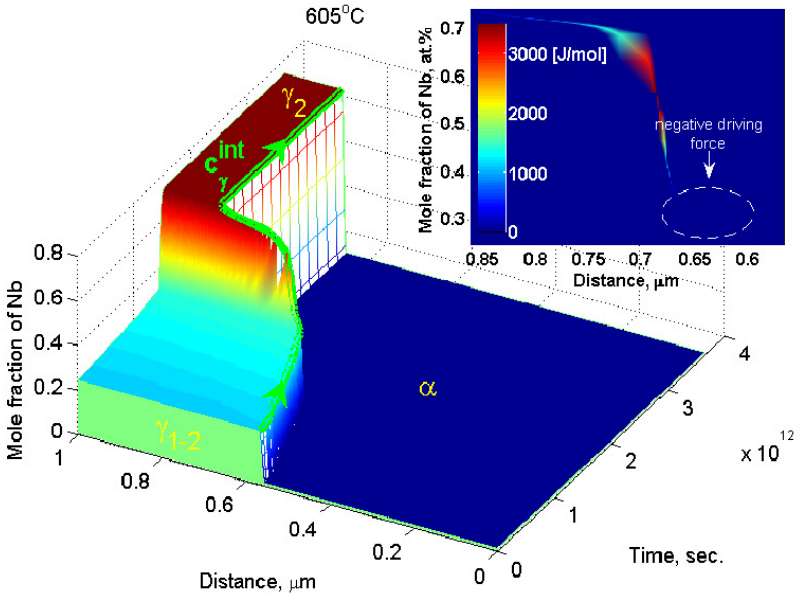

(b)

Figure 3.16: Phase-field investigation of possible LE between α and γ at 605^0C. Here, (a) indicates the first phase-field investigation of possible LE between α and γ free energies which converges at the first LE at 24.49 at.% Nb and (b) shows the continuation of the phase-field investigation after the first LE which eventually converges to the second LE, which is also the final stable state of the system, at 73.95 at.% Nb.

an interesting period within which the chemical driving force is negative and external driving drive has to be artificially introduced to compensate for the negative value and to get the diffusion-couple system to evolve; among all the presented simulation results, this is the only exception in which the chemical driving force does not start with a positive non-trivial value; explanation for the meaning of this negative driving force is given in the following.

Within the framework of phase-field modeling, the process of finding these LE progressed as follows:

- First, phase-field diffusion couple was started with the initial composition of γ at 13 at.% Nb. After the evolution time was greater than 2×10^{11} s, it was observed that the Kirkendall interface stopped moving, $\triangle g_{\alpha\beta}^{phi}$ converged to a value of almost 0 J/mol, and the compositions within the bulk phases reached their homogeneous states. In other words, the interface dissipation model found the system's first (or intermediate) LE whose γ's composition was 24.49 at.% Nb. Note here that the $\triangle g_{\alpha\beta}^{phi}$ distribution along the evolutionary path of c_{γ}^{int} and correspondingly the morphology of the path (inset of Fig. 3.16 (a)) are different from those at lower temperatures (see insets of Fig. 3.15); particularly, the $\triangle g_{\alpha\beta}^{phi}$ distribution and the evolutionary path of c_{γ}^{int} do not exhibit unusual peak and necking points respectively; this is due to the fact that c_{γ}^{int} has not yet passed through the first inflection point of the bcc miscibility gap to enter the gap's unstable region. Further prolonging the simulation did not lead to any significant changes. The almost-zero $\triangle g_{\alpha\beta}^{phi}$ at the found LE utterly shut down the system and trapped it there.

- In order to break this stasis and continue the phase-field investigation of $\alpha - \gamma$ LE, the composition of γ was slightly shifted to a higher value while keeping the

composition of α unchanged. The simulation result interestingly showed that, within this small deviation, the system tended to converge back to its initial LE. This was because here $\triangle g_{\alpha\beta}^{phi}$ had negative values which tended to reverse the compositional increment in order to bring down the system's total energy. In other words, there existed a finite energy barrier after the first LE which tentatively prevented the system from further evolving to higher γ-composition after the first LE. This energy barrier together with the vanishing of driving force (before the LE as described above) form an effective two-fold obstacle introduced by an intermediate LE, if it existed, which proceeds to interrupt the monotectoid decomposition and cause DP.

To force the system to overcome the energy barrier, a positive driving force was artificially introduced into the reacting interface in order to counter the negative value of $\triangle g_{\alpha\beta}^{phi}$ when it was observed. This artificial driving force could in reality be legitimated by the fact that the relaxation of internal stresses (due to volume/strain mismatch) between α and γ lamellae (with γ_{1-2} composition), that tends to start first at the grain boundaries between the two γ grains (with γ_1 composition, within which the lamellae nucleates and grows) after some sufficient aging time, will essentially break down the first LE between α and γ (by altering their free energies to lower values) and likely put the system into an out-of-equilibrium condition with non-trivial thermodynamic driving force to continue evolving. During the introduction of artificial driving force, it was observed that the peak of the energy barrier that the system had to overcome was about 18.65 J/mol, as shown in Fig. 3.17.

- When $\triangle g_{\alpha\beta}^{phi}$ turned positive, the artificial driving force was removed to allow the evolution of the system to resume as normal. At this moment, the system

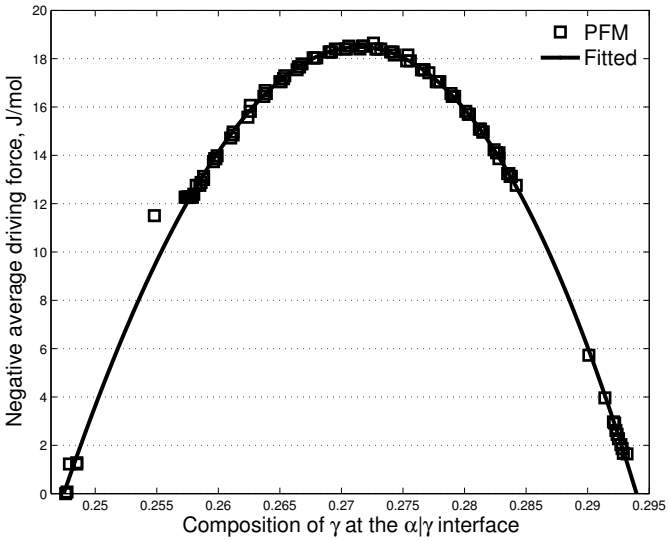

Figure 3.17: Energy barrier introduced by the intermediate local equilibrium after the γ_{1-2} composition to hinder the discontinuous monotectoid decomposition. Note that negative average driving force at the interface, $-\triangle g^{phi}_{\alpha\beta}$, is reported in this figure.

had already entered the unstable region of the bcc miscibility gap. The driving force here was so significant that it dramatically drove the system all the way out of the unstable region (refer to the inset of Fig. 3.16 (b) for details). When the system's c^{int}_{γ} passed through the second inflection point of the miscibility gap, $\triangle g^{phi}_{\alpha\beta}$ started converging and eventually brought the system to its second LE located at the γ_2 composition of 73.95 at.% Nb. Note here that the entire subprocess after the first DP reaction (the first LE) practically represented the later DC reaction: $\alpha + \gamma_{1-2} \rightarrow \alpha + \gamma_2$. After this, the system again stayed idle at the γ_2 LE. Further phase-field investigations at higher γ-compositions did not result in any additional LE. The interface dissipation model found a total of two LE between α and γ in comparison to only one LE in the previous

findings at lower temperatures.

To confirm this, an additional minimization was implemented in a MATLAB script to double check the number of LE between α's and γ's CALPHAD free energies. The minimization is conventionally with respect to composition and at a specific temperature. The size of compositional domain for each LE search is controllable, and the considered temperatures are from both $400^0C - 605^0C$ and $605^0C - 647^0C$ ranges. It was found that the CALPHAD free energies of α and γ indeed form two LE with each other within the temperature range of $605^0C - 647^0C$ while they exhibit only one LE within the temperature range of $400^0C - 605^0C$, consistent with the phase-field investigations.

According to the set theory proposition mentioned earlier (see Fig. 3.12), the observation of two LE between α and γ within the temperature range of $605^0C - 647^0C$ (or the union of C and B) tentatively indicates that Djuric's hypothesis is a possible explanation for the origin of uranium-niobium's discontinuous monotectoid decomposition (C possibly belongs to A, i.e. C_2). Yet, this indication is not conclusive due to the fact that the CALPHAD free energies show only one LE within $400^0C - 605^0C$. Here, in favor of the thermodynamic hypothesis we revisited the CALPHAD free energies within the temperature range between 400^0C and 605^0C. The goal was to go beyond CALPHAD to see if there exists an extraordinary condition under which the CALPHAD energies could be extended to accommodate the hypothesis. In terms of the aforementioned set theory, this condition, if it existed, would legitimate the union of C into A.

3.4.2 Strain effect on the two local equilibrium assumption

To find out what this condition could possibly be, we empirically sketched out new energetic profiles based on the CALPHAD free energies and following Djuric's

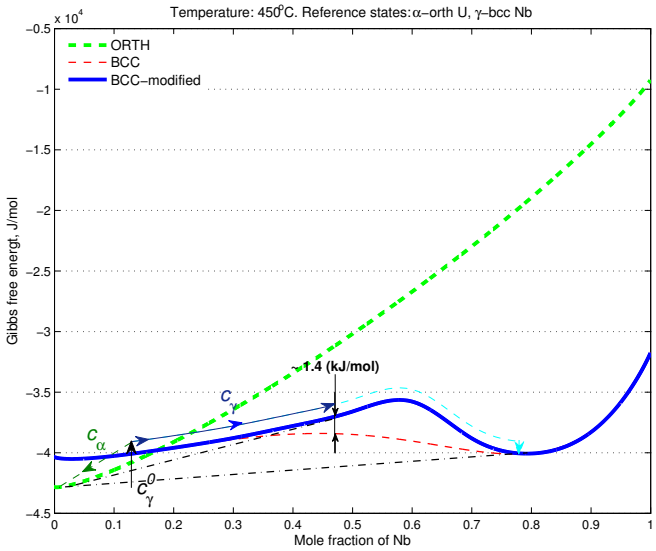

(a)

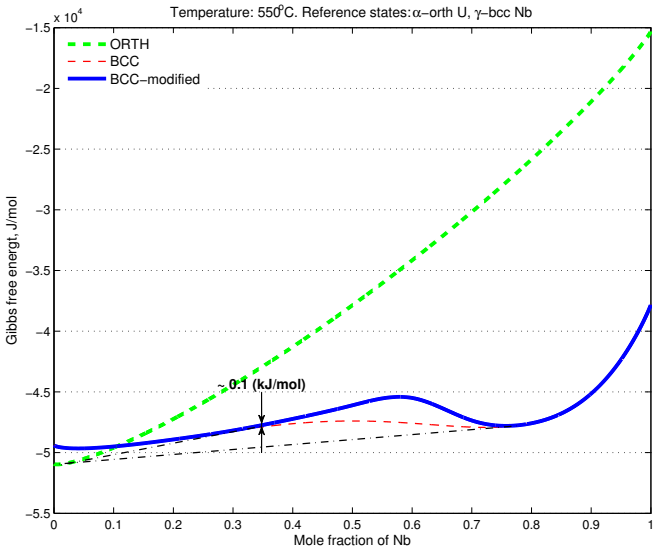

(b)

Figure 3.18: Proposed strain-adjusted free energies of α and γ at 450^0C (a) and 550^0C (b), plotted with reference to orth-U and bcc-Nb. Here, since additional strain energy was assumed to be insignificant in α, the phase's proposed free energies were chosen to be the same as CALPHAD free energies to simplify the effort. Notice that the proposed free energies form two common tangents with each other. These strain-adjusted free energies can be seen as the realization of Djuric's hypothetical free energies via CALPHAD methodology.

proposal [1]. For this, the piecewise cubic polynomial with ten knots was used. This polynomial first allowed the accurate fittings of the CALPHAD base energies then enabled the desired modifications on top of these bases by fine tuning the positions of appropriate knots. The resulting energies are illustrated at 450^0C and 550^0C in Fig. 3.18 (note that for quick LE estimations in this figure the conventional free-energy minimizer implemented in MATLAB was used). As illustrated in Fig. 3.18, the empirical estimations using piecewise cubic polynomials indicated that Djuric's hypothesis holds when the non-equilibrium energies around the lump of the bcc miscibility-gap is slightly or moderately increased. Since it is always the first impression that an increase in the total energy of a system is usually the result of strain/stress, these empirical findings lead us to the following considerations:

First, in the case of uranium-niobium's discontinuous monotectoid decomposition, due to the volume mismatch ($\sim 1\% - 15\%$) between α (20.8625 $\mathring{A}^3/Atom$ [161]) and γ (18.0988 (pure Nb) - 20.6464 (pure U) $\mathring{A}^3/Atom$ [This work]), there exists a stress/strain field around the interfacial region between the two phases. Due to the lamellae-type structure, this stress/strain field is distributed all over the lamellae where the discontinuous monotectoid decomposition happens, making its existence within the microstructure and effect on the decomposition non-ignorable. To best demonstrate this stress/strain field, a possible transformation path from bcc to orthorhombic structure is considered in Fig. 3.19. As shown in this figure, the transformation happens along the bct lattice of the bcc structure under a distortion and shuffle. Under this transformation, sufficient lattice mismatches would be introduced along the a_{orth} and c_{orth} axes while coherent-type mismatch exists along the b_{orth}, as demonstrated in Fig. 3.20. The lattice mismatch along a_{orth} and c_{orth} could result in misfit dislocations to reduce some of the internal stresses. Alternatively, it can also favor the growth of the precipitate for each step of, for instance, 4 or 5

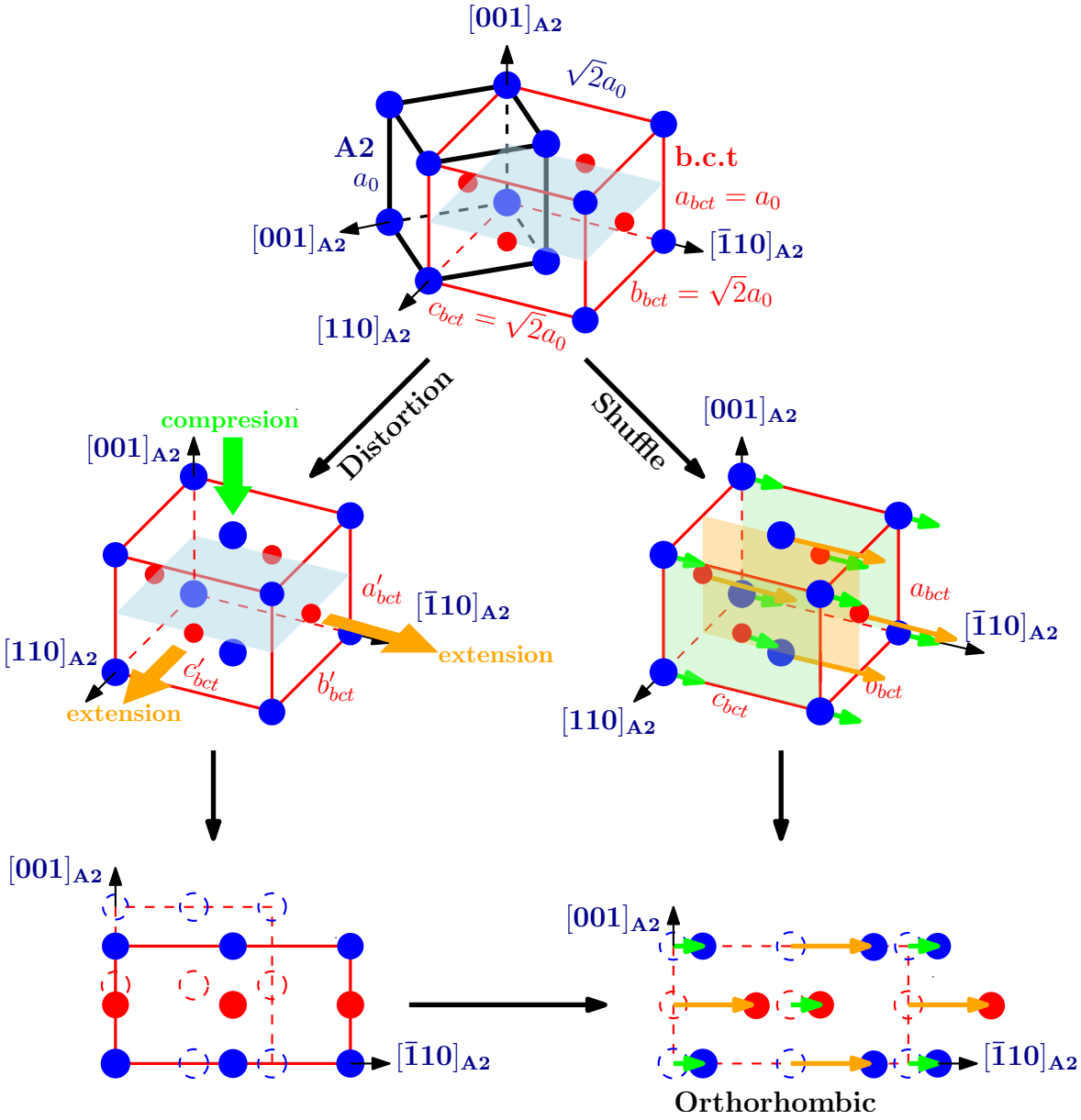

Figure 3.19: Schematic demonstration of the structural transformation from bcc to orth happened when the orth precipitate nucleate out of the bcc matrix.

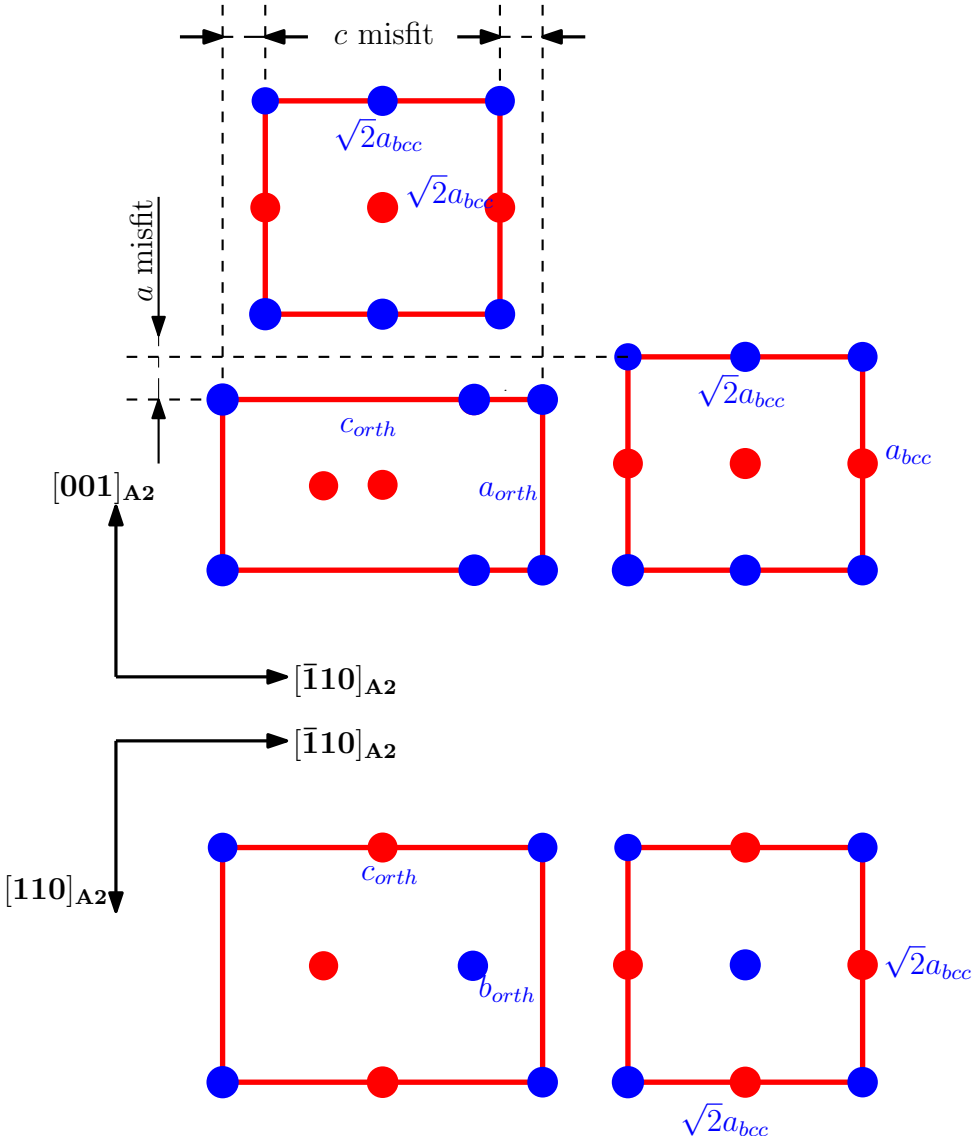

Figure 3.20: Lattice mismatches between the orthorhombic precipitate and bcc matrix along the a_{orth}, b_{orth}, and c_{orth} directions. Here, lattice mismatch along b_{orth} is relatively small while ones along the a_{orth} and c_{orth} are considerably large.

stacked orthorhombic unit cells along the a direction which tend to fit better with a stack of 3 or 4 bcc unit cells. In either case, internal strain around the interface between α and γ exist and raises in free energies of α and γ as the result of this strain should be expected.

Second, CALPHAD free energies are bulk free energies. Although the bulk energies can be used to describe interfacial thermodynamics of the reaction front between α and γ under ordinary conditions where interfacial effects, e.g. coherency, stress/strain, etc., are weak, they tend to be insufficient under special conditions where the interfacial effects are dominant. In such conditions, the additional energies arising from the interfacial effects must be explicitly taken into account. Here, since the strain energy arising from this stress/strain field tends to be smaller at higher temperature (due to thermal relaxation), it is more likely that the CALPHAD bulk energies can account for the interfacial effect of stress/strain under high temperature conditions, hence the observations of two LE within $605^0C - 647^0C$. In contrast, at lower temperature the strain energy becomes larger; it tends to deviate the system from ordinary thermodynamics, making the CALPHAD description of its complete effect less sufficient. This is especially true for the non-equilibrium part of the CALPHAD energies, i.e. the lump of the bcc miscibility gap, which was not directly verified with experimental equilibria like the equilibrium part of the CALPHAD energies but rather the extrapolating products of these equilibrium energies.

Combining the above considerations, it is concluded that the physical condition legitimating Djuric's hypothesis (the union of C into A) is stress/strain. This stress/strain is distributed along the $\alpha|\gamma$ lamellar structures and its non-trivial associated energy deviates the system out of the ordinary thermodynamics represented by CALPHAD at temperatures ranging from 400^0C to 605^0C. To account for the

effect of this stress/strain, we propose to use the above strain-adjusted free energies. These strain-adjusted free energies share a common advantage of soundly taking into account the possible effect of stress/strain while at the same time remaining completely consistent with other phase equilibria from CALPHAD estimations and experiments. It is however noted that for convenience these adjusted energies had been simplified. In particular, since α is considerably stiffer than γ, it is less likely to be deformed; therefore, we assume that α has no strain and assign all strain energy to γ. In addition, since the equilibrium part of γ's free energy was directly checked against experiments, it is believed that this part should have taken into account a considerable energetic contribution from the strain within its compositional region; hence, it does not need much attention. On the other hand, the non-equilibrium part of γ's free energy, located within the bcc miscibility gap, is just a product of the CALPHAD extrapolation of the equilibrium part; although it is expected that this part still carries some of the accountability for the strain effect from the equilibrium part via the extrapolation (therefore the observation of two LE within $605^0C - 647^0C$), it may still not sufficiently capture the effect of the strain which becomes stronger at lower temperature. In reality, the strain-adjusted free energies of both α and γ should be changing over the entire compositional domains of the two phases, but might not be much different from the current simplified ones.

3.4.3 Quantification of Djuric's hypothesis

One practical problem with the above strain-adjusted free energies is that they are rather discontinuous, i.e. different adjusted energies at different temperatures have to be described by different piecewise cubic polynomials. This is somewhat inconvenient and insufficient since one will have to repeat the above empirical evaluation every times a new energy is needed. The goal is to generate a general de-

scription for the strain-adjusted free energies, which provides a complete freedom to predict any energetic value within the interval of interest. Such predictive capability is especially essential for future implementations of phase-field simulations to investigate the lamellar growths of the discontinuous monotectoid decomposition or other microstructure evolutions or phase transitions in the uranium-niobium alloys. Naturally, CALPHAD's subregular solution model (Eq. 2.35) appeared as the first choice for the description. It was however found that this model cannot well describe the proposed strain-adjusted free energies shown in Fig. 3.18. The reason is that the *n-order* polynomials used in this model are not mathematically sufficient to capture the high nonlinearity of these curves. Here, we proposed a modification of this model, focusing on the improvement of function-approximation capability:

First, let us consider a nonlinear temperature extension of interaction parameter:

$$\Omega^{\nu}_{Nb,U} = a_{\nu} + b_{\nu}T + c_{\nu}T\ln T + d_{\nu}T^2 \tag{3.4}$$

Substitute Eq. 3.4 into Eq. 2.39 and taking temperature out yields:

$$\begin{aligned} G_{Nb,U:Vac} \;=\; & x_{Nb}G^0_{Nb} + (1-x_{Nb})G^0_U + \\ & + RT\left(x_{Nb}\ln x_{Nb} + (1-x_{Nb})\ln(1-x_{Nb})\right) + \\ & + A(x_{Nb}) + B(x_{Nb})T + C(x_{Nb})T\ln(T) + \\ & + D(x_{Nb})T^2 \end{aligned} \tag{3.5}$$

where, $A(x_{Nb})$, $B(x_{Nb})$, $C(x_{Nb})$, and $D(x_{Nb})$ are $(n+2)^{th}$-*order* polynomials:

$$A(x_{Nb}) = x_{Nb}(1-x_{Nb})\sum_{\nu=0}^{n} a_\nu (2x_{Nb}-1)^\nu \quad (3.6)$$

$$B(x_{Nb}) = x_{Nb}(1-x_{Nb})\sum_{\nu=0}^{n} b_\nu (2x_{Nb}-1)^\nu \quad (3.7)$$

$$C(x_{Nb}) = x_{Nb}(1-x_{Nb})\sum_{\nu=0}^{n} c_\nu (2x_{Nb}-1)^\nu \quad (3.8)$$

$$D(x_{Nb}) = x_{Nb}(1-x_{Nb})\sum_{\nu=0}^{n} d_\nu (2x_{Nb}-1)^\nu \quad (3.9)$$

From the mathematical point of view, *n-order* polynomial is a convenient tool for modeling simple systems, however it is not always effective when dealing with complex systems. Here, to capture the highly non-linear strain-adjusted free energies, we proposed to substitute the $(n+2)^{th}$-*order* polynomials by piecewise cubic splines. In particular, instead of using a single function to model the whole energy curve, we divided the curve into different intervals and described each interval with one particular function. At the interception between two intervals, the functions are smoothly connected (up to 2^{nd} derivative for cubic spline). The mathematical description of this modification was given as follows:

$$\begin{aligned} G_{i_{Nb,U:Vac}} = {} & x_{Nb}G^0_{Nb} + (1-x_{Nb})G^0_U + \\ & + RT\left(x_{Nb}\ln x_{Nb} + (1-x_{Nb})\ln(1-x_{Nb})\right) + \\ & + A_i(x_{Nb}) + B_i(x_{Nb})T + C_i(x_{Nb})T\ln(T) + \\ & + D_i(x_{Nb})T^2, \text{ for } x_{Nb} \in [x^i_{Nb}, x^{i+1}_{Nb}] \end{aligned} \quad (3.10)$$

where, i is the interval index of which value runs from 1 to 10 ($i = 1$ corresponds to

$x \in [0, 0.1]$; $i = 2$ corresponds to $x \in [0.1, 0.2]$; etc.), and $A_i(x)$, $B_i(x)$, $C_i(x)$, and $D_i(x)$ are the piecewise cubic splines:

$$\begin{aligned}
A_i(x_{Nb}) &= a_{i,0} + a_{i,1}(x_{Nb} - x^i_{Nb}) + a_{i,2}(x_{Nb} - x^i_{Nb})^2 + \\
&\quad + a_{i,3}(x_{Nb} - x^i_{Nb})^3, \text{ for } x_{Nb} \in [x^i_{Nb}, x^{i+1}_{Nb}] \qquad (3.11)\\
B_i(x_{Nb}) &= b_{i,0} + b_{i,1}(x_{Nb} - x^i_{Nb}) + b_{i,2}(x_{Nb} - x^i_{Nb})^2 + \\
&\quad + b_{i,3}(x_{Nb} - x^i_{Nb})^3, \text{ for } x_{Nb} \in [x^i_{Nb}, x^{i+1}_{Nb}] \qquad (3.12)\\
C_i(x_{Nb}) &= c_{i,0} + c_{i,1}(x_{Nb} - x^i_{Nb}) + c_{i,2}(x_{Nb} - x^i_{Nb})^2 + \\
&\quad + c_{i,3}(x_{Nb} - x^i_{Nb})^3, \text{ for } x_{Nb} \in [x^i_{Nb}, x^{i+1}_{Nb}] \qquad (3.13)\\
D_i(x_{Nb}) &= d_{i,0} + d_{i,1}(x_{Nb} - x^i_{Nb}) + d_{i,2}(x_{Nb} - x^i_{Nb})^2 + \\
&\quad + d_{i,3}(x_{Nb} - x^i_{Nb})^3, \text{ for } x_{Nb} \in [x^i_{Nb}, x^{i+1}_{Nb}] \qquad (3.14)
\end{aligned}$$

in which, $a_{i,j}$, $b_{i,j}$, $c_{i,j}$, and $d_{i,j}$ (i=1:10, j=0:3) are the parameters that need to be optimized/fitted.

Intuitively, this 'divide-and-conquer' approach is more efficient in term of function-approximation capability. It has been proven in the present work that this modified model can capture the proposed strain-adjusted free energies very well. Here, we considered ten equal intervals and fitted the model's parameters to the strain-adjusted free energies proposed at 450^0C, 500^0C, 550^0C and 600^0C as well as the CALPHAD free energy at the monotectoid isotherm (647^0C, since at and above the monotectoid isotherm, strain effect was assumed to be trivial and interfacial thermodynamics converges to bulk thermodynamics). The fitted parameters are reported in Table 3.6. It is noted that the modified CALPHAD model with its parameters has been tested within the temperature range of current interest, i.e., from 400^0C to

Table 3.6: Fitted parameters of the modified CALPHAD model

i	$a_{i,0}$	$a_{i,1}$	$a_{i,2}$	$a_{i,3}$	$b_{i,0}$	$b_{i,1}$	$b_{i,2}$	$b_{i,3}$
1	4855354	-2861327	432519.9	-1010.99	-74217.1	46621.42	-6860.67	18.1987
2	4855354	-1404866	5943.184	18483.02	-74217.1	24358.51	236.6101	-275.874
3	14719509	51739.75	-129369	9884.032	-275640	2093.379	2881.799	-82.8449
4	21094219	4467592	322563.7	12183.99	-371923	-80598.5	-4968.72	-49.3709
5	-71225699	10795858	1848909	110210.5	1253360	-192175	-32246.1	-1724.15
6	-68518197	-10571851	1871309	331834.3	1189689	183832.6	-33080.4	-5617.15
7	213274245	-31127311	-2298607	344728.5	-3704181	540739.4	39376.83	-5897.18
8	-128918818	32854963	-2125842	16868.97	2241427	-570515	36399.29	-256.279
9	14040090	-5820683	577586.5	3915.623	-235628	101913.2	-10460.9	-80.0717
10	14040090	-1608656	-165347	17507.54	-235628	31224.93	2852.946	-342.654
	$c_{i,0}$	$c_{i,1}$	$c_{i,2}$	$c_{i,3}$	$d_{i,0}$	$d_{i,1}$	$d_{i,2}$	$d_{i,3}$
1	-5.95519	4.185259	-0.6457	0.001862	10907.84	-6943.64	1024.979	-2.75678
2	-5.95519	2.398882	0.012651	-0.02681	10907.84	-3671.62	-36.441	41.2129
3	-29.8181	0.612326	0.313772	-0.00751	42062.07	-399.266	-443.529	11.76045
4	-36.5953	-8.33309	-0.45831	0.000171	56068.61	12219.35	738.4793	5.476907
5	122.0804	-19.3117	-3.22278	-0.16559	-188778	29039.94	4864.408	257.587
6	127.7052	17.31244	-3.42271	-0.5589	-180630	-27593.4	5009.066	845.6495
7	-375.469	55.62401	3.870939	-0.60034	559460.6	-81782.4	-5928.51	889.9922
8	222.3259	-57.0167	3.731668	-0.03248	-337849	86055.73	-5501.18	38.777
9	-22.2192	9.681064	-1.0019	-0.00715	35346.03	-15298.8	1574.507	11.3674
10	-22.2192	3.015317	0.267741	-0.03275	35346.03	-4695.01	-424.876	51.17595

647^0C, and the results were acceptable; yet, inefficiency should still be expected since accurate manual assessment of proposed strain-adjusted free energies is non-trivial. Generalization of the model's predictability for a better performance and more comprehensive temperature domain is possible but requires additional thermodynamic data and meticulous efforts, e.g., reliable experimental intermediate compositions of γ_{1-2} as well as more careful and sophisticated evaluations of the strain-adjusted free energies of interest.

The estimated temperature- and composition-dependent strain energies are reported in Fig. 3.21. As indicated in this figure, these energies can be feasibly fitted by $4th - order$ polynomials which are usually acceptable characterizations for the dependencies of strain energy on composition and temperature. Indeed, within the context of classical mechanics, strain energy can be written as follows:

$$U_{str} = \frac{1}{2} V_M(x,T) E(x,T) \epsilon^2(x,T)$$

where, for the strain energy of interest, x is the intermediate concentration of γ_{1-2} and is paired with its correspondent temperature T, V_M is molar volume, E is Young's modulus, and ϵ is strain induced by V_M mismatch. It has been shown in practice [162, 163, 164, 165, 166, 167] that V_M and subsequently E and ϵ, which are closely related to V_M, can be reasonably approximated by a linear function of temperature. In addition, it can be derived from Fig. 3.1 and [4] that Vegard's law [168] tends to hold for V and hence intuitively for E and ϵ as well, which also makes these quantities also approximately linear functions of composition. Consequently, the strain energy of interest is roughly a $4th - order$ function of the paired intensive properties:

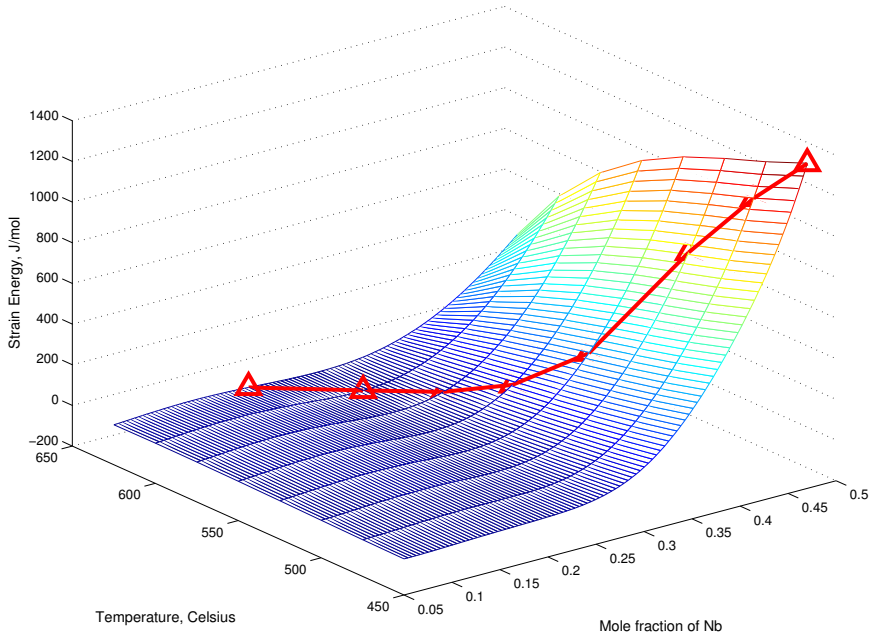

(a)

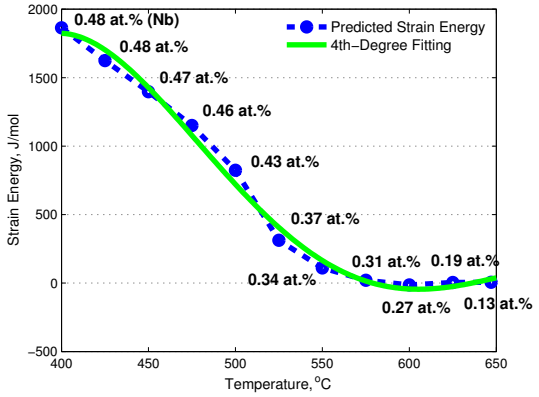

(b)

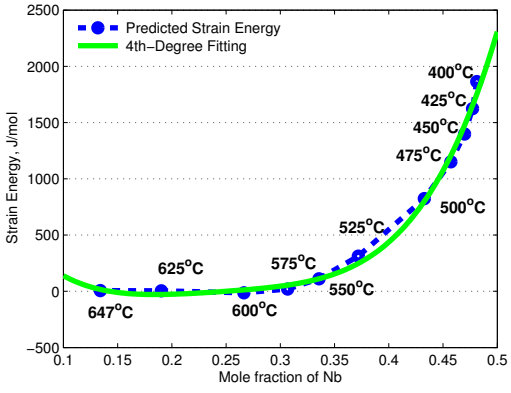

(c)

Figure 3.21: Predicted additional strain energies as a function of temperature and composition. Solid line (red color) in (a) indicates strain energy at the intermediate composition of γ_{1-2} (estimated with the strain-adjusted free energies). Its projection on the energy-temperature and energy-composition plane are shown in (b) and (c), respectively. Note that the isothermal and isocomposition strain energies are also reasonably fitted by $4^{th} - order$ polynomials.

$$U_{str} \approx u_0(x^4) + u_1(x^4)T + u_2(x^4)T^2 + u_3(x^4)T^3 + u_4(x^4)T^4 \qquad (3.15)$$

Therefore, phenomenological agreement between the empirical corrections of the strain energy and the functional form of $4^{th} - order$ tends to verify, to some extent, the physical eligibility of the proposed strain-adjusted free energies (note that the isothermal and isocomposition strain energies, shown in Fig. 3.21, can also be reasonably fitted by $4^{th} - order$ polynomials).

3.4.4 On the significance and shortcoming of Djuric's hypothesis

The significance of Djuric's hypothesis on the origin of the discontinuous reactions in uranium-niobium system is that it firstly legitimates the occurrence and sustainment of the metastable γ_{1-2} during the monotectoid decomposition which is an important condition for the occurrence of DP and secondly explains the compositional adjustment of DC in a straightforward manner. To best illustrate this, phase-field diffusion-couple simulations were repeated for the case of 450^0C and 550^0C using the proposed strain-adjusted free energies. It is noted that the diffusion couples here are not meant to be the tool for LE investigation like above but rather the simulations of uranium-niobium's monotectoid decomposition. In this regard, the final converged state of the diffusion-couple simulations manifest the product phase that would be expected from the decomposition of the system. The simulation results are shown in Fig. 3.22. As can be seen from this figure, the monotectoid decomposition is indeed discontinuous at the intermediate state with the metastable product of $\alpha + \gamma_{1-2}$ instead of progressing all the way to the final product of $\alpha + \gamma_2$ as in the above phase-field simulations using the CALPHAD free energies. Within the phase-field framework, the simulated monotectoid decomposition happens for each case of tem-

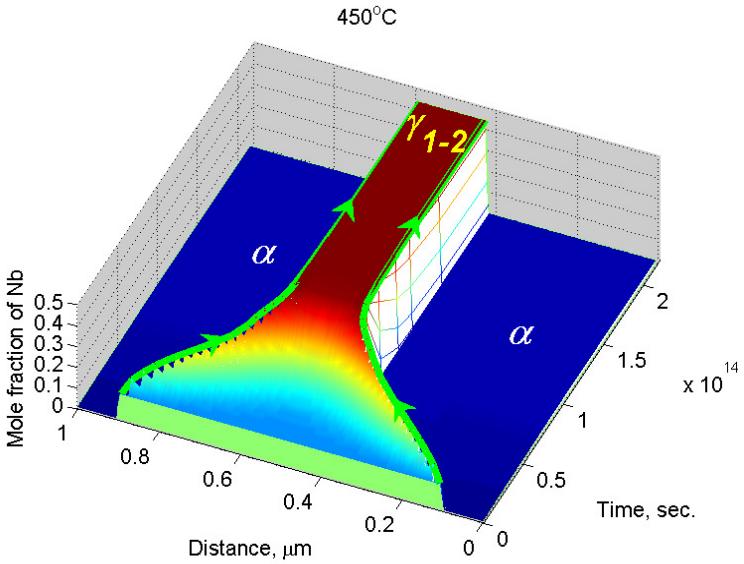

(a)

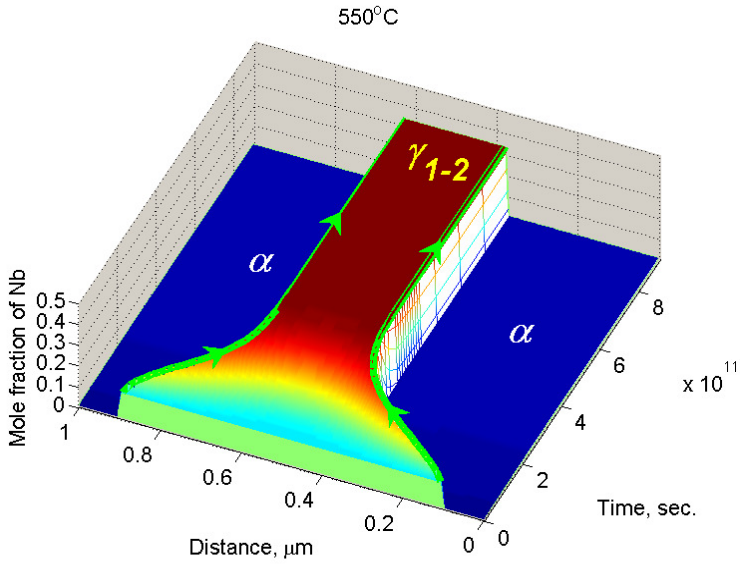

(b)

Figure 3.22: Phase-field simulation at 450^0C and 550^0C using the strain-adjusted free energies to feature the significant of Djuric's hypothesis in explaining the occurrence and sustainment of γ_{1-2}. Here, it is noted that after some time the system converge to the state at which α and γ_{1-2} lamellae coexist.

perature as follows. At the early stage of the reaction, γ_1 starts transforming to α. This is due to the fact that γ_1 is energetically less stable than α. The consequence of this phase transformation is that the Nb content inside the γ precipitate increases steadily. This happens first at the $\alpha|\gamma$ interface, i.e. c_γ^{int}, then gradually propagates into the γ precipitate via long-range diffusion, leading to a gradient distribution of Nb across the γ precipitate during the phase transformation. When c_γ^{int} reaches its LE value which happens to be γ_{1-2} in these study cases, due to the two-fold obstacle introduced by this LE, as aforementioned, the phase transformation tends to stop with minimal thermodynamic driving force. At this moment, if the gradient distribution exists across γ, it will decrease c_γ^{int} to balance out the Nb distribution across the γ precipitate and hence prevent c_γ^{int} from reaching its LE value of γ_{1-2} and allow the phase transformation to continue. When the distribution of Nb across γ is homogeneous with the value of γ_{1-2}, as happens in Fig. 3.22 after 1×10^{14} s and 2×10^{11} s for the cases of 450^0C and 550^0C respectively (again slow evolution time is due to the slow bulk diffusivities of α and γ), the Nb concentration within α also reaches its stable value throughout the phase and the monotectoid decomposition is completed. The featured phase product in this case is the mixture of α and metastable γ_{1-2} which is the special characteristic of DP.

Following the above simulations, 0.01 μm of near equilibrium U - 75 $at.\%$ Nb are nucleated inside the resulting metastable γ_{1-2} phase. These simulation setups are meant to investigate Djuric's assumption on the occurrence of DC, which states that upon the nucleation of γ_2 inside the system, the intermediate product of $\alpha + \gamma_{1-2}$ will continue to transform into the final stable product of $\alpha + \gamma_2$. For convenience, U - 75 $at.\%$ Nb is not differentiated from γ_2 since the near-equilibrium phase will quickly transform into the stable form at early reaction. The simulation results are reported in Fig. 3.23. As can be seen from this figure, the system's transformation

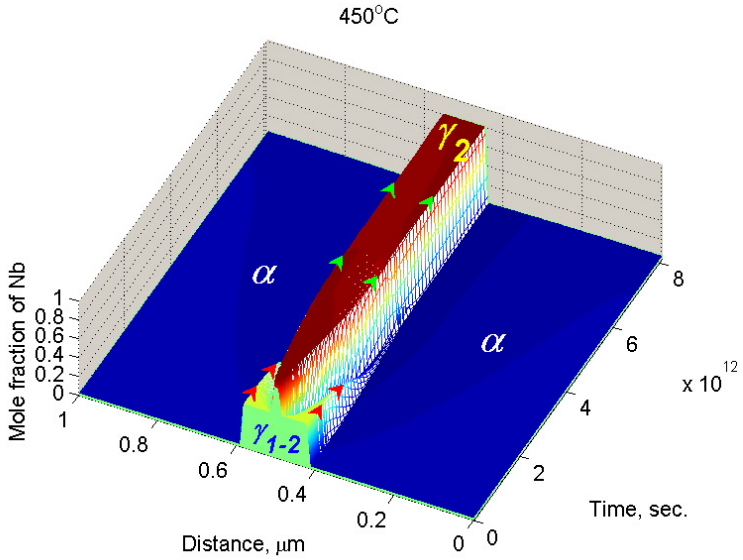

(a)

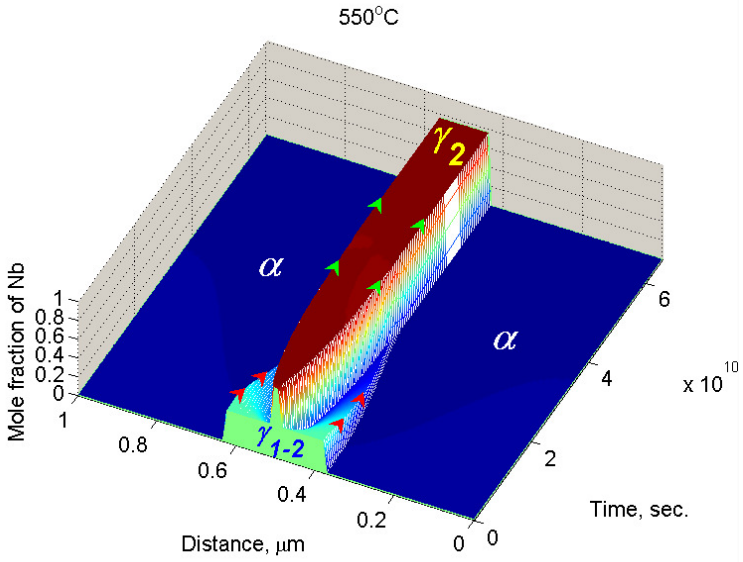

(b)

Figure 3.23: Phase-field simulation at 450^0C and 550^0C using the strain-adjusted free energies to feature the significant of Djuric's hypothesis in explaining the compositional adjustment of DC. Note here that $\alpha + \gamma_{1-2}$ continues to transform to $\alpha + \gamma_2$ when γ_2 nucleates inside the system, in consistent with experiments.

indeed continues with the appearance of γ_2-precipitate in the following manner. At the beginning, the new γ_2 reacts with γ_{1-2} at $\gamma_{1-2}|\gamma_2$ interface. Since, γ_2 is thermodynamically more stable than γ_{1-2}, it consumes the metastable phase. The growth of γ_2 into γ_{1-2} reduces the Nb content throughout the γ_{1-2} precipitate by means of long-range diffusion starting at the $\gamma_{1-2}|\gamma_2$ interface. This reduction, when propagating to $\alpha|\gamma_{1-2}$ interface, disturbs the metastable state at this region. Consequently, γ_{1-2} starts reacting again with α, trying to gain back local equilibrium. The reaction between α and γ_{1-2} tends to increase Nb content in γ_{1-2} region, competing with the opposite trend happening at the $\gamma_{1-2}|\gamma_2$ interface. Since the reaction at the second interface has a higher driving force than that at the first interface, the Nb-content throughout the γ_{1-2} phase region depletes faster than it can gain back. Consequently, γ_{1-2} ends up transforming completely into α and γ_2, featuring the characteristic compositional adjustment of DC.

Here, it is noted that even though the above demonstrated occurrence and sustainment of γ_{1-2} as well as the compositional adjustment from γ_{1-2} to γ_2 are two important conditions for the occurrences of DP and DC in the uranium-niobium system respectively, they alone are not sufficient to make the discontinuous reactions. Here, the missing condition is the lamellar-type structures by which DP and DC are characterized as the so-called cellular reactions [19, 32]. While Djuric's hypothesis can best explain the first two conditions, as demonstrated by the above phase-field simulations, it does not necessarily result in the proper microstructures. This is indeed true and can be shown by mean of 2-D phase-field simulations. In the following, the simulation of microstructural evolution of DP is carried out at 450^0C. It is noted that in order to have a better focus we narrow our discussion down to only DP, which is generally the discontinuous reaction of more interest. The designated simulation makes use of the proposed strain-adjusted free energies to feature Djuric's hypoth-

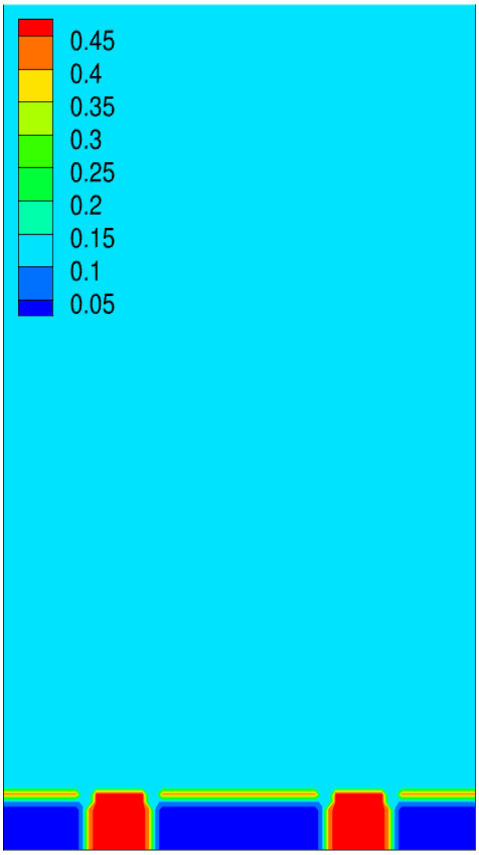

Figure 3.24: Initial configuration of the simulation box with size of 162×108 nm and four precipitates with compositions follow the equilibrium partition of α and γ (note that color indicates the mole fraction of Nb; as such red regions are γ_{1-2} precipitates, blue regions are α precipitates, and light blue region is γ_1 matrix).

esis. In addition, it is put under the assumption that the DP reaction is a volume diffusion controlled process. The volume-diffusion-controlled assumption is one possible for DP [169] and found to benefit the reaction with a faster interfacial velocity [170]. Under this kinetic assumption, the diffusivities at the interfaces are chosen to be equal to the bulk diffusivities, which are taken from the DICTRA assessment. The simulation domain is 162×108 nm in size which reflects physical length scale of the system as measured in [31]. It initially consists of two α precipitates and two γ precipitates whose compositions and sizes follows the LE partition, as shown in Fig. 3.24.

The simulation result is shown in Fig. 3.25. As can be seen from this figure, the initially nucleated α precipitates eventually impinge and coalesce while the γ_{1-2} precipitates fades out. The reason for this is that at the interface between the γ_1 matrix and γ_{1-2} lamellae there occurs a down-hill diffusion between the two bcc phases, i.e. a Nb flux flows from γ_{1-2} to γ_1. This flux (vertical flux) dissipates a considerably large amount of Nb content out of the γ_{1-2} lamellae. Note that relative to this flux, there exists another flux (lateral flux) that flows along the tips of the α lamellae (due to the curvatures/gradients of these lamellae along the reaction front) and, in the opposite way, adds more Nb content to the γ_{1-2} lamellae to grow them. Unfortunately, in this case the later lateral flux is slower than the vertical flux and not able to sustain the Nb content within the γ lamellae near its LE value. This essentially breaks down the equilibrium between the α and γ_{1-2} lamellae, allowing the α lamellae to expand into the γ_{1-2} lamellae until impingement. The evolving system therefore does not exhibit the discontinuous reaction, and in this case Djuric's hypothesis falls short as being the only necessary and sufficient condition for the origin of the discontinuous reaction in the uranium-niobium system.

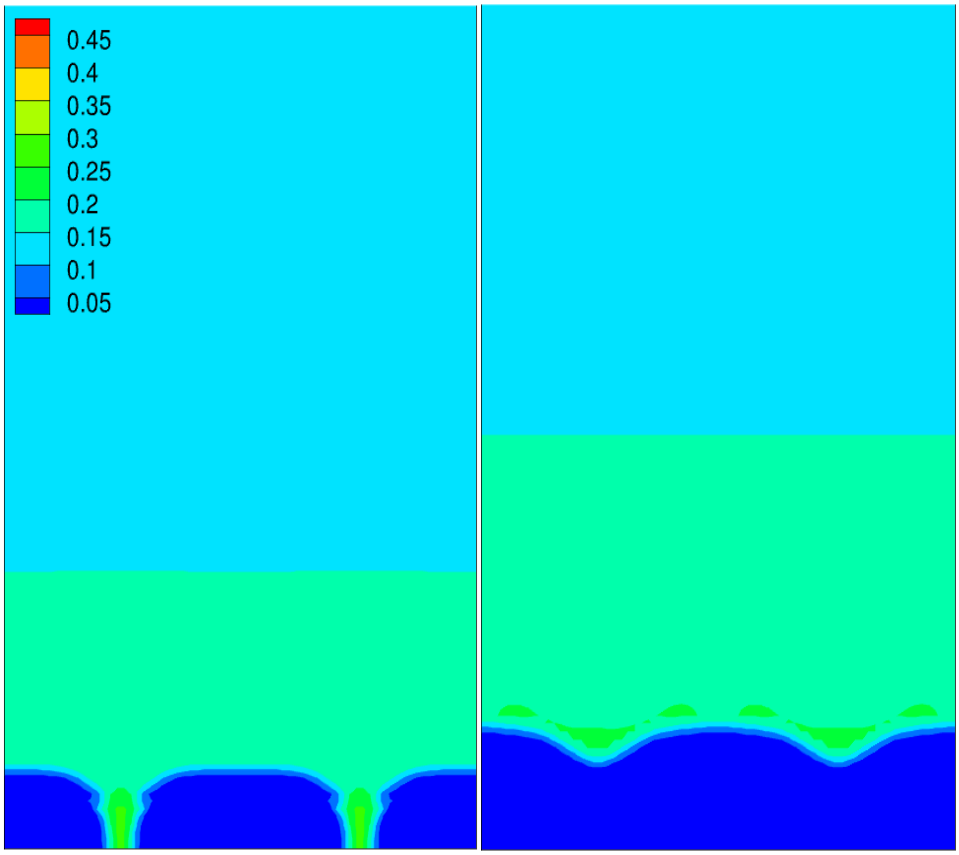

(a) (b)

Figure 3.25: Phase-field simulation at 450^0C without fast boundary diffusion resulting in lamellar coalescence (note that color indicates the mole fraction of Nb).

3.4.5 The role of diffusion mechanism on the growth of DP's lamellae under Djuric's hypothesis

As is commonly known, while thermodynamics decides which are the stable and metastable phases co-existing inside a system, it is the kinetics that usually determines the morphologies of microstructures of those phases. This tends to be true in the case of the uranium-niobium system and has been demonstrated above by mean of phase-field simulations. In the following, the non-trivial role of kinetics on the occurrence of DP under Djuric's thermodynamic hypothesis is further investigated. Particularly, the above 2-D phase-field simulation was repeated with the assumption that DP is a boundary-diffuse-controlled process. This is usually the more common assumption for DP than the volume-diffuse-controlled assumption [19, 32]. Under the boundary-diffuse-controlled assumption, the interfacial diffusivities, especially ones along the reaction front (or moving grain boundary [19, 32]) of DP were taken to be significantly larger than bulk diffusivities. Again, the bulk diffusivities are taken from the DICTRA assessment, the interfacial diffusivities at the reaction front/grain boundary are derived from the experimental interphase boundary diffusivity triple product $sD\delta$ [31], where s is the segregation factor at the interface, D is the needed diffusivity, and $\delta = 1$ (A) is interfacial width, and the interfacial diffusivities at the $\alpha|\gamma_{1-2}$ interface are chosen to be 10^3 times smaller than those at the reaction front.

Simulation result is reported in Fig. 3.26. Here, in contrast to the previous case, when the fast grain-boundary condition was taken into account, the Nb-flux flowing into the γ_{1-2} lamellae from the tips of the α lamellae is much more significant than the Nb-flux flowing out of the γ lamellae due to the down-hill diffusion. In other words, there is not much Nb leakage from the γ lamellae and its LE state with the α lamellae is sustained during the reaction. Analysis of driving force at the

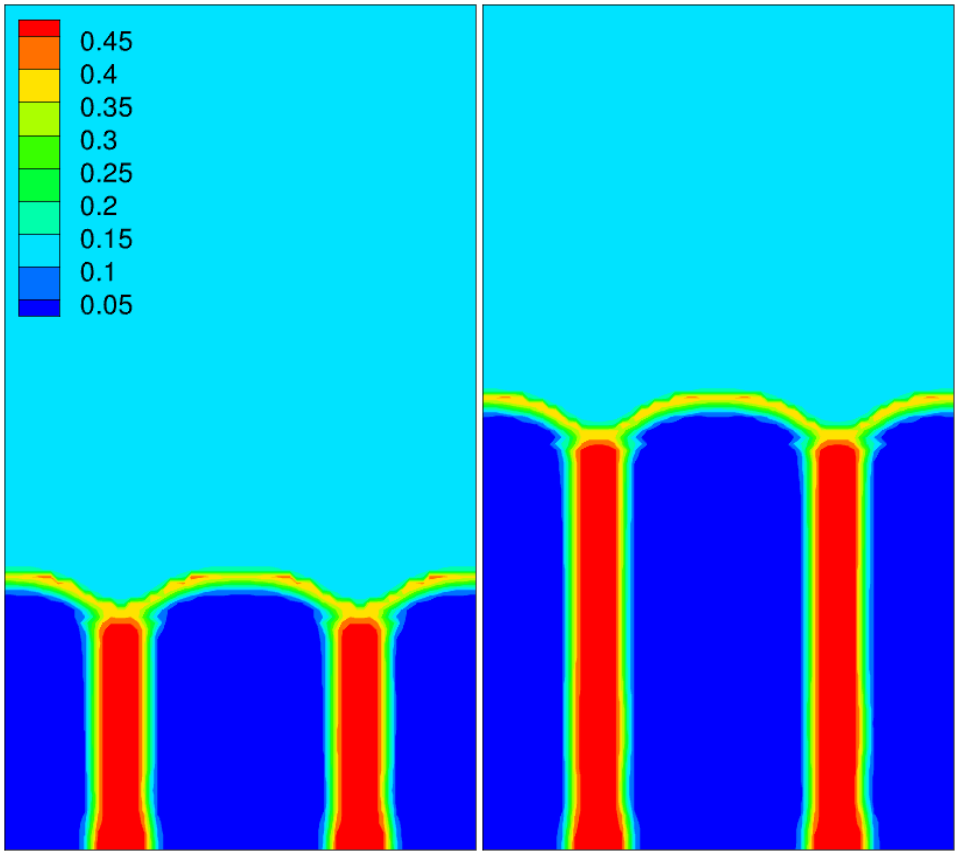

(a) (b)

Figure 3.26: Phase-field simulation 450^0C with fast boundary diffusion resulting in stable lamellar growth (note that color indicates the mole fraction of Nb; as such red regions are γ_{1-2} precipitates, blue regions are α precipitates, and light blue region is γ_1 matrix).

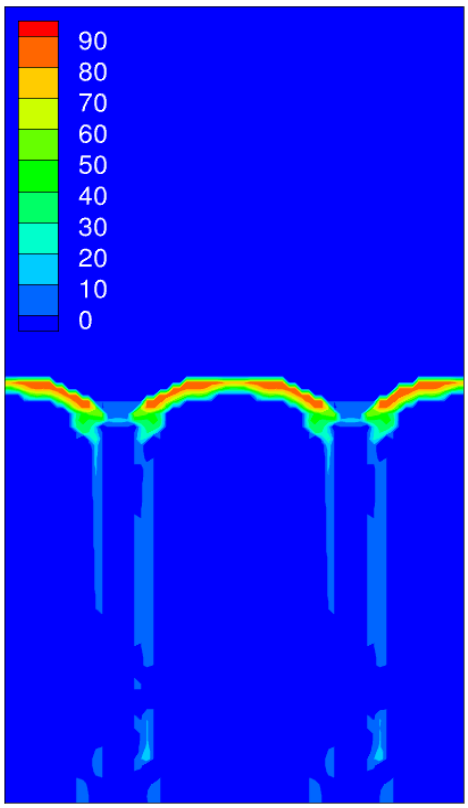

Figure 3.27: Chemical driving forces at different interfaces between α and γ at 450^0C under Djuric's hypothesis. Note that unit of chemical driving forces is J/cm^3 and positions of precipitates and matrix correspond to those in Fig. 3.26 (b).

interfaces shown in Fig. 3.27 demonstrates this. In this figure, it is also interestingly observed that the driving force distributed at the $\gamma_{1-2}|\gamma_1$ interface is considerably smaller than that at the $\alpha|\gamma_1$ interface. The existence of this driving force during down-hill diffusion is found to be in good agreement with Hillert's theory on the driving force of DP [171, 172] in which he stated that: "*the driving free energy for the growth of the new α grain is identified with some fraction of the free energy which would be lost due to volume diffusion if certain mechanisms did not interfere.*" In our case, there is such interfering mechanisms and hence the driving force is relatively non-trivial for the growth of DP (note that Hillert α grain is equivalent to the γ_{1-2} lamellae). Yet, the $\gamma|\gamma$ interface is still effectively carried by the growth of α precipitate and DP still occurs, as can be seen from the figure. The result is therefore the stable growth of $\alpha|\gamma_{1-2}$ lamellae, which showcases the sufficient role of kinetics, i.e. fast grain-boundary diffusion, under Djuric's hypothesis on the origin of DP in the uranium-niobium system.

From the above observations, while it is reasonable at this moment to conclude that (1) Djuric's hypothesis is possible when the effect of internal strain on the thermodynamics of the reaction is considered and that (2) this thermodynamic hypothesis can indeed result in the stable lamellar growth of DP given an appropriate kinetic condition (i.e. DP is a boundary-diffusion-controlled process), we are curious to see if the optimal interlamellar spacing of DP, a very common interest that most researches on DP seeks to address, could be explained by satisfying of all these thermodynamic and kinetic conditions? If it was possible to show this, it would further strengthen the above conclusion. As such, we carry out, in the following, phase-field simulations at 450^0C using different interlamellar spacing which includes 27 nm, 40.5 nm, 54 nm, 63 nm, and 81 nm (note that experimental spacing is around 55 nm [173]).

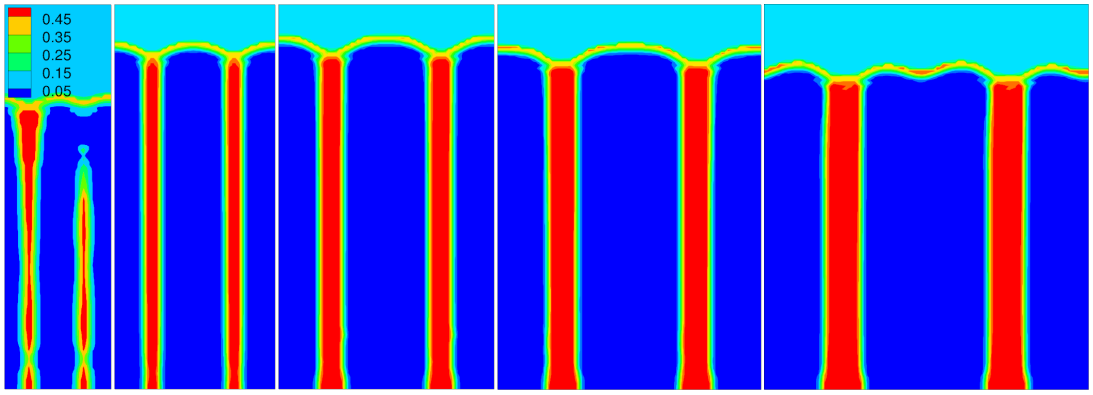

(a) $27nm$ (b) $40.5nm$ (c) $54nm$ (d) $66nm$ (e) $81nm$

Figure 3.28: 2D phase-field simulations at 450^0C with different interlamellar spacings (note that color indicates the mole fraction of Nb; as such red regions are γ_{1-2} precipitates, blue regions are α precipitates, and light blue region is γ_1 matrix).

Simulation results are shown in Fig. 3.28. As can be seen from this figure, among the considered interlamellar spacing, 54 nm yields the fastest discontinuous-precipitation growth. The calculated interfacial velocity in this case is 5.28×10^{-11} m/s, which is in good agreement with the experimental value of 5.2×10^{-11} m/s [31] for the interlamellar spacing of ~ 55 nm [173]. Note that when the interlamellar spacing deviates from 54 nm, the lamellar growth of uranium-niobium's discontinuous precipitation becomes slower, which is in agreement with the previous generic phase-field study of DP [170]. Interestingly, in the case of 27 nm, the lamellae start to pinch off and coalesce after some initial growth. This results in both larger lamellar size and interlamellar spacing, which are close to the 54 nm. Even so, the resulting curvature and hence surface tension at the tip of the precipitates is not essentially that of the favorable 54 nm. Consequently, the interfacial velocity is still smaller than those with initial interlamellar spacing close to 54 nm. Note that lamellar coalescence during growth is a common feature in the cellular-type reaction as it has

been often reported in literature (e.g. [170, 174, 175, 176]). Such a coalescence can sometimes result in the termination of the lamellar growth and subsequently lead to the development of heterogeneous colonies, as opposed to the current observation. In contrast to the lamellar coalescence which is seen in the case of small interlamellar spacing, in the case when the spacing is large, the simulation result shows that the lamellae tend to split into smaller branches (refer to Fig. 3.28). Interestingly enough, such branching also tends to allow the lamellae to readjust their size and spacing to 54 nm. Nevertheless, unless the branching occurs to its completion, the surface tension at the tip of the precipitates is still not that of the ideal one, and hence have slower interfacial velocity as compared to those with initial interlamellar spacings close to 54 nm. Based on these observations, the optimal spacing of uranium-niobium's DP, in this case, appears to follow the principles of maximum growth velocity which happens as a natural selection process and can be intuitively understood as follows. Given that the α precipitates were initially nucleated with different inter-precipitate spacing along the $\gamma|\gamma$ grain boundary, during the cellular reaction, some precipitates will grow faster than the others. As they expand out in all directions during growth, the faster precipitates will gradually invade the area in front of the slower precipitates and essentially block these precipitates from further growing. In this way, the fastest precipitates will eventually become dominant and hence specify the interlamellar spacing of the cellular reaction. And, with this interesting explanation for the optimal interlamellar spacing and the ability to quantitatively match the calculation with experiment, the postponed conclusion should now be safely made.

3.5 Phase-field investigation of the on-the-fly kinetic hypothesis

The beauty of ICMSE is that it is very versatile in the sense that different fundamental models can be put together and linked by empirical relationships in order to assess various aspects of materials. Even with a single integrated framework, so long as its modeling capability can still match our rich imagination and curiosity, there still exists an interesting degree of freedom for exploration. In this regard, it is interesting to think that if we could prove Djuric's hypothesis with the aid of ICMSE, with the aid of ICMSE we could also confront it. As such, we did not find it bothersome to split our effort to prove that Djuric's hypothesis is not strictly essential while at the same time favor the hypothesis during our phase-field investigations of the role of kinetics on the growth of DP's lamellae, which text presented above. The goal is to challenge the fundamental significance of Djuric's hypothesis, i.e. the intermediate LE that thermodynamically 'stabilizes' the metastable γ_{1-2} phase and hence establishes the necessary condition for DP. The initial idea is to prove that kinetics can also sustain the metastable phase and on top of this it can lead to the stable growth of DP's lamellae. Its source is a little imagination which schemes that if the reaction happened fast enough, it would not leave much time for the composition within the γ lamellae to reach γ_2, the system's only LE, during its active time at the reaction front with fast diffusion and therefore becomes frozen at an intermediate γ_{1-2} state due to sluggish bulk diffusion after the reaction front passes through. The solution of phase-field evolution equations exists and is reported in Fig. 3.29.

For this solution, the interfacial mobility and permeability are chosen to be considerably larger than those of the previous simulations. They both are scaled up by increasing the atomic mobility using our empirical relationship for the interfacial mobility and Steinbach's relationship [36] for the permeability. The interfacial mo-

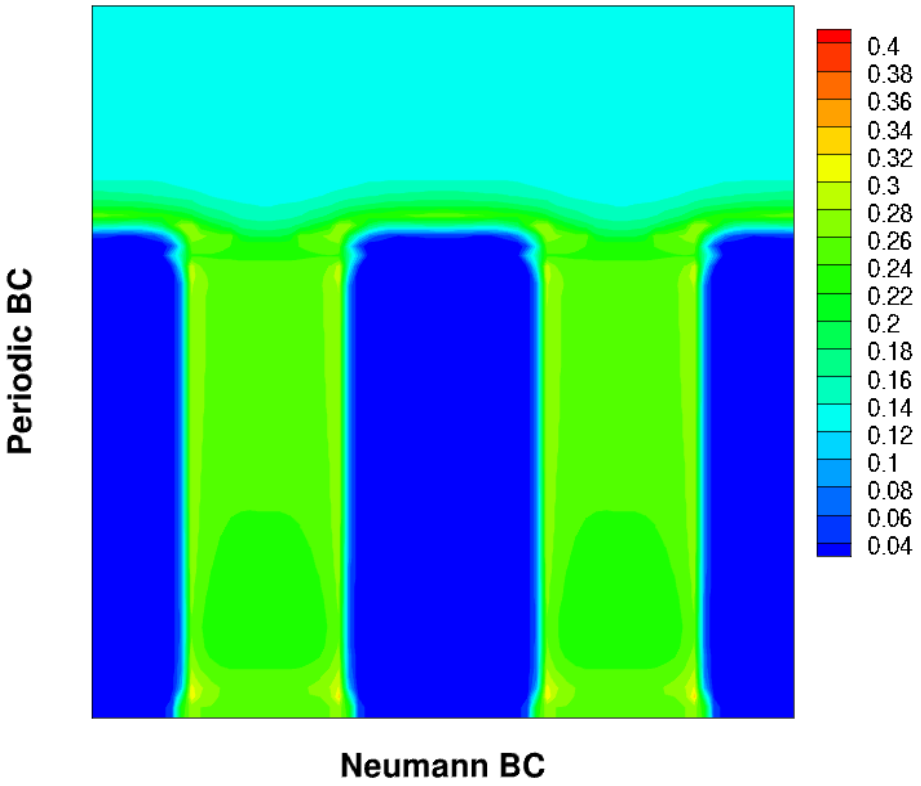

Figure 3.29: Phase-field simulation at 450^0C to demonstrate that kinetics can sustain the metastable γ_{1-2} phase and lead to the stable lamellar growth of DP (note that yellow regions are γ_{1-2} precipitates, blue regions are α precipitates, and light blue region is γ_1 matrix).

bility and permeability at the $\alpha|\gamma_{1-2}$ interface are specifically 1.5 times smaller than those at the $\alpha|\gamma_1$ interface and 2 times smaller than those at the $\gamma_{1-2}|\gamma_1$ interface. For thermodynamic driving forces, the strain-adjusted free energies are made use of. Although these energetic profiles tend to feature Djuric's hypothesis, they are not needed in this case to sustain the intermediate γ since kinetics has taken this part in the way that was described above (notice how the composition in the γ lamellae differ from the LE γ_{1-2} value which is ~ 48 at% Nb in this case of 450^0C). The reason for using the strain-adjusted free energies here is that it allows the composition of the sustained intermediate γ to stay below the inflection point of the miscibility gap, which in this case is shifted to higher value relative to that of the CALPHAD free energy due to the additional strain energy, and therefore lies out of the unstable region of γ's free-energy landscape. Very importantly, this allows the interface between the γ precipitate and matrix to stay dormant with minimal driving force (see Fig. 3.30 for demonstration) and ready to be carried forward by the α precipitate just like in the previous case (see Fig. 3.27) but this times under the control of kinetics. Otherwise, the thermodynamic driving force at this interface will effectively push the interface backwards in opposite to the growth direction in order to achieve the LE between the two γ phases. In other words, it will favor the spinodal decomposition which will promote the intermediate γ to stable γ_2 before the lamellar growth. This will prevent the discontinuous reaction from occurring in the proposed kinetic mechanism as the γ phases refuse to collaborate during the initiation of the reaction (i.e. (1) it moves against the direction favored by the kinetic mechanism, and (2) it bypasses DP with DC).

From the above observation, it is concluded that kinetics can also act as the main mechanism for the growth of DP. This mechanism tends to relax the strict thermodynamic condition proposed by Djuric. Yet, minimal support from thermodynamics

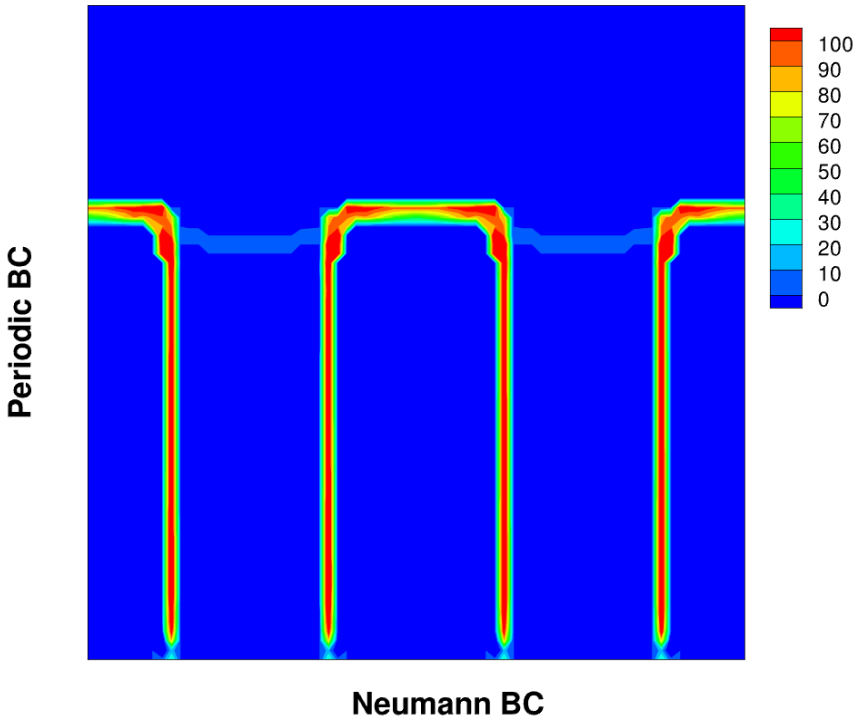

Figure 3.30: Driving force (J/cm^3) distributed at different interface at 450^0C under the investigated kinetic mechanism (note that positions of the precipitates and matrix correspond to those in Fig. 3.29).

is still required for a successful initiation of the reaction. Within the context of this work, the particular thermodynamic requirement is that the intermediate composition of the metastable γ phase should not lie within the thermodynamically unstable region of γ energetic profile and for this the additional strain energy is needed.

With great sophistication comes great challenges. The more we investigate uranium-niobium, the more we realize that this is indeed true for this system. The discontinuous reaction, the spinodal decomposition, the shape memory effect, etc., each of which has its own level of complication in thermodynamics, kinetics, and/or crystallographic nature which are perplexing problems in themselves. And yet, at the beginning we had such a naive impression that the binary system is simple-but-not-simplistic enough for a decent demonstration of ICMSE advantages in the research and development of Gen-IV metallic fuels. It is clear now that extensive investigation of the system is much exhausted and that at some point there must be an end to this work. Before this end, it would be interesting to investigate one last possible explanation for the origin of uranium-niobium's DP.

3.6 Discussion on the Strelova's ordering tendency and its relation to the occurrence of discontinuous precipitation

Upon finishing his work, Djuric had fairly pointed out that another possibility exists and relates to the interesting finding of Strelova *et al.* [43]: "*Another possibility could be derived from the work of Strelova et al.* [10]*), who found a pronounced tendency to short-range ordering in the equiatomic U-Nb alloy. This tendency could lower the free energy of the system and allow another, intermediate, state during the decomposition of the gamma phase*" [1]. If this was true, the short-range ordering would tentatively explain the recent experimental study [31] which observed that the intermediate γ_{1-2} composition remains constant at about 50 at.% Nb through-

out the temperature domain from 350^0C to 550^0C. Unfortunately, so far, there has been little evidence to support Strelova's work. Further investigations are needed to verify this interesting observation.

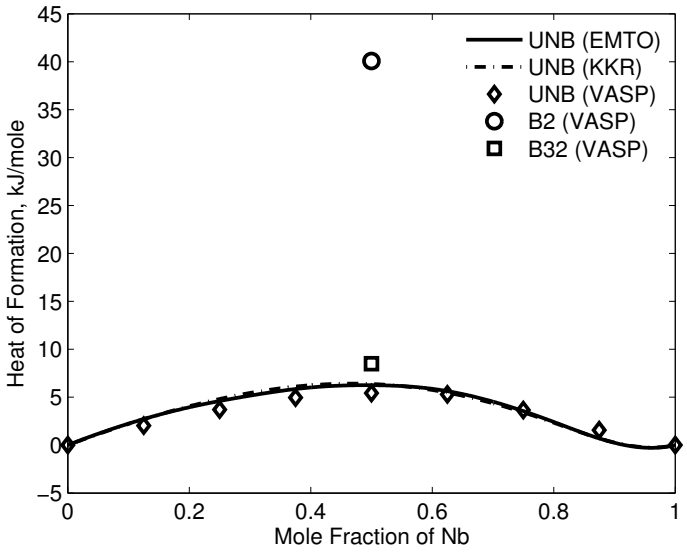

Figure 3.31: Formation energies of ordered B2 and B32 equiatomic uranium-niobium relative to that of disordered A2 uranium-niobium.

In order to encourage such investigations, we dedicate this last section to discuss a little bit about the Strelova's ordering tendency and its relation to the occurrence of discontinuous reactions. To begin with, first-principles calculations of short-range ordering in the equiatomic alloy were conducted in order to directly compare with experiments. Yet, due to technical issues, this first trial was not very successful. Alternatively, we calculated the formation energies of possible ordered bcc structures in order to estimate the relative stability between the ordered and disordered phases, hoping that this would shed some light on the ordering tendency of the material.

This turned out to be assessable using the VASP package, which is best optimized for studying intermetallic compounds. The two ordered bcc considered were the common B2 and B32. Their ground-state heats of formation were calculated and compared with that of A2 as in Fig. 3.31. As can be seen from this figure, the formation energy of B2 structure is significantly larger than that of A2. It is therefore concluded that the probability of observing this ordered phase forming inside the A2 structure is low. Similar conclusion may also be applicable in the case of B32 for the same reason although things could turn out to be more complicated for this ordered phase during the discontinuous monotectoid reaction, as follows:

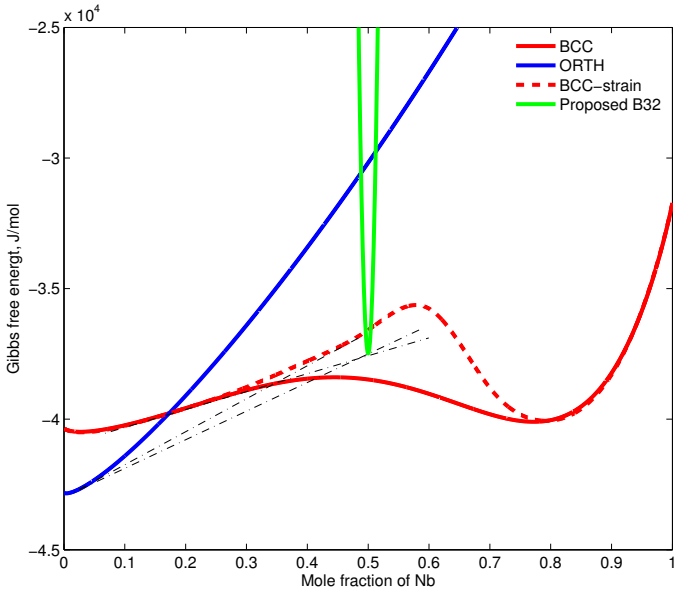

Figure 3.32: Hypothetical free energy of B32 at 450^0C relative to those of α and γ. Notice that the free energy of B32 is larger than that of γ when strain is not considered but become smaller than that of γ when additional strain energy is taken into account.

Let us first recall that during DP it is believed that the internal strain due to lattice/volume mismatch between α and γ will increase the free energies of the two reacting phases around the interfacial region. Intuitively, this energetic increase could result in a change of relative stability between the disordered A2 and ordered B32. To demonstrate this, the free energies of α, γ, and B32 are plotted in Fig. 3.32. In this figure, the solid blue line and dashed red line are the CALPHAD free energies of α and γ respectively, the solid red line is the proposed strain-adjusted free energy of γ, and the solid green line is the proposed free energy of B32. Here, the proposed free energy for the tip of the B32 parabola is expressed in temperature-composition-decoupling form of Eq. 3.5 as follows:

$$\begin{aligned} G_{Nb,U:Vac} &= x_{Nb}G^0_{Nb} + (1-x_{Nb})G^0_U + \\ &\quad + RT\left(x_{Nb}\ln x_{Nb} + (1-x_{Nb})\ln(1-x_{Nb})\right) + \\ &\quad + A(x_{Nb}) + B(x_{Nb})T \end{aligned} \tag{3.16}$$

where $A(x_{Nb})$ equals the ground-state formation energy of B32 and $B(x_{Nb})$ is empirically taken to be -8. Note that the choice of $A(x_{Nb})$ value is made so as to allow Eq. 3.16 to reproduce the heat of formation energy of B32 at 0 K. Also, the negative value of $B(x_{Nb})$ is chosen in order to reflect the ordering tendency of B32 at elevated temperatures, since it will decease the free energy of this value when temperature increases. Optionally, additional terms expressing the nonlinear dependency on temperature of B32 may be added to Eq. 3.16. This would allow the ordered phase to be less favorable than the disordered phase at high temperatures closing to the melting point. Such an ordering tendency can be similarly found in the σ phase of the iron-chromium system [177].

As can be seen from Fig. 3.32, although B32 is originally less stable than A2, it could become more stable than the disordered phase when this phase is under strain. This is of course under the assumption that the chosen $B(x_{Nb})$ has already accounted for the effect of strain energy on the thermodynamics of B32. Giving all this, B32, as an intermetallic compound with different thermodynamics (i.e. energetic profile) than that of A2 but the same bcc structure, will form a LE with α which explains the intermediate γ_{1-2} of DP. B32 also tends to form another LE with γ_1 which would allow better sustainment of its interface with this phase during the monotectoid decomposition. If, in case α also formed another LE with γ_1 as in the case of Djuric's hypothesis, DP would occur in a way similar to a eutectoid reaction. In such a case, the triple junction between α, γ and B32 is strictly governed by the three pairs of common tangents and the stable growth of DP's lamellae will be strongly dependent on the thermodynamics of the uranium-niobium system. The kinetic condition, i.e. fast grain boundary diffusion, in this case would not be essential for the occurrence of DP as it is in the cases of the kinetics and Djuric's hypotheses. Even if α does not form a LE with γ, the DP reaction could still occur but in this case the kinetic effect is likely needed to sustain the stable lamellar growth. Of course, all these explanations or ultimately another possible hypothesis for the occurrence of DP stemming from Strelova's short-range ordering only hold when B32 exhibits the above hypothetical free energy with the negative value of $B(x_{Nb})$. Is this really the case?

We conducted first-principles calculations of the free energies of B32 uranium-niobium using the supercell approach as implemented in the ATAT package [178]. Result is shown in Fig. 3.33. To compare this calculated free energy with the CALPHAD free energies shown in Fig. 3.32, a change in energy reference from one implemented in the VASP package to the SGTE values made use of for the CALPHAD energies is needed. For this, first-principles calculations of free energies of

A2 uranium and niobium were also carried out and their results are also reported in Fig. 3.33. From these quantum mechanical-based energies, the formation energy of B32, ΔG^{B32}_{UNb}, was calculated as follows:

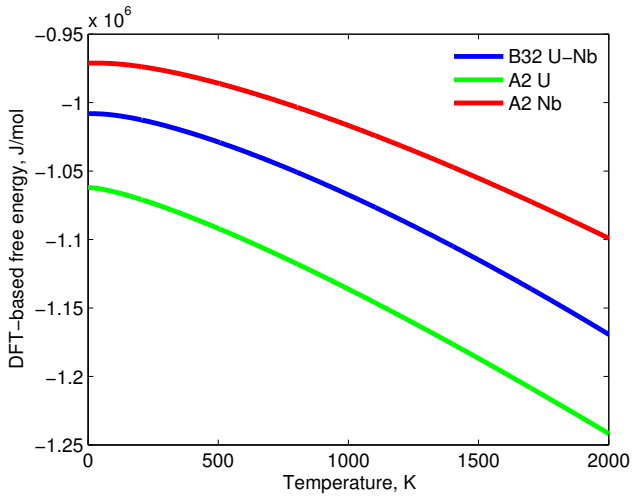

Figure 3.33: First-principles-based finite-temperature free energies of B32 uranium-niobium, A2 uranium, and A2 niobium.

$$\Delta G0^{B32}_{UNb} = G0^{B32}_{UNb}(T) - 0.5G0^{A2}_{U}(T) - 0.5G0^{A2}_{Nb}(T) \tag{3.17}$$

where $G0$ is to indicate that the free energies are quantum mechanical-based. It is noted that by subtracting the free energies of the pure element, some systematic error induced during the first-principles calculations would also be negated. The calculated free energy of B32 can now be written with the SGTE reference as follows:

$$G1^{B32}_{UNb} = \Delta G0^{B32}_{UNb}(T) - 0.5G1^{A2}_{U}(T) - 0.5G1^{A2}_{Nb}(T) \tag{3.18}$$

where $G1$ is to indicate that the free energy is now CALPHAD-based. To verify

whether or not such a reference change is reliable, we plotted the first-principles free energy against the newly derived CALPHAD free energy in Fig. 3.34. It is noted that in this case, the whole first-principles free energy curve is shifted by a constant equal to the different between this energy and the new CALPHAD free energy at 300 K. It can be seen from the figure that the difference between the energetic curves are minimal, which indicates that the accuracy of the reference change is acceptable.

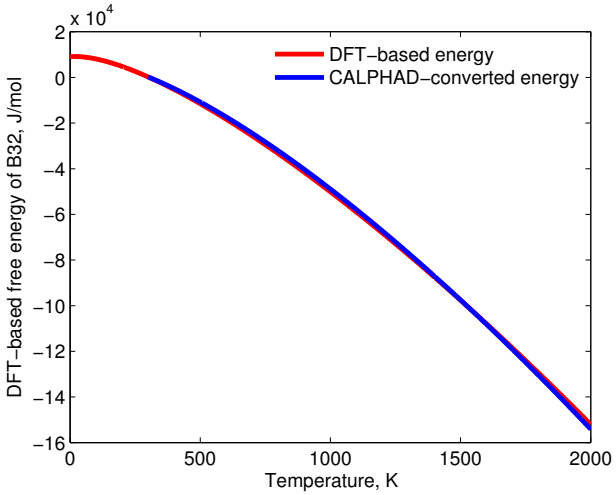

Figure 3.34: Quantum mechanical-based free energy vs CALPHAD-converted free energy for B32. Here, it is noted that the first-principles-based free energy is shifted by a constant to make it easier to compare with the CALPHAD-converted free energy.

We now fit this new CALPHAD free energy of B32 to the model parameters: $A(x_{Nb})$ and $B(x_{Nb})$ in Eq. 3.16. The result is plotted against the CALPHAD free energies converted from first-principles calculations and the proposed energy that favors Strelova's ordering tendency, as shown in Fig. 3.35. As can be seen from this figure, the fitted free energy does not match very well with the derived CALPHAD free energy. This indicates that B32 exhibits a slightly nonlinear temperature de-

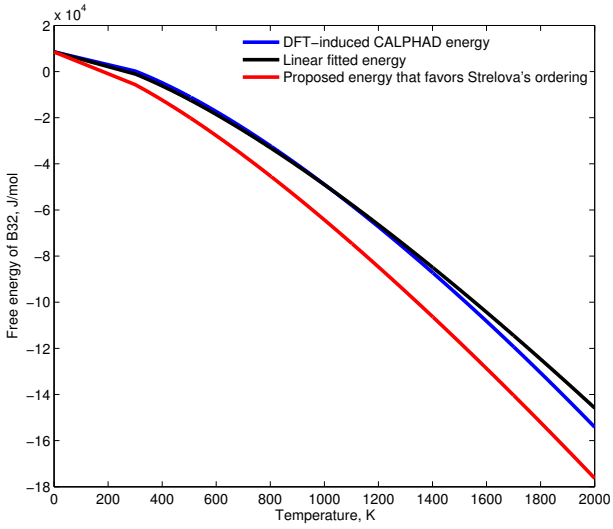

Figure 3.35: CALPHAD-converted free energy vs fitted free energy vs proposed free energy for B32.

pendence. Nevertheless, the difference is small and the resulting $A(x_{Nb})$ and $B(x_{Nb})$ parameters are acceptable. Here, the value of $A(x_{Nb})$ is again the same ground-state heat of formation of B32. The value of $B(x_{Nb})$ in this case, however, has the positive value of 6.2 as opposed to the negative value of -8 in the case of the proposed energy. This positive value will act to decrease the free energy of B32 when temperature increases and therefore will not favor the stability of B32 over that of A2 at high temperatures. This is true even when the effect of strain to the free energy of A2 is considered, as indicated in Fig. 3.36. It is therefore concluded that the short-range ordering, if it indeed happened in A2 as according to Strelova *et al.* [43], is less likely to favor B2 and B32; or, even if it did it would not be pronounced enough to lead to the intermediate state of γ_{1-2}. Yet, there perhaps exists other ordered bcc structures with equiatomic composition that exhibit the above hypothetical free energy that tends to explain for the occurrence of DP in the uranium-niobium system. Fur-

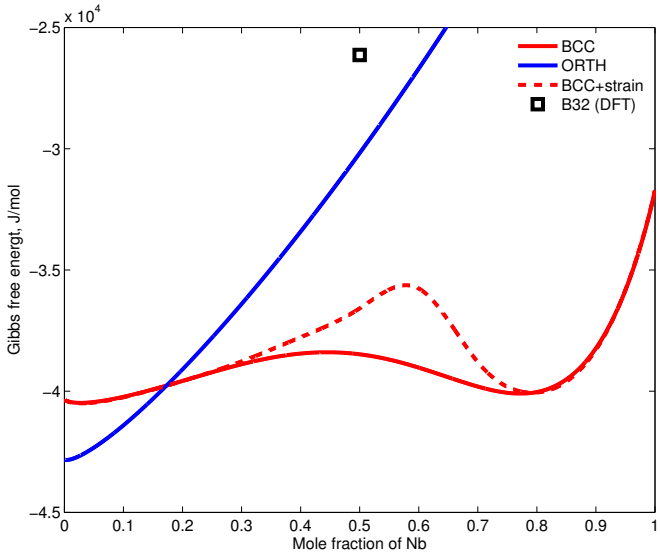

(a) 450^0C

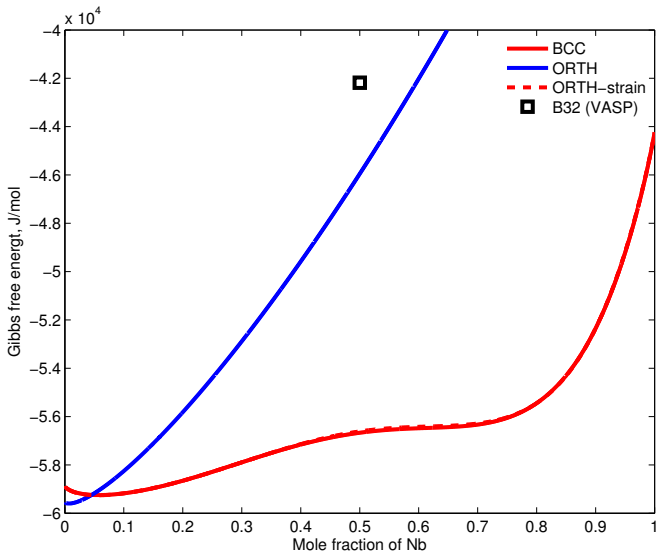

(b) 650^0C

Figure 3.36: First-principles free energies of B32 at 450^0C and 650^0C as compared to those of A2. Note here that the free energies of B32 are significantly higher that those of A2, which indicates that B32 is not a favorable phase at high temperature.

ther investigations on this matter are highly recommended to shed more light into the thermodynamics nature of uranium-niobium system as well as the occurrence of its discontinuous precipitation.

4. SUMMARY AND OUTLOOK

4.1 Summary

To summarize, an integrated computational study is carried out in this major section to investigate Djuric's hypothesis on the origin of uranium-niobium's discontinuous monotectoid decomposition. In particular, first-principles calculations are carried out to estimate the ground-state heats of formation of γ. Within the framework of CALPHAD, the resulting *ab initio* energetic data is coupled with available experiments to assess for a self-consist thermodynamic description which is in turn used to evaluate atomic mobility and diffusivity of γ. Assessment results are generally in good agreement with experiments, especially our current long-term aging experiments. With the self-consistent thermodynamic and kinetic information available, phase-field diffusion-couple simulations are then carried out to investigate possible LE between the CALPHAD free energies of α and γ to see whether or not these two phases form with two local equilibriums each other as hypothesized by Djuric.

Interestingly, it is found that the acquired CALPHAD free energies on one hand agree with Djuric's hypothesis within $605^0C - 647^0C$, while on the other hand disagree with the thermodynamic assumption between $400^0C - 605^0C$. To resolve this partial agreement in favor of the thermodynamic assumption, the CALPHAD free energies within $400^0C - 605^0C$ are revisited to see if there existed a special condition under which the hypothesis could be accommodated. It is interestingly found that when the stress/strain due to volume/lattice mismatches between α and γ is considered, the CALPHAD free energies of α and γ could actually be extended to accommodate the thermodynamic hypothesis. To account for the additional strain energy, new energetic profiles are empirically sketched out based on the original CAL-

PHAD energies and by following Djuric's proposal. The resulting energies are the combination of both CALPHAD chemical energies as well as the additional strain energy and are called strain-adjusted energies that are only valid for coexisting α and γ lamellae with non-trivial strain/stress field. The quantitative description of these energies is given by a modified CALPHAD model for the interval of interest. This description can be seen as a manifestation of the thermodynamic hypothesis's possibility enabled by the key assumption that strain/stress field around the interfacial region between α and γ plays an important role in 'stabilizing' the intermediate LE between the two reacting phases, as indicated by the current hierarchical computational thermodynamic and kinetic investigation.

Using the strain-adjusted free energies, phase-field simulations are carried out to investigate the roles of kinetics on the stable lamellar growth of DP. It was concluded that the thermodynamic hypothesis proposed by Djuric is one possible explanation for the occurrence of the discontinuous reactions in niobium-uranium, given that the effect of strain on thermodynamics and the kinetics of the reaction front are properly accounted for. During the phase-field investigations under Djuric's hypothesis, it was interestingly found that kinetics can actively sustain the metastable γ phase and lead to the stable lamellar growth of DP. This gave rise to another possible explanation for the origin of the discontinuous precipitation. Interestingly, this hypothesis tended to relax the strict two local equilibrium condition in Djuric's hypothesis. Yet, it still tended to rely on a minimal thermodynamic requirement in order to initiate the reaction. Lastly, Strelova's ordering tendency and its relation to the occurrences of the discontinuous reactions was discussed. Via first-principles calculations of formation energies of B2 and B32 structure, we found that such ordering tendency does not seem to occur for the two investigated order structures. Yet, there perhaps exists other ordered equiatomic bcc structures which agree with Strelova's observation and

therefore tend to exhibit an energetic profile that explains the occurrence of DP in the uranium-niobium system.

Via the current work, the author hopes to contribute towards a better understanding of the thermodynamics and kinetics that govern the uranium-niobium system and its interesting discontinuous precipitation. It is believed that such a fundamental understanding will come in handy in the future research and development of this metallic fuel and other advanced fuels that make use of uranium and niobium. The author also hopes to have successfully demonstrated the advantage of ICMSE in the research and development of metallic fuels for Gen-IV fast breeder reactors. Such an advantage is reflected particularly in the current integrated framework via its versatility in assessing fundamental thermodynamics and kinetics of the material in order to investigate different hypotheses on the origin of the discontinuous reactions. Furthermore, various perspectives on the applications of this ICMSE framework for scientific and engineering purposes exist to further demonstrate this. Let us list a few in the following section.

4.2 Outlook

The current framework can be adopted to investigate the thermodynamic and kinetic effects on different stable and metastable microstructures of uranium-niobium such as the discontinuous coarsening reaction (DC) which is left unsolved in the current study. From an engineering point of view, since DC, like DP, also tends to degrade the fuel's corrosion resistance and ductility, it also offers practical interest. From a scientific point of view, DC is also an interesting problem to investigate. Indeed, although less complicated than DP, DC does not necessarily occur in a straightforward manner as assumed by Djuric. To demonstrate this, a phase-field simulation was carried out to have a first look at the microstructural evolution of

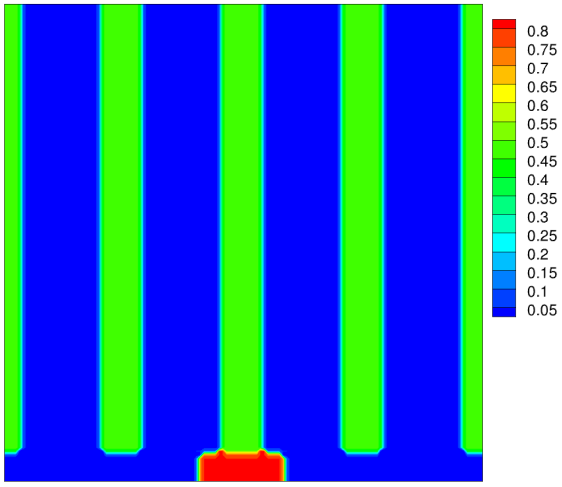

Figure 4.1: Initial configuration of the phase-field investigation of DC at 450^0C under Djuric's hypothesis and volume-diffusion-controlled assumption (note that color indicates mole fraction of Nb, as such red region corresponds to γ_2 precipitate, blue regions correspond to α precipitates, and green regions correspond to γ_{1-2} precipitates).

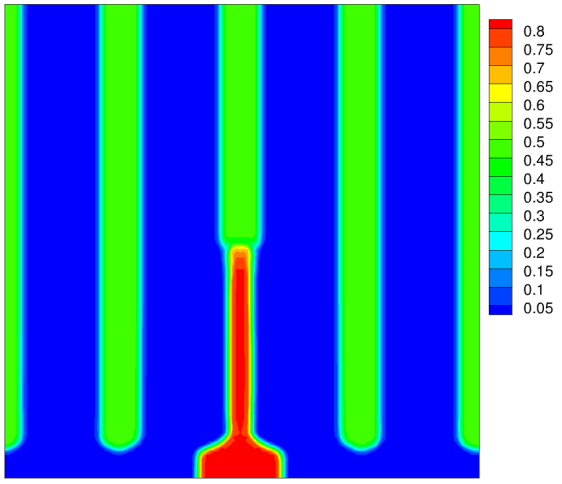

Figure 4.2: Phase-field investigation of DC at 450^0C under Djuric's hypothesis and volume-diffusion-controlled assumption (note that color indicates mole fraction of Nb, as such red region corresponds to γ_2 precipitate, blue regions correspond to α precipitates, and green regions correspond to γ_{1-2} precipitates).

DC. For this trial, a small γ_2 precipitate is initially nucleated at the grain boundary where the DP's lamellae grow, as shown Fig. 4.1. Here, the simulation domain is $192 \times 192\ nm$. The simulation is subjected to Djuric's hypothesis and the assumption that DC is a volume-diffusion-controlled process. It is simulated at 450^0C and uses the same physical and model parameters as reported in Table 3.5. Simulation result is shown in Fig. 4.2. As can be seen from this figure, the reaction progresses in a way that favors the growth of stable γ_2 at the cost of metastable γ_{1-2}, consistent with Djuric's assumption; however, the γ_2 precipitate does not appear to coarsen. The reason for this is that the long-range diffusion to redistribute Nb content from the neighboring γ_{1-2} precipitates to the γ_2 precipitate and hence allow coarsening in this case happens at a much lower rate than the short-range diffusion happening at the interface the between γ_2 and the γ_{1-2} precipitate within which it was nucleated. Further investigation on the effects of kinetics on DC are needed to shed more light on the origin of this reaction.

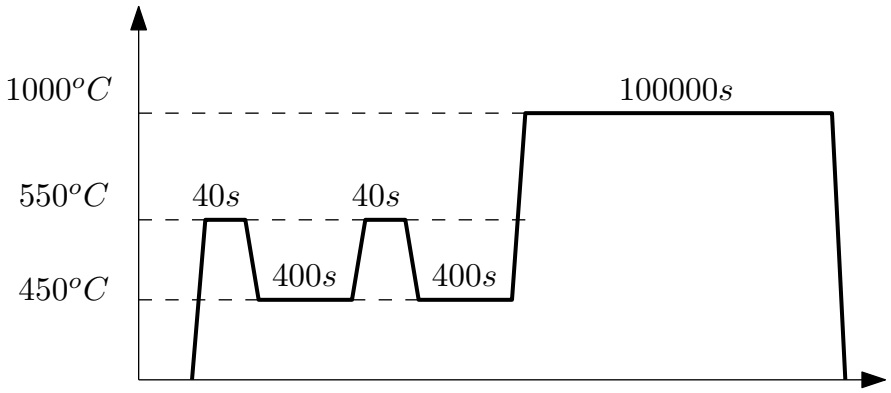

Figure 4.3: Schematic 5-stage heat treatment.

The integrated framework can also be applied to many practical problems such as

alloy design, materials processing, and manufacturing cycles. Indeed, on the current scale, it can be used to simulate various heat treatment processes under different temperature and time conditions to investigate the product microstructures, which are important for the final performance of the material. To illustrate this, we conducted a simulation according to the heat treatment history shown in Fig. 4.3. This simulation is under the assumption that Djuric's hypothesis indeed explains the origin of DP. The motivation for this simulation is rather naive. Since under Djuric's hypothesis, the interlamellar spacings at different temperatures are different, we thought that we could make use of this phenomenon to engineering the lamellar microstructure into various spherical precipitates using the heat treatment history presented in Fig. 4.3. The results are shown in Fig. 4.4. As evidence by this figure, we could not achieve the spherical precipitates as expected. The reason for this is perhaps that the difference in the interlamellar spacing at different temperatures is not pronounced. Instead, what we observed from the last heat treatment stage is interestingly close to the 'ghost image' which is a special feature of discontinuous dissolution (the inverse process of the discontinuous precipitation or coarsening) [19]. Although it would take further investigations to verify whether discontinuous dissolution is a physical feature of uranium-niobium, the current observation is good enough to showcase the capability of the ICMSE framework in exploring properties/phenomena that are dependent on the fundamental thermodynamics and kinetics of the system. Such a capability is very important to the research and development of materials.

The ICMSE framework can also be extended to include continuum-scale toolkits for the performance analysis of materials. This would further advance the framework's advantages and practicality. An example for this would be the finite element analysis of the effect of microstructure on the performance of the material and product as shown in Fig. 4.5. Here, the lamellar microstructure of DP at 450^0C was ana-

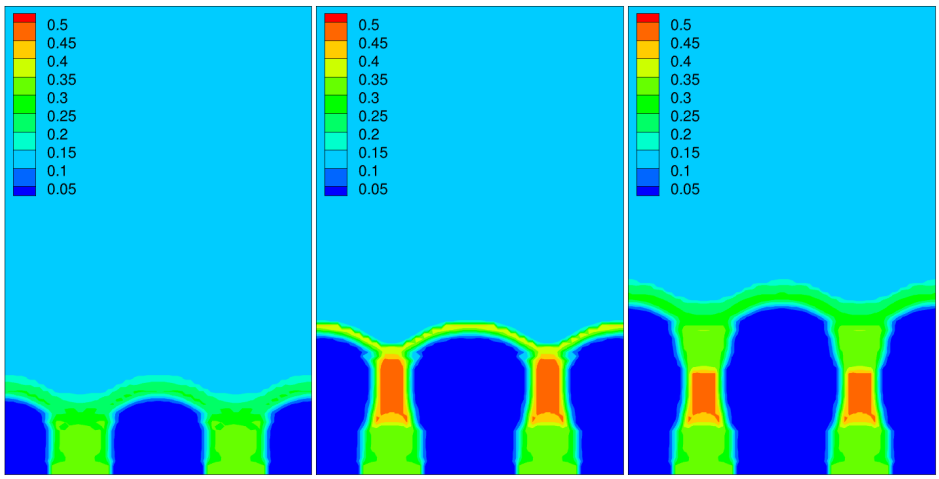

(a) Stage 1 (b) Stage 2 (c) Stage 3

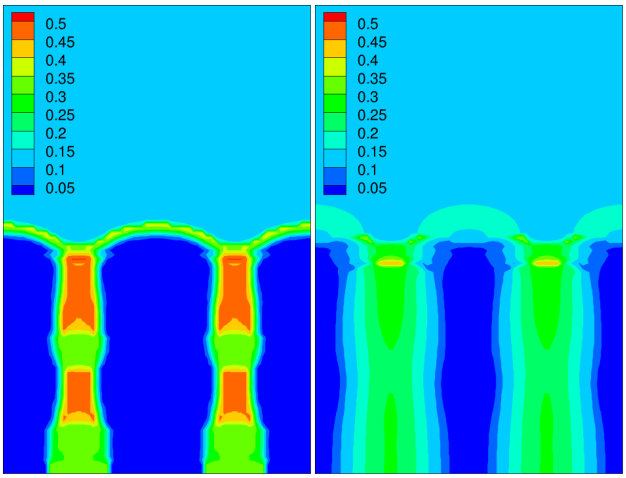

(d) Stage 4 (e) Stage 5

Figure 4.4: Phase-field simulation of the many-stage heat treatment process (note that color indicates mole fraction of Nb, as such light blue region corresponds to γ_1 matrix, blue regions correspond to α precipitates, and regions between α precipitates are γ_{1-2} precipitates).

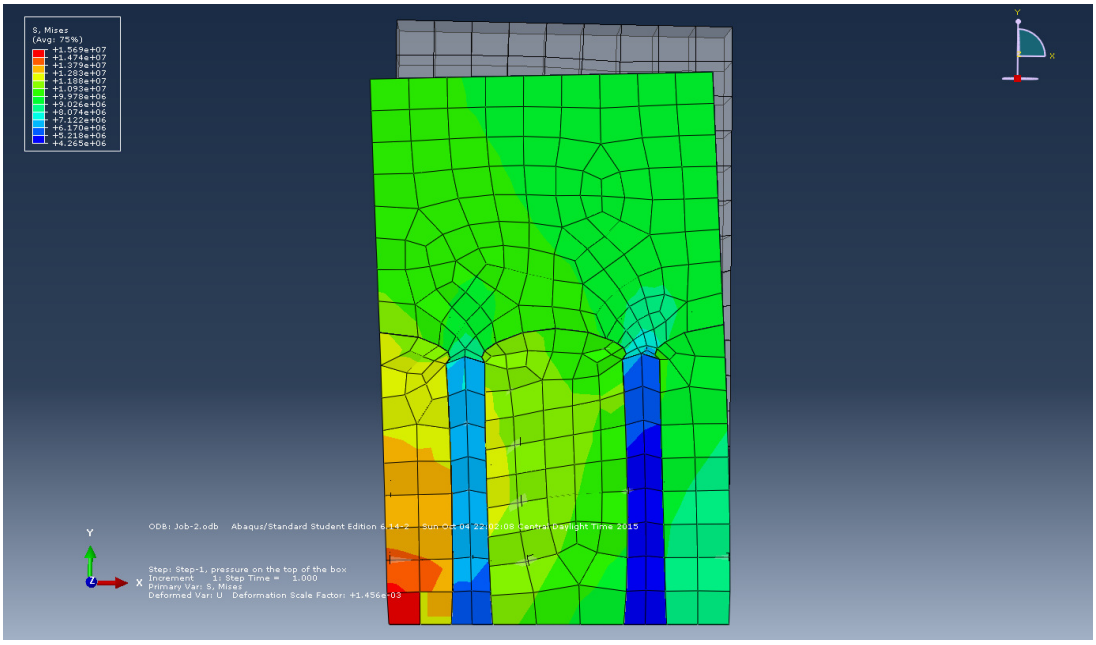

Figure 4.5: Finite-element analysis of the DP's lamellae under pressure and shear stresses.

lyzed for stress distribution under the conditions of compressive and shear stresses on the top and left boundaries of the microstructure respectively using Abaqus. Given reasonably accurate material informations, such continuum analysis could be used either for materials prognosis, i.e. to predict the failure of the nuclear fuel, or for fuel design, i.e. optimize processing condition to minimize the negative impacts of the microstructure. Other examples include the integration of dislocation dynamics to investigate material behavior under plastic deformation or coupling of thermal analysis and mechanical models to investigate fatigue strength under different temperature and loading cycles. Recently, it was proposed to use additive manufacturing in the research and development of advanced nuclear fuels. The author finds this to be a very interesting idea and the current integrated framework can be very helpful to realize it in an effective and efficient manner.

With this, we complete the current effort in encouraging the implementation of ICMSE in the research and development of nuclear fuels and IFR with an optimistic hope that it will be further advanced by fellow scientists and engineers, who work in the field of computational materials science and engineering or benefit greatly from it.

REFERENCES

[1] B Djurić. Decomposition of gamma phase in a uranium-9.5 wt% niobium alloy. Journal of Nuclear Materials, 44(2):207–214, 1972.

[2] BA Rogers, DF Atkins, EJ Manthos, and ME Kirkpatrick. Uranium-columbium alloy diagram. Trans. Met. Soc. AIME, 212:387–393, 1958.

[3] Ross J Jackson. Reversible martensitic transformation between transition phases of uranium-base niobium alloys. Technical report, Dow Chemical Co., Golden, Colo. Rocky Flats Div., 1970.

[4] Yu V Vambersky, AL Udovsky, and OS Ivanov. Investigation of thermodynamic properties of bcc solid solutions of uranium (ii). the uranium-niobium system. Journal of Nuclear Materials, 55(1):96–108, 1975.

[5] XJ Liu, ZS Li, J Wang, and CP Wang. Thermodynamic modeling of the U-Mn and U-Nb systems. Journal of Nuclear Materials, 380(1):99–104, 2008.

[6] Yajun Liu, Di Yu, Yong Du, Guang Sheng, Zhaohui Long, Jiang Wang, and Lijun Zhang. Atomic mobilities, diffusivities and their kinetic implications for U-X (X = Ti, Nb and Mo) bcc alloys. CALPHAD, 37:49–56, 2012.

[7] Georgij B Fedorov and Evgeniĭ Aleksandrovich Smirnov. Diffusion in reactor materials. Technical report, National Bureau of Standards, Washington, DC (USA), 1984.

[8] International Energy Agency. Energy technology perspectives 2010. 2012.

[9] International Energy Agency. Energy technology perspectives 2010. 2014.

[10] Energy Information Administration. Monthly energy review. Febuary, 2015.

[11] Department of Energy. Nuclear energy research and development roadmap. 2010.

[12] World Nuclear Association. World energy needs and nuclear power. http://www.world-nuclear.org/info/Current-and-Future-Generation/World-Energy-Needs-and-Nuclear-Power/, 2015. [Online; accessed March 7, 2015].

[13] Nuclear Energy Agency and International Energy Agency. Technology roadmap – nuclear energy. 2010.

[14] Stanley H Fistedis. The experimental breeder reactor-II inherent safety demonstration, EBR-II division, Argonne national laboratory Idaho Falls, Idaho and Argonne, Illinois, USA, april 1986. Nuclear engineering a. des., 101(1), 1987.

[15] DC Wade and YI Chang. The integral fast reactor concept: physics of operation and safety. Nuclear science and engineering, 100(4):507–524, 1988.

[16] Tadashi Inoue and Lothar Koch. Development of pyroprocessing and its future direction. Nuclear Engineering and Technology, 40(3):183, 2008.

[17] John Allison, Mei Li, C Wolverton, and XuMing Su. Virtual aluminum castings: an industrial application of ICME. JOM, 58(11):28–35, 2006.

[18] National Research Council on Integrated Computational Materials Engineering. Integrated computational materials engineering: a transformational discipline for improved competitiveness and national security. National Academies Press, 2008.

[19] I Manna, SK Pabi, and W Gust. Discontinuous reactions in solids. International Materials Reviews, (46):53–91, 2001.

[20] R.A. Vandermeer. Phase transformations in a uranium-14 at.% niobium alloy. Acta Metallurgica, (28):383–393, 1980.

[21] KH Eckelmeyer, AD Romig, and LJ Weirick. The effect of quench rate on the microstructure, mechanical properties, and corrosion behavior of U-6 wt pct Nb. Metallurgical Transactions A, 15(7):1319–1330, 1984.

[22] Heather M Volz, Robert E Hackenberg, Ann M Kelly, WL Hults, AC Lawson, RD Field, DF Teter, and DJ Thoma. X-ray diffraction analyses of aged U-Nb alloys. Journal of Alloys and Compounds, 444-445:217–225, 2007.

[23] AJ Clarke, RD Field, RE Hackenberg, DJ Thoma, DW Brown, DF Teter, MK Miller, KF Russell, DV Edmonds, and G Beverini. Low temperature age-hardening in U-13 at.% Nb: an assessment of chemical redistribution mechanisms. Journal of Nuclear Materials, 393:282–291, 2009.

[24] RJ Jackson and DV Miley. Tensile properties of gamma quenched and aged uranium-rich niobium alloys. Trans. ASM, (61):336, 1968.

[25] RJ Jackson. Isothermal transformations of uranium-13 atomic percent niobium. Rocky Flats Plant (Golden, CO), report RFP-1609 (9 April 1971).

[26] KH Eckelmeyer. Aging phenomena in dilute uranium alloys. In Physical Metallurgy of Uranium Alloys, J.J. Burke, D.A. Colling, A.E. Gorum, and J. Greenspan, ed. (Brook Hill, Chestnut Hill, MA, 1976), pages 463–509.

[27] OS Ivanov and GI Terekhov. Disintegration of gamma-solid solution of uranium and niobium. The Structure of Alloys of Certain Systems Containing Uranium and Thorium in The Structure of Alloys of Certain Systems Containing Uranium and Thorium [translation AEC-TR-5834 (U.S. Atomic Energy

Commisson, Washington, DC, July 1963)], E.M. Potapova, ed. (Gosatomizdat, Moscow, 1961), pages 35–47 (33–44 in translation), 1961.

[28] OS Ivanov and Y.S. Virgiliev. The decomposition of the gamma-uranium base solid solutions as revealed by x-ray diffraction. J. Nucl. Mater., 6:199–202, 1962.

[29] WD Wilkinson. Uranium metallurgy. 2:1231, 1962.

[30] C D'Amato, FS Saraceno, and TB Wilson. Phase transformations and equilibrium structures in uranium-rich niobium alloys. Journal of Nuclear Materials, 12(3):291–304, 1964.

[31] Robert E Hackenberg, Heather M Volz, Pallas A Papin, Ann M Kelly, Robert T Forsyth, Tim J Tucker, and Kester D Clarke. Kinetics of lamellar decomposition reactions in U-Nb alloys. Solid State Phenomena, 172:555–560, 2011.

[32] DB Williams and EP Butler. Grain boundary discontinuous precipitation reactions. International Metals Reviews, 26(1):153–183, 1981.

[33] Z-K Liu, L-Q Chen, P Raghavan, Q Du, JO Sofo, SA Langer, and C Wolverton. An integrated framework for multi-scale materials simulation and design. Journal of Computer-Aided Materials Design, 11(2-3):183–199, 2004.

[34] Zi-Kui Liu, Long-Qing Chen, and Krishna Rajan. Linking length scales via materials informatics. JOM, 58(11):42–50, 2006.

[35] Zi-Kui Liu and Long-Qing Chen. Integration of first-principles calculations, CALPHAD modeling, and phase-field simulations. In Applied Computational Materials Modeling, pages 171–213. Springer, 2007.

[36] Ingo Steinbach, Lijun Zhang, and Mathis Plapp. Phase-field model with finite interface dissipation. Acta Materialia, 60(6):2689–2701, 2012.

[37] Lijun Zhang and Ingo Steinbach. Phase-field model with finite interface dissipation: extension to multi-component multi-phase alloys. Acta Materialia, 60(6):2702–2710, 2012.

[38] PCL Pfeil, JD Browne, and GK Williamson. The uranium-niobium alloy system in the solid state. J. Inst. Metals, 87:204–208, 1958–59.

[39] J Koike, ME Kassner, RE Tate, and RS Rosen. The Nb-U (niobium-uranium) system. Journal of Phase Equilibria, 19(3):253–260, 1998.

[40] Thaddeus B Massalski, Hiroaki Okamoto, PR Subramanian, Linda Kacprzak, et al. Binary alloy phase diagrams. ASM International, 1990.

[41] Saurabh Bajaj, Alexander Landa, Per Söderlind, Patrice EA Turchi, and Raymundo Arróyave. The U-Ti system: strengths and weaknesses of the CALPHAD method. Journal of Nuclear Materials, 419(1):177–185, 2011.

[42] Jan-Olof Andersson and John Ågren. Models for numerical treatment of multicomponent diffusion in simple phases. Journal of Applied Physics, 72(4):1350–1355, 1992.

[43] SV Strelova, Ya S Umansky, and OS Ivanov. Short-range order in uranium-niobium solid solution. Journal of Nuclear Materials, 34(2):160–164, 1970.

[44] Walter Kohn. Nobel lecture: electronic structure of matter-wave functions and density functionals. Reviews of Modern Physics, 71(5):1253–1266, 1999.

[45] Pierre Hohenberg and Walter Kohn. Inhomogeneous electron gas. Physical Review, 136(3B):B864, 1964.

[46] Axel D Becke. Perspective: fifty years of density-functional theory in chemical physics. The Journal of Chemical Physics, 140(18):18A301, 2014.

[47] Walter Kohn and Lu Jeu Sham. Self-consistent equations including exchange and correlation effects. Physical Review, 140(4A):A1133, 1965.

[48] Peter E Blöchl. Projector augmented-wave method. Physical Review B, 50(24):17953, 1994.

[49] Alex Zunger, S-H Wei, LG Ferreira, and James E Bernard. Special quasirandom structures. Physical Review Letters, 65(3):353, 1990.

[50] OK Andersen, O Jepsen, and G Krier. Exact muffin-tin orbital theory. Lectures on Methods of Electronic Structure Calculations, edited by V. Kumar, OK Andersen, and A. Mookerjee, World Scientific Publishing Co., Singapore, pages 63–124, 1994.

[51] Levente Vitos. Exact muffin-tin orbitals method. Computational Quantum Mechanics for Materials Engineers: The EMTO Method and Applications, pages 13–35, 2007.

[52] J Korringa. On the calculation of the energy of a Bloch wave in a metal. Physica, 13(6):392–400, 1947.

[53] W Kohn and N Rostoker. Solution of the Schrödinger equation in periodic lattices with an application to metallic lithium. Physical Review, 94(5):1111, 1954.

[54] BL Gyorffy. Coherent-potential approximation for a nonoverlapping-muffin-tin-potential model of random substitutional alloys. Physical Review B, 5(6):2382, 1972.

[55] Larry Kaufman and John Ågren. CALPHAD, first and second generation–birth of the materials genome. Scripta Materialia, 70:3–6, 2014.

[56] Nigel Saunders and A Peter Miodownik. CALPHAD (calculation of phase diagrams): a comprehensive guide, volume 1. Elsevier, 1998.

[57] Josiah Willard Gibbs. On the equilibrium of heterogeneous substances. American Journal of Science, (96):441–458, 1878.

[58] Oswald Kubaschewski, Charles B Alcock, and PJ Spencer. Materials thermochemistry. Pergamon press, 1993.

[59] JJ Van Laar. Melting or solidification curves in binary system. Z Phys Chem, 63:216, 1908.

[60] JJ Van Laar. Melting or solidification curves in binary system, part II. Z Phys Chem, 64:257–297, 1908.

[61] L Kaufman (1966a) private communication to L Brewer march 25.

[62] JL Meijering. Segregation in regular ternary solutions, part I. Philips Res Rep, 5:333–356, 1950.

[63] JL Meijering and HK Hardy. Closed miscibility gaps in ternary and quaternary regular alloy solutions. Acta Metallurgica, 4(3):249–256, 1956.

[64] JL Meijering. Calculation of the nickel-chromium-copper phase diagram from binary data. Acta Metallurgica, 5(5):257–264, 1957.

[65] Larry Kaufman. J.L. Meijering's contribution to the calculation of phase diagrams – a personal perspective. Physica B+C, 103(1):1 – 7, 1981.

[66] Larry Kaufman and Morris Cohen. The martensitic transformation in the iron-nickel system. Transactions of the American Institute of Mining and Metallurgical Engineers, 206(10):1393–1401, 1956.

[67] PJ Spencer. A brief history of CALPHAD. CALPHAD, 32(1):1–8, 2008.

[68] Larry Kaufman and Morris Cohen. Thermodynamics and kinetics of martensitic transformations. Progress in Metal Physics, 7:165–246, 1958.

[69] Hans Leo Lukas, Suzana G Fries, and Bo Sundman. Computational thermodynamics: the CALPHAD method, volume 131. Cambridge university press, 2007.

[70] L Kaufman (1966a) private communication to L Brewer, march 25.

[71] Larry Kaufman. The lattice stability of metals– I: titanium and zirconium. Acta Metallurgica, 7(8):575–587, 1959.

[72] Larry Kaufman. The stability of metallic phases. Progress in Materials Science, 14(2):57–96, 1969.

[73] O. Kubaschewski and T.G. Chart. Calculation of metallurgical equilibrium diagrams from thermochemical data. J. Inst. Metals, 93:329–338, 1965.

[74] M Hillert and LI Staffansson. Regular-solution model for stoichiometric phases and ionic melts. Acta Chem. Scand., 24(10):3618–3626, 1970.

[75] Bo Sundman and John Ågren. A regular solution model for phases with several components and sublattices, suitable for computer applications. Journal of Physics and Chemistry of Solids, 42(4):297–301, 1981.

[76] I Ansara, B Sundman, and Po Willemin. Thermodynamic modeling of ordered phases in the Ni-Al system. Acta Metallurgica, 36(4):977–982, 1988.

[77] A_T Dinsdale. SGTE data for pure elements. CALPHAD, 15(4):317–425, 1991.

[78] RH Davies, AT Dinsdale, SM Hodson, JA Gisby, NJ Pugh, TI Barry, and TG Chart. MTDATA–the NPL databank for metallurgical thermochemistry. User Aspects of Phase Diagrams, pages 140–145, 1991.

[79] CW Bale, P Chartrand, SA Degterov, G Eriksson, K Hack, R Ben Mahfoud, J Melançon, AD Pelton, and S Petersen. FactSage thermochemical software and databases. CALPHAD, 26(2):189–228, 2002.

[80] Gunnar Eriksson. Thermodynamic studies of high-temperature equilibria. 12. SOLGASMIX, a computer-program for calculation of equilibrium compositions in multiphase systems. Chemica Scripta, 8(3):100–103, 1975.

[81] Carelyn E Campbell, Ursula R Kattner, and Zi-Kui Liu. The development of phase-based property data using the CALPHAD method and infrastructure needs. Integrating Materials and Manufacturing Innovation, 3(1):1–23, 2014.

[82] Xiao-Gang Lu, Malin Selleby, and Bo Sundman. Assessments of molar volume and thermal expansion for selected bcc, fcc and hcp metallic elements. CALPHAD, 29(1):68–89, 2005.

[83] JD Van der Waals. The thermodynamic theory of capillarity flow under the hypothesis of a continuous variation of density. Journal of Statistical Physics, 20(2):179–245, 1979.

[84] John W Cahn and John E Hilliard. Free energy of a nonuniform system: I. interfacial free energy. The Journal of Chemical Physics, 28(2):258–267, 1958.

[85] V. Ginzburg and L. Landau. On the theory of superconductivity Zh. Eksp. Teor. Fiz. 20 (1950) 10641082. Translation in collected papers of L.D. Landau, Pergamon, Oxford, pages 546–568, 1965.

[86] P. Hohenberg and B. Halperin. Theory of dynamic critical phenomena. Rev. Modern Phys., 49:435–479, 1977.

[87] J. Gunton, M. Miguel, and P. Sahni. The dynamics of first-order phase transitions,. In C. Domb, J.L. Lebowitz (Eds.), 8:267–466, 1983.

[88] R. Kobayashi. Modeling and numerical simulations of dendritic crystal growth. Physica D, 63:410–423, 1993.

[89] Long-Qing Chen and AG Khachaturyan. Computer simulation of structural transformations during precipitation of an ordered intermetallic phase. Acta Metallurgica et Materialia, 39(11):2533–2551, 1991.

[90] Y Wang, L-Q Chen, and AG Khachaturyan. Kinetics of strain-induced morphological transformation in cubic alloys with a miscibility gap. Acta Metallurgica et Materialia, 41(1):279–296, 1993.

[91] T Miyazaki, A Takeuchi, T Koyama, and T Kozakai. Computer simulation of phase decomposition in the regular solid solution based upon the Cahn-Hilliards non-linear diffusion equation. Materials Transactions, JIM, 32(10):915–920, 1991.

[92] T Miyazaki, A Takeuchi, and T Koyama. Computer simulations of the phase decomposition on Cu-Co binary alloys based on the non-linear diffusion equation. Journal of Materials Science, 27(9):2444–2448, 1992.

[93] Hiraku Nishimori and Akira Onuki. Pattern formation in phase-separating alloys with cubic symmetry. Physical Review B, 42(1):980, 1990.

[94] D Rodney, Y Le Bouar, and A Finel. Phase field methods and dislocations. Acta Materialia, 51(1):17–30, 2003.

[95] Yann Le Bouar, A Loiseau, and AG Khachaturyan. Origin of chessboard-like structures in decomposing alloys. theoretical model and computer simulation. Acta materialia, 46(8):2777–2788, 1998.

[96] LA. Finel, G. Boussinot, Y. Le Bouar, and Q. Bronchart. Quantitative phase field modeling. JOM, 56:215, 2004.

[97] JS Langer. Models of pattern formation in first-order phase transitions. Directions in Condensed Matter Physics, 1:165–186, 1986.

[98] Seong Gyoon Kim, Won Tae Kim, and Toshio Suzuki. Phase-field model for binary alloys. Physical Review E, 60(6):7186, 1999.

[99] Alain Karma and Wouter-Jan Rappel. Phase-field method for computationally efficient modeling of solidification with arbitrary interface kinetics. Physical Review E, 53(4):R3017, 1996.

[100] Alain Karma. Phase-field formulation for quantitative modeling of alloy solidification. Physical Review Letters, 87(11):115701, 2001.

[101] Tak Shing Lo, Alain Karma, and Mathis Plapp. Phase-field modeling of microstructural pattern formation during directional solidification of peritectic alloys without morphological instability. Physical Review E, 63(3):031504, 2001.

[102] Blas Echebarria, Roger Folch, Alain Karma, and Mathis Plapp. Quantitative phase-field model of alloy solidification. Physical Review E, 70(6):061604, 2004.

[103] R Folch and M Plapp. Quantitative phase-field modeling of two-phase growth. Physical Review E, 72(1):011602, 2005.

[104] I Steinbach, F Pezzolla, B Nestler, M Seeßelberg, R Prieler, GJ Schmitz, and JLL Rezende. A phase field concept for multiphase systems. Physica D: Nonlinear Phenomena, 94(3):135–147, 1996.

[105] I Steinbach. Phase-field models in materials science. Modelling and Simulation in Materials Science and Engineering, 17(7):073001–073031, 2009.

[106] WJ Boettinger, JA Warren, C Beckermann, and A Karma. Phase-field simulation of solidification 1. Annual Review of Materials Research, 32(1):163–194, 2002.

[107] Long-Qing Chen. Phase-field models for microstructure evolution. Annual Review of Materials Research, 32(1):113–140, 2002.

[108] Long-Qing Chen and Wei Yang. Computer simulation of the domain dynamics of a quenched system with a large number of nonconserved order parameters: the grain-growth kinetics. Physical Review B, 50(21):15752, 1994.

[109] SY Hu and LQ Chen. Solute segregation and coherent nucleation and growth near a dislocation – a phase-field model integrating defect and phase microstructures. Acta Materialia, 49(3):463–472, 2001.

[110] YU Wang, YM Jin, AM Cuitino, and AG Khachaturyan. Phase field microelasticity theory and modeling of multiple dislocation dynamics. Applied Physics Letters, 78(16):2324–2326, 2001.

[111] YM Jin, YU Wang, and AG Khachaturyan. Three-dimensional phase field microelasticity theory and modeling of multiple cracks and voids. Applied Physics Letters, 79(19):3071–3073, 2001.

[112] Hervé Henry and Herbert Levine. Dynamic instabilities of fracture under biaxial strain using a phase field model. Physical Review Letters, 93(10):105504, 2004.

[113] Deepali N Bhate, Ashish Kumar, and Allan F Bower. Diffuse interface model for electromigration and stress voiding. Journal of Applied Physics, 87(4):1712–1721, 2000.

[114] A Kazaryan, Y Wang, and Bruce R Patton. Generalized phase field approach for computer simulation of sintering: incorporation of rigid-body motion. Scripta Materialia, 41(5):487–492, 1999.

[115] XN Jing, JH Zhao, G Subhash, and X-L Gao. Anisotropic grain growth with pore drag under applied loads. Materials Science and Engineering: A, 412(1):271–278, 2005.

[116] Yu U Wang. Computer modeling and simulation of solid-state sintering: a phase field approach. Acta Materialia, 54(4):953–961, 2006.

[117] Qiang Du, Chun Liu, and Xiaoqiang Wang. Simulating the deformation of vesicle membranes under elastic bending energy in three dimensions. Journal of Computational Physics, 212(2):757–777, 2006.

[118] Thierry Biben, Klaus Kassner, and Chaouqi Misbah. Phase-field approach to three-dimensional vesicle dynamics. Physical Review E, 72(4):041921, 2005.

[119] G Horvay and JW Cahn. Dendritic and spheroidal growth. Acta Metallurgica, 9(7):695–705, 1961.

[120] G Horvay. Modified Stefan problem. Journal of Engineering Physics, 8(6):539–557, 1965.

[121] RF Sekerka, CL Jeanfils, RW Heckel, and HI Aaronson. Lectures on the theory of phase transformations. TMS-AIME, New York, NY, page 117, 1975.

[122] Y Wang, D Banerjee, CC Su, and AG Khachaturyan. Field kinetic model and computer simulation of precipitation of L12 ordered intermetallics from fcc solid solution. Acta Materialia, 46(9):2983–3001, 1998.

[123] DY Li and LQ Chen. Shape evolution and splitting of coherent particles under applied stresses. Acta Materialia, 47(1):247–257, 1998.

[124] Y Wang and AG Khachaturyan. Three-dimensional field model and computer modeling of martensitic transformations. Acta Materialia, 45(2):759–773, 1997.

[125] A Artemev, Y Jin, and AG Khachaturyan. Three-dimensional phase field model of proper martensitic transformation. Acta Materialia, 49(7):1165–1177, 2001.

[126] YL Li, SY Hu, ZK Liu, and LQ Chen. Phase-field model of domain structures in ferroelectric thin films. Applied Physics Letters, 78(24):3878–3880, 2001.

[127] S Choudhury, YL Li, CE Krill, and L-Q Chen. Phase-field simulation of polarization switching and domain evolution in ferroelectric polycrystals. Acta Materialia, 53(20):5313–5321, 2005.

[128] JX Zhang and LQ Chen. Phase-field microelasticity theory and micromagnetic simulations of domain structures in giant magnetostrictive materials. Acta Materialia, 53(9):2845–2855, 2005.

[129] Yunzhi Wang and Armen Khachaturyan. Effect of antiphase domains on shape and spatial arrangement of coherent ordered intermetallics. Scripta Metallurgica et Materialia, 31(10):1425–1430, 1994.

[130] M. Ode, S. Kim, and T. Suzuki. Recent advances in the phase-field model for solidification. ISIJ Int., 41:1076–1082, 2001.

[131] Hendrik J Monkhorst and James D Pack. Special points for brillouin-zone integrations. Physical Review B, 13(12):5188, 1976.

[132] IA Abrikosov, AMN Niklasson, SI Simak, B Johansson, AV Ruban, and Hans Lomholt Skriver. Order-N Green's function technique for local environment effects in alloys. Physical Review Letters, 76(22):4203, 1996.

[133] Oleg E Peil, Andrei V Ruban, and Börje Johansson. Self-consistent supercell approach to alloys with local environment effects. Physical Review B, 85(16):165140, 2012.

[134] Georg Kresse and D Joubert. From ultrasoft pseudopotentials to the projector augmented-wave method. Physical Review B, 59(3):1758, 1999.

[135] Georg Kresse and Jürgen Hafner. *Ab initio* molecular dynamics for liquid metals. Physical Review B, 47(1):558, 1993.

[136] G Kresse and J Hafner. *Ab initio* molecular-dynamics simulation of the liquid-metal–amorphous-semiconductor transition in germanium. Physical Review B, 49(20):14251, 1994.

[137] Georg Kresse and Jürgen Furthmüller. Efficient iterative schemes for *ab initio* total-energy calculations using a plane-wave basis set. Physical Review B, 54(16):11169, 1996.

[138] Fran Cverna et al. ASM ready reference: thermal properties of metals. ASM International, 2002.

[139] P Söderlind, B Sadigh, V Lordi, A Landa, and PEA Turchi. Electron correlation and relativity of the 5-f electrons in the U-Zr alloy system. Journal of Nuclear Materials, 444(1):356–358, 2014.

[140] Alex Landa, Per Söderlind, and Patrice EA Turchi. Density-functional study of the U-Zr system. Journal of Alloys and Compounds, 478(1):103–110, 2009.

[141] A Landa, P Söderlind, and PEA Turchi. Density-functional study of U-Mo and U-Zr alloys. Journal of Nuclear Materials, 414(2):132–137, 2011.

[142] Thien C. Duong and Raymundo Arroyave. Multiscale modeling of discontinuous precipitation in U-Nb. Proceedings of the TMS Middle East - Mediter-

ranean Materials Congress on Energy and Infrastructure Systems (MEMA 2015), pages 481–490, 2015.

[143] Baldwin Sawyer. The uranium-columbium alloy system. ANL-4027 (October 1946), 1947.

[144] HA Saller and FA Rough. Report no. BMI-752. Argone National Laboratory Report ANL-4029, Battelle Memorial Institue Report BMI-752, 1952.

[145] OS Ivanov and GI Terekhov. Transformations of the γ-solid solution during quenching and tempering in the uranium-niobium and uranium-niobium-molybdenum systems. In The Structure of Alloys of Certain Systems Containing Uranium and Thorium, pages 20–34, 1961.

[146] M Hansen and K Anderko. Constitution of binary alloys. J. Electrochem. Soc., 105(12):260C–261C, 1958.

[147] GI Terekhov. Features of the structure of the U-Nb phase diagram. Russ. Metall., (4):170–171, 1982.

[148] RP Elliott. Constitution of binary alloys, first supplement. McGraw-Hill, 1965.

[149] P Chiotti, VV Akhachinskij, and I Ansara. The chemical thermodynamics of actinide elements and compounds, part 5: the actinide binary alloys. V. Medvedev, M.H. Rand, E.F. Westrum Jr., F.L. Oetting (Eds.) International Atomic Energy Agency, Vienna, 1981.

[150] HA Saller and FA Rough. BMI-1000. Compilation of US and UK Uranium and Thorium Constitutional Diagrams, Technical Information Service, Oak Ridge, Tenn., 1955.

[151] Yu.S. Virgil'ev. Nonmetallic inclusions in alloys of uranium and zirconium, niobium, and molybdenum. The Structure of Alloys of Certain Systems Contain-

ing Uranium and Thorium; Gosudarstvennoe Izdatelstvo Literatury v Oblasti Atomnoi Nauki Tekniki, Moscow 306-311 (1961) in Russian; TR: AEC-tr-5834, U.S. Atomic Energy Comm., pages 289–293, 1961.

[152] CAW Peterson and WJ Steele. A study of the effect of alloying on the gamma-phase stability of uranium using vacuum differential thermal analysis. Technical report, California. Univ., Livermore. Lawrence Radiation Lab., 1963.

[153] C Fizzotti and A Maspereni. Effects of heat treatment on the structure of uranium-rich U-Nb alloys. Com. Naz. Energ. Nucl., RT/MET-(66)1, pages 1–23, 1966.

[154] F. Coppola and C. Fizzotti. Metastable phases in uranium-rich U-Nb alloys and their thermal decomposition. Com. Naz. Energ. Nucl, RT/MET-(66)2, pages 1–37, 1966.

[155] L.I. Gomozov, E.M. Lyutina, and O.S. Ivanov. Solubility of zirconium, molybdenum, and niobium in alpha-uranium. Russian Metallurgy, (2):131–135, 1970.

[156] HK Hardy. A "sub-regular" solution model and its application to some binary alloy systems. Acta Metallurgica, 1(2):202–209, 1953.

[157] Y Adda and A Kirianenko. Etude de l'autodiffusion de l'uranium en phase γ. J. Nucl. Mater., 1(2):120–126, 1959.

[158] GB Fedorov, VN Gusev, and EA Smirnov. Diffusive and thermodynamic properties of gamma-phase of uranium-niobium system alloys. Atomnaya Energiya, 32(1):11, 1972.

[159] Norman L Peterson and Robert E Ogilvie. Diffusion studies in the uranium-niobium (columbium) system. Trans. Met. Soc. AIME, 218, 1960.

[160] NL Peterson and RE Ogilvie. Diffusion in the uranium-niobium (columbium) system. Trans. AIME, 227, 1963.

[161] WT Eeles and AL Sutton. X-ray determination of the atomic positions in alpha-uranium at 22 and 660 degree C. Acta Crystallographica, (16):575, 1963.

[162] L.T. Lloyd. Therma expansion of alpha-uranium singal crystals. Journal of Nuclear Materials, 3(1):67–71, 1961.

[163] A. P. Müller and A. Cezairliyan. Thermal expansion of niobium in the range 1500–2700 K by a transient interferometrie technique. International Journal of Thermophysics, 9(2):195–203, 1988.

[164] P. Hidnert and H.S. Krider. Thermal expansion of columbium. U.S. Department of Commerce, Bureau of Standards Journal of Research, 11:279–284, 1933.

[165] Thien Chi Duong, Navdeep Singh, and Raymundo Arróyave. First-principles calculations of finite-temperature elastic properties of Ti2AlX (X = C or N). Computational Materials Science, 79:296–302, 2013.

[166] Hassan S Thawabi, Thien Duong, and Raymundo Arróyave. Thermodynamic and mechanical stabilities of α-and β-Ta4AlC3 via first-principles investigations. Journal of Applied Physics, 114(21):213517, 2013.

[167] Hieu H. Pham, Michael E. Williams, Patrick Mahaffey, Miladin Radovic, Raymundo Arroyave, and Tahir Cagin. Finite-temperature elasticity of fcc Al: atomistic simulations and ultrasonic measurements. Phys. Rev. B, 84:064101, Aug 2011.

[168] Lars Vegard. Die konstitution der mischkristalle und die raumfüllung der atome. Zeitschrift für Physik A Hadrons and Nuclei, 5(1):17–26, 1921.

[169] M Korchynsky and RW Fountain. Precipitation phenomena in cobalt-tantalum alloys. Trans. Met. Soc. AIME, 215, 1959.

[170] Lynda Amirouche and Mathis Plapp. Phase-field modeling of the discontinuous precipitation reaction. Acta Materialia, 57(1):237–247, 2009.

[171] Mats Hillert. On theories of growth during discontinuous precipitation. Metallurgical Transactions, 3(11):2729–2741, 1972.

[172] Mats Hillert. An improved model for discontinuous precipitation. Acta Metallurgica, 30(8):1689–1696, 1982.

[173] RE Hackenberg (2015) private communication to TC Duong, june 28.

[174] Katsumi Nakajima, Markus Apel, and Ingo Steinbach. The role of carbon diffusion in ferrite on the kinetics of cooperative growth of pearlite: a multi-phase field study. Acta Materialia, 54(14):3665–3672, 2006.

[175] I Steinbach and M Apel. The influence of lattice strain on pearlite formation in Fe-C. Acta Materialia, 55(14):4817–4822, 2007.

[176] Ingo Steinbach and Mathis Plapp. Pearlite revisited. Continuum Mechanics and Thermodynamics, 24(4-6):665–673, 2012.

[177] Chuang Ying-Yu, Lin Jen-Chwen, and Y Austin Chang. A thermodynamic description and phase relationships of the Fe-Cr system: part I the bcc phase and the sigma phase. CALPHAD, 11(1):57–72, 1987.

[178] A Van de Walle, M Asta, and G Ceder. The alloy theoretic automated toolkit: a user guide. CALPHAD, 26(4):539–553, 2002.